Ph.D. Thesis

Study on the mechanism of double proton transfer in terms of dynamical electron theory

(動的電子論による二重プロトン移動の反応機構に関する研究)

Department of Basic Science,
Graduate School of Arts and Sciences,
The University of Tokyo

Michihiro Okuyama

奥山 倫弘

2009

Contents

1 General Introduction **1**

1.1 Introduction for the present thesis 1

1.2 Organization of this thesis 2

2 Electron flux in molecules induced by nuclear motion **5**

2.1 Introduction 6

2.2 Nonadiabatic electron dynamics and its induced flux 7

2.2.1 Electron flux 7

2.2.2 Nonadiabatic electron wavepacket dynamics with the semiclassical Ehrenfest theory 8

2.3 Illustrative examples of the Schiff flux 10

2.3.1 A typical covalent bond: H_2 10

2.3.2 Electron transfer induced by nonadiabatic transition: NaCl 10

2.3.3 Intra- and inter-molecular electron current in double proton transfer dynamics of formic acid dimer 11

2.4 Time-shift flux 11

2.4.1 Definition 11

2.4.2 Induced flux and adiabatic flux 12

2.4.3 Approximate calculation of the time-shift flux 13

2.4.4 Time-shift flux for the semiclassical Ehrenfest wavefunction. 13

2.4.4.1 H_2 13

2.4.4.2 NaCl 14

2.4.4.3 FAD 14

2.4.5 Time-shift flux extracted from *ab initio* molecular dynamics (AIMD) 14

2.4.5.1 H_2 14

2.4.5.2 FAD 15

2.5 Concluding Remarks 15

3 Electron wavepacket dynamics of double proton transfer for FAD: Semiclassical Ehrenfest study **23**

3.1 Introduction 25

3.2 Electronic reorganization from monomers to dimer: Molecular orbitals and electron densities of FAD at the stable and transition states 27
3.2.1 Computational methods 27
3.2.2 Geometric structures at stable and transition states for FAD and FAM 27
3.2.3 Molecular orbitals study for FAD at stable and transition states . . 28
3.2.3.1 Some characteristics of the canonical molecular orbitals . . 28
3.2.3.2 Electron deficient chemical bonds: Comparison with diborane 28
3.2.4 Localized molecular orbitals (LMO) at stable and transition states for FAD 29
3.2.5 Similarity of electronic structure between the stable and transitions: energetics 30
3.2.6 Electronic reorganization from monomers to dimer: Difference electronic density 31
3.2.6.1 Deformation of the electronic density 31
3.2.6.2 Electronic currents 32
3.3 Double proton transfer dynamics in FAD as studied with Semiclassical Ehrenfest theory (SET) 33
3.3.1 Initial condition and computational procedure to solve SET 33
3.3.2 Time series of geometry change 33
3.3.3 Proton carries much electron density in its transfer: Mulliken population analysis 34
3.3.4 Extremely small contribution of hydrogen-atom migration: Very small radical character in the reaction 35
3.3.5 Large fluctuation of double bonds: Bond order dynamics representing the fluctuation of double bonds 36
3.3.6 Bending motion of CH with respect to OCO plane assisting the π-bond fluctuation through sigma-bond to pi-conjugation 37
3.3.7 Global feature of electronic state remains almost constant: Snapshot of difference density 38
3.3.8 Gross electron flux associated with proton transfer: Adiabatic electron flux 39
3.3.9 Schiff's flux of electrons induced by nonadiabatic interaction 42
3.4 Summary of the dynamics: monomers to dimer, and double proton transfer: Concluding remarks 43

4 General Conclusions **81**

Chapter 1

General Introduction

1.1 Introduction for the present thesis

In nature, there are many atoms and molecules. They undergo various interesting chemical reactions in gas, liquid, and solid phases. Theoretically studying chemical reactions is equivalent to tracking the positions of electrons and nuclei within molecules. These motions are basically described in terms of the time-dependent Schrödinger equation, and the quantum states of a molecule is determined in principle. However, the resultant equations are quite often too large to solve directly even for molecules of moderate size. Therefore we need various approximations, depending on what physical aspects one investigates. In the present study we adopt the so-called mixed quantum-classical representation to track dynamically the quantum states of molecules. In this representation, the electrons and nuclei are treated by quantum and classical mechanics, respectively.

As the simplest extreme of this theoretical scheme, one may recall of the classical trajectory calculations, in which the classical nuclei are driven by the Newton mechanics on a single electronic potential energy surface based on the Born-Oppenheimer approximation [1, 2, 3]. This is called *ab initio* molecular dynamics (AIMD) method and frequently is used to practically analyze chemical reactions. Since AIMD requires diagonalization of the electronic Hamiltonian at each nuclear configuration, Car and Parrinello [4] proposed a new molecular dynamics method that leads to an energy minimum of a molecular system without diagonalization of the electronic Hamiltonian. Some studies based on this method have been reported in the literature even for relatively large molecular systems [5, 6, 7, 8, 9].

A critical deficiency of these methods, however, is that the electron dynamics on the course of chemical change can't be tracked dynamically. One of the simplest methods to treat electron dynamics is the so-called semiclassical Ehrenfest theory (SET) [10, 11, 12]. In this theory, the motion of the electrons follows the time-dependent Schrödinger equation (TDSE) according to the modified electronic Hamiltonian, while the motion of the

nuclei follows the Newtonian equation being driven by a mean-field force generated by the average energy of the electronic wavepacket states. The equations of motion for electronic and nuclear motions are solved simultaneously in a coupled fashion. Although SET faces a theoretical difficulty well after a molecular system passes across a nonadiabatic region, it gives a beautiful and accurate representation of the electron wavepacket dynamics. In the present study, therefore, we adopt SET as a means to track electronic wavepacket dynamics within the validity range of the theory. This treatment includes electronic wavepacket propagation in terms of linear combinations of the so-called configuration state functions, each of which is an appropriate linear combinations of the Slater determinants, and its equation of motion takes explicit account of the nonadiabatic (nuclear kinematic) coupling elements. An extensive application of such SET in *ab initio* level is yet found rare in the literature of quantum chemistry and chemical reaction dynamics.

Thanks to the progress of the method of electron wavepacket dynamics such as the above SET, electronic wavepacket states, rather than the eigenstates of the stationary state electronic Hamiltonian, are now getting more available and becoming less exceptional. In this situation of the stage of progress, the main aim of the present work is to develop the methodology to analyze chemical reactions by extracting dynamical information from the electronic wavepackets. As an example, we study the probability current density of electrons. This is a quantity to represent how the electronic probability density flows just like fluid in molecular space. With this quantity, we can visualize clearly the atto-second change of the electron current in the course of a bond rearrangement. Indeed, we will numerically show for the first time the examples of the electron probability current density or Schiff's flux that is driven by nuclear kinematic couplings. Furthermore, we propose a new way to determine the electronic current, which can be applied to the AIMD. This is not a trivial extension of the Schiff flux, since the latter gives only a null field for such a stationary wavefunction.

The second aim of the present study is to apply our developed physical quantities to an actual chemical system. As a typical example we have picked double proton transfer in formic acid dimer. This is because electronic rearrangement and flow inside the molecular complex that take place synchronously with proton motions is of general interest and highly nontrivial. Indeed we will find the way of such dynamics to proceed in this thesis.

1.2 Organization of this thesis

We first introduce a time shift flux and define adiabatic flux based on in chapter 2. Then, we apply the Schiff's and adiabatic fluxes to the collision reaction of H_2 and NaCl, and we show that the adiabatic flux can describe well the process which generates covalent and ionic bonds of H_2 and NaCl, respectively in the frameworks of the SET and AIMD method. In chapter 3, the adiabaitc flux is applied to the double proton transfer (DPT)

in formic acid dimer (FAD). With the adiabatic flux and some physical quantities, we study the mechanism of it.

References

[1] J. J. P.Stewart, L. P. Davis and L. W. Burggraf, J. Comput. Chem. **8**, 1117 (1987).

[2] S. A. Maluendes and M. Dupuis, J. Chem. Phys. **93**, 5902(1990).

[3] R. N. Barnett and U. Landman, Phys. Rev. B **48** 2081 (1993).

[4] R. Car, M. Parrinello, Phys. Rev. Lett. **55** 2471 (1985).

[5] M. E. Tuckerman, D. Marx, M. L. Klein and M. Parrinello, Science. **275** 817 (1997).

[6] S. Miura, M. E. Tuckerman and M. L. Klein, J. Chem. Phys. **109** 5290 (1998).

[7] K. Laasonen, A. Pasquarello, R. Car, C. Lee and D. Vanderbilt, Phys. Rev. B **47** 10142 (1993).

[8] B. Chen, I. Ivanov, J. M. Park, M. Parrinello and M. L. Klein, J. Phys. Chem. B **106** 12006 (2002).

[9] I. Bakó, J. Hutter and G. Pálinkás, J. Chem. Phys. **117** 9838 (2002).

[10] H. D. Meyer, W. H. Miller, J. Chem. Phys. **70**, 3214 (1979).

[11] M. Amano and K. Takatsuka, J. Chem. Phys. **122**, 084113 (2005).

[12] K. Yagi and K. Takatsuka, J.Chem. Phys. **123**, 224103 (2005).

Chapter 2

Electron flux in molecules induced by nuclear motion

Abstract

As a general tool for analysis of chemical reactions from the view point of electron wavepacket dynamics, electron flux within a molecule is numerically realized in terms of physically time-dependent electronic wavefunctions given by the semiclassical Ehrenfest theory. These wavefunctions are synchronized with real time motion of molecular nuclei through the nuclear kinematic coupling (nonadiabatic elements). Since the standard quantum flux gives only a null field for a real-valued electronic eigenfunction, we extend the definition of flux such that the essential information of dynamical flow of electrons can be retrieved even from adiabatic electronic wavefunctions calculated in the scheme of the so-called *ab initio* molecular dynamics.

2.1 Introduction

Studies on pathways of electrons in the course of chemical reaction are fundamentally important in chemistry, biology and relevant material sciences. The current electronic structure theory of molecules, i.e. quantum chemistry, can provide the accurate snapshots of electronic distribution associated with geometrical changes of even very large molecules. In fact, however, these snapshots do not actually represent the dynamical electron current at each time, simply because most of the electronic wavefunctions in quantum chemistry do not include the time variable, which represents electronic standing waves within the Born-Oppenheimer approximation [1]. However, in the deeper study of dynamical chemical reactivity, we sometimes want to identify how electronic flow in a molecule occurs as a function of real time, synchronizing with the nuclear motions and/or an applied external field (as such examples of demanding the knowledge of electron flow in molecules, see for instance, [2, 3]), which partly constitutes the motivation of the present work. Another quest for the real time dynamics of electrons arises from the rapid progress of attosecond (as) pulse laser technology [4, 5, 6, 7, 8, 9, 10, 11, 12, 13, 14, 15] With the successive use of such ultra short time pulses (as in the pump-probe experiments), one may be able to follow the real dynamics of electronic motion eventually. Therefore we here study some practice to extract the quantum flux from *ab initio* electronic wavepackets. Although the electronic flux is not necessarily a direct observable, theoretical insight about molecular electron dynamics might serves as a useful guide even for experimental studies. Furthermore, such a study is definitely necessary for a higher stage of chemical reactivity theory, particularly for reactions in electronically excited states.

In order for the standard definition of flux to give a nonzero value, an electronic wavefunction under study must be a complex-valued function [16]. In their pioneering works in chemical reaction dynamics, Wyatt et al. have shown beautiful quantum mechanical flux arising from nuclear wavepackets in the reaction of H+ H_2 [17] and F+H_2 [18] (see also [19]). As for the electronic flux within a molecule, such time-dependent currents are usually induced by applying external fields to them. For instance, Steiner and Fowler performed a molecular orbital study of electron flux induced by a magnetic field in conjugated molecules [20] and clusters [21]. Tsukada et al. have presented an extensive theoretical studies on electron conductance of atomic and molecular bridges such as the so-called molecular wire [22]. In their study, a wide class of molecular systems were shown to exhibit interesting patterns of electron current by application of biased electrodes and magnetic field. More recently, Barth et al. have carried out an *ab initio* calculation to numerically realize the unidirectional electron ring current in Mg-porphyrin [23].

To track the electron current induced by chemical reactions in vacuum, one should find a way to correlate an electron wavepacket with the absolute time by synchronizing with nuclear motions. Indeed, Barth et al. have recently extracted electronic and nuclear

simultaneous fluxes using the full quantum non-Born-Oppenheimer calculation of H_2^+ molecule [24]. As a method to treat a many-electron system, however, we in this paper adopt the semiclassical Ehrenfest theory [25, 26], in which electron wavepacket dynamics is determined through the nuclear kinematic couplings (nonadiabatic coupling). This is the case even if a system under study does not have an explicit avoided crossing or conical intersections [27, 28]. In our study, an electronic wavefunction is propagated in time along a "classical" nuclear path, and it becomes inevitably complex valued. With these complex wavefunctions, the standard quantum mechanical flux, that is, the probability current density [16], which we denote the Schiff flux for simplicity in this paper, can be explicitly evaluated for even a large molecule. Thus the first aim of this study is to achieve numerical realization of the Schiff flux for the semiclassical Ehrenfest electron wavepackets. To the best of our knowledge, no such numerical calculation has ever been reported in the literature.

However, generation of a complex valued electronic wavepacket through the cumbersome nonadiabatic couplings is neither common nor easy. On the other hand, the so called *ab initio* molecular dynamics (AIMD) [29] has been well established as an on-the-fly technique of propagating classical trajectories with use of the analytic evaluation of the energy gradient of potential energy hypersurfaces [30, 31]. In this method, the adiabatic electronic wavefunction is produced at each nuclear configuration successively. However, being real-valued in general, these wavefunctions give identically zero to the Schiff flux. The second aim of this paper is, therefore, to extend the Schiff flux so that the dynamical information on the intrinsic electron flux hidden behind such a standing wavefunction is extracted.

This chapter is organized as follows: Starting with the definition and formalism of the nonadiabatic electron wavepackets in Sec. 2, we show, in Sec. 3, how the electron flux is induced in molecules by nuclear motion. In Sec. 4, we extend the standard quantum mechanical flux so that it can extract the electron flux in a stationary-state electronic wavefunction. The paper concludes in Sec. 5.

2.2 Nonadiabatic electron dynamics and its induced flux

2.2.1 Electron flux

We start with the general definition of quantum mechanical flux, and then proceed to the electron flux within a molecule.

Let

$$i\hbar\frac{\partial}{\partial t}\psi\left(\mathbf{r},t\right)=\left[-\frac{\hbar^2}{2m}\nabla^2+V\left(\mathbf{r},t\right)\right]\psi\left(\mathbf{r},t\right) \tag{2.2.1}$$

be a one-body Schrödinger equation and consider a population loss from a closed volume Ω such that

$$\frac{\partial}{\partial t}\int_{\Omega}\psi^{*}\left(\mathbf{r},t\right)\psi\left(\mathbf{r},t\right)d\mathbf{r}, \tag{2.2.2}$$

then the flux vector naturally arises as [16]

$$\vec{j}\left(\mathbf{r},t\right)=\frac{\hbar}{2im}\left[\psi^{*}\left(\mathbf{r},t\right)\nabla\psi\left(\mathbf{r},t\right)-\psi\left(\mathbf{r},t\right)\nabla\psi^{*}\left(\mathbf{r},t\right)\right]. \tag{2.2.3}$$

This is a direct consequence of the conservation of probability, and is automatically followed by the N-particle extension: With

$$\tilde{\nabla}_{N}=\sum_{j=1}^{N}\left(\begin{array}{ccc}\frac{\partial}{\partial x_{j}} & \frac{\partial}{\partial y_{j}} & \frac{\partial}{\partial z_{j}}\end{array}\right), \tag{2.2.4}$$

the 3-dimensional flux is represented as

$$\vec{j}_{N}\left(\mathbf{r}_{1},\mathbf{r}_{2},\cdots,\mathbf{r}_{N}\right)=\frac{\hbar}{2im}\left(\psi^{*}\left(t\right)\tilde{\nabla}_{N}\psi\left(t\right)-\psi\left(t\right)\tilde{\nabla}_{N}\psi^{*}\left(t\right)\right), \tag{2.2.5}$$

which is reduced to the one-particle reduced flux

$$\vec{j}\left(\mathbf{r}_{1}\right)=N\int\vec{j}_{N}\left(\mathbf{r}_{1},\mathbf{r}_{2},\cdots,\mathbf{r}_{N}\right)d\mathbf{r}_{2}\cdots d\mathbf{r}_{N}, \tag{2.2.6}$$

or

$$\vec{j}\left(\mathbf{r}\right)=\frac{\hbar}{2im}\left[\tilde{\nabla}_{1}\gamma\left(\mathbf{r}',\mathbf{r};t\right)-\tilde{\nabla}_{1}\gamma\left(\mathbf{r},\mathbf{r}';t\right)\right]\Big|_{\mathbf{r}'=\mathbf{r}}, \tag{2.2.7}$$

where $\gamma\left(\mathbf{r}',\mathbf{r};t\right)$ is the off-diagonal spin-free first order reduced density matrix [32]. In this expression, $\tilde{\nabla}_{1}$ is to be operated on the $\mathbf{r}$ coordinates first and after that $\mathbf{r}'$ should be replaced with $\mathbf{r}$.

Note that if a wavefunction at hand is real-valued, as a solution of the stationary state Schrödinger equation, the flux of Eq. (2.2.7) is identically zero. Thus, within the framework of standard quantum chemistry aiming at the solution of the electronic eigenvalue problem, the flux is not a useful quantity. This is the case even for an electronic wavefunction representing the electron transfer process. The zero flux is a natural consequence of the situation that a standing wave solution is simply superposition of electron currents having exactly opposite directions to each other. A direct idea to induce such electron current is to apply a time-dependent interaction such as a field provided by a laser or dynamical magnetic fields as described in Introduction. On the other hand, our main concern in this paper is the electron flux synchronously induced by nuclear motion in the course of chemical reactions.

2.2.2 Nonadiabatic electron wavepacket dynamics with the semiclassical Ehrenfest theory

To attain a time-dependent electronic wavefunction, we use the semiclassical Ehrenfest theory (abbreviated as SET). Although this method becomes invalid once the relevant

nuclear path passes across an avoided crossing or conical intersection, and although this difficulty can be totally removed by our method of phase space averaging and natural branching (PSANB) [33, 34], we do use SET just to illustrate how the electron current is calculated. Any other time-dependent electronic wavefunctions can be equally applied. Below is the outline of the primitive version of SET we use in this paper [25, 26]. Note that close inquiry of quantitative accuracy is not in the scope of the present work. Within the nonrelativistic scheme, our quantum mechanical molecular Hamilton is generally of the form

$$H(\mathbf{r},\mathbf{R}) = \frac{1}{2}\sum_k \hat{P}_k^2 + H^{(\mathrm{el})}(\mathbf{r};\mathbf{R}), \tag{2.2.8}$$

where many-body electronic Hamiltonian is defined by

$$H^{(\mathrm{el})}(\mathbf{r};\mathbf{R}) = \frac{1}{2}\sum_j \hat{p}_j^2 + V_c(\mathbf{r};\mathbf{R}), \tag{2.2.9}$$

in mass-weighted coordinates scaling all the masses to unity. Here, $\mathbf{r}$ and $\mathbf{R}$ denote the electronic and nuclear coordinates, respectively, and $\hat{p}_j$ and $\hat{P}_k$ are the operators of their conjugate momenta. $V_c(\mathbf{r};\mathbf{R})$ is the Coulombic interaction potential among electrons and nuclei. In SET, an electron wavepacket is supposed to directly couple with nuclear "classical" motions $\mathbf{R}(t)$ in a manner of $\psi(\mathbf{r};\mathbf{R}(t))$ which is expanded in configuration state functions (CSF) $\{\Phi_I(\mathbf{r};\mathbf{R})\}$ such that

$$\psi(\mathbf{r};\mathbf{R}(t)) = \sum_I C_I(t)\,\Phi_I(\mathbf{r};\mathbf{R})|_{\mathbf{R}=\mathbf{R}(t)}\,. \tag{2.2.10}$$

The electronic state mixing represented by $\{C_I(t)\}$ takes place subject to the electronic Schrödinger equation

$$i\hbar\frac{\partial}{\partial t}C_I(t) = \sum_J \left[H_{IJ}^{(el)} - i\hbar\sum_k \dot{R}_k X_{IJ}^k\right] C_J(t)\,, \tag{2.2.11}$$

where

$$X_{IJ}^k = \left\langle \Phi_I \middle| \frac{\partial \Phi_J}{\partial R_k}\right\rangle \quad \text{and} \quad H_{IJ}^{(\mathrm{el})}(\mathbf{R}) = \left\langle \Phi_I \middle| H^{(\mathrm{el})} \middle| \Phi_J \right\rangle. \tag{2.2.12}$$

On the other hand, the nuclear path is determined by the mean-field force created by the electron wavefunction such that [26]

$$\ddot{\mathbf{R}}_k(t) = -\sum_{I,J,K} C_I^* \left(X_{IK}^k H_{KJ}^{(\mathrm{el})} - H_{IK}^{(\mathrm{el})} X_{KJ}^k\right) C_J - \sum_{IJ} C_I^* \frac{\partial H_{IJ}^{(\mathrm{el})}}{\partial R_k} C_J. \tag{2.2.13}$$

Simultaneous equations (2.2.11) and (2.2.13) are those we actually solve in this paper. For more sophisticated version of SET that includes correction terms both for Eqs. (2.2.11) and (2.2.13), we refer to ref. [34]. The right-hand side of Eq. (2.2.13) is reduced to the Hellmann-Feynman force only if the basis set used were complete.

2.3 Illustrative examples of the Schiff flux

By performing the semiclassical Ehrenfest calculations as above, we show a couple of examples of the Schiff flux for selected molecules having different type of chemical bonding.

2.3.1 A typical covalent bond: H_2

We start with one of the simplest covalent chemical bonds, hydrogen molecule, to see how the electrons flow in the course of bond formation and cleavage. We first prepare a pair of hydrogen atoms on the ground electronic state at ~ 1.85 Å of their mutual distance. Then, we let them collide to each other with some relative momentum. They approach each other and eventually are bounced back by the potential barrier. Figure 2.1 panels (a1) and (a2) shows a pair of snapshots of the Schiff flux based on the SET wavefunction taken at the internuclear distance $R = 1.32$ Å, one on the occasion of approaching (a1), the other separating (a2). A SET calculation has been carried out in terms of two CSFs using only two low-lying σ orbitals in 6-31G** basis. The weight of the configuration of double excitation is in the order of 10^{-5}.

Two obvious points are immediately noticed. Due to the symmetry (note that the mesh points in Fig. 2.1 are a little asymmetric), the electron flux at the central dividing cross-section should be zero. In approaching, the electrons are flowing into the inner area of H-H, thus pulling the nuclei inside. On the other hand, when separating, the electrons flow out of the bonding region to pull the nuclei outwards.

2.3.2 Electron transfer induced by nonadiabatic transition: NaCl

As the second example, we explore the flux of NaCl. This molecule is well-known for its electron transfer dynamics due to the potential crossing between the ionic $Na^+ + Cl^-$ state and the neutral $Na + Cl$. The avoided crossing is localized at ~ 7.4 Å in their internuclear distance. We have let the neutral Na and Cl hit with a small kinetic energy (~ 0.095 eV) but with zero impact parameter. SET wavepacket has been propagated in time in terms of 703 CSFs of CISD with molecular orbitals of 6-31G basis set. Figure 2.2 (a) shows the electron current at $R = 8.31$ Å , which is significantly before the crossing. As seen, the electrons are already flowing from Na to Cl side through such a distant space. It is noteworthy that electrons around chlorine atom is receding from the nucleus, and there is a confluent point between the two flux lines from Na and Cl, which is naturally located close to Cl nucleus. In the internuclear distance of $R = 7.39$ Å (panel (b)), which is very close to the avoided crossing point, the confluent point is found almost in the middle of the bond distance. After the nuclear path has passed over the crossing region, at $R = 6.02$ Å (panel (c)), the qualitative feature of the flux does not change much from that of panel (b).

2.3.3 Intra- and inter-molecular electron current in double proton transfer dynamics of formic acid dimer

Once the semiclassical Ehrenfest electronic wavefunction is at hand, the computation of flux is not a hard task and can be used as an aid to analyze the dynamical mechanism of chemical reactions. We here show such an example of rather complicated electronic flow associated with the so-called double proton transfer in formic acid dimer (FAD). In organic chemistry, the rearrangement of double bonds synchronizing with the proton transfers is termed as tautomerization. However, it is not clear how the tautomerization is accomplished from the view point of electrons flows, since there are a couple of nontrivial competing channels for them [2]. Here is an example of the electron flux within FAD in the energy range where double proton transfers are possible. SET wavepacket has been evolved in time in terms of 861 CSFs of CISD with molecular orbitals of STO-6G basis set. In Fig. 2.3, panel (a) shows the flux mostly on the molecular plane (so to say σ-flow), while panel (b) exhibits the flow at a plane which is shifted by 0.529 Å from the molecular plane (π-flow). It is remarkable that we observe a global flow throughout the two molecules in the π-flow, which suggests a collective motion in the current within and between the molecules.

2.4 Time-shift flux

As stated above, a real-valued wavefunction can give only zero flux in the Schiff definition, Eq. (2.2.3) based on Eq. (2.2.2). This is also the case even for the electronic (adiabatic) wavefunction generated in the course of *ab initio* dynamics. To remedy this aspect of the Schiff flux, we explore a possible extension of it as follows.

2.4.1 Definition

In place of the time variation of the electronic density in Eq. (2.2.2), we consider the dynamics of an overlap integral of a time-propagating wavefunction defined $\psi(\mathbf{r},t)$ in a volume Ω as

$$\begin{aligned} & i\hbar\frac{\partial}{\partial t}\int_{\Omega}\psi^{*}\left(\mathbf{r},t-\Delta t/2\right)\psi\left(\mathbf{r},t+\Delta t/2\right)d\mathbf{r} \\ & =-\frac{\hbar^{2}}{2m}\int_{\Omega}d\mathbf{r}[\psi^{*}\left(t-\Delta t/2\right)\nabla^{2}\psi\left(t+\Delta t/2\right)-\psi\left(t+\Delta t/2\right)\nabla^{2}\psi^{*}\left(t-\Delta t/2\right)] \\ & +\int_{\Omega}d\mathbf{r}\psi^{*}\left(t-\Delta t/2\right)\left(V\left(t+\Delta t/2\right)-V^{*}\left(t-\Delta t/2\right)\right)\psi\left(t+\Delta t/2\right), \end{aligned} \tag{2.4.1}$$

where $\psi(t)$ can be general so far. If no external field is applied, the time dependence of $V(\mathbf{r},t)$ arises from a change in nuclear positions only, and we rewrite it as $V(\mathbf{r},\mathbf{R}(t))$.

For a sufficiently small Δt, $V(\mathbf{r}, \mathbf{R}(t+\Delta t/2)) - V^*(\mathbf{r}, \mathbf{R}(t-\Delta t/2))$ must be small due to the slow nuclear motions. Thus we may neglect this term, which results in

$$\begin{aligned}&\frac{\partial}{\partial t}\int_\Omega \psi^*(t-\Delta t/2)\,\psi(t+\Delta t/2)\,d\mathbf{r}\\&= -\frac{\hbar}{2mi}\int_{\partial\Omega} d\mathbf{A}\nabla\cdot\left[\psi^*(t-\Delta t/2)\,\nabla\psi(t+\Delta t/2) - \psi(t+\Delta t/2)\,\nabla\psi^*(t-\Delta t/2)\right],\end{aligned} \tag{2.4.2}$$

where $\partial\Omega$ is the surface of the volume Ω, the coordinates on which are expanded by $\mathbf{A}$. Thus one can define a complex-valued flux

$$\vec{J}(t,\Delta t) = \frac{\hbar}{2im}\left[\psi^*(t-\Delta t/2)\,\nabla\psi(t+\Delta t/2) - \psi(t+\Delta t/2)\,\nabla\psi^*(t-\Delta t/2)\right] \tag{2.4.3}$$

This flux, which we call the time-shift flux, represents a loss of the overlap of a wavefunction given at time $t-\Delta t/2$ with that at $t+\Delta t/2$ through the boundary $\partial\Omega$, which can be, of course, complex. It may also be regarded as a spatial direction of the deformation of a wavefunction from $\psi(t-\Delta t/2)$ to $\psi(t+\Delta t/2)$. To be a little more precise, we rewrite the above overlap integral in Eq. (2.4.1) as

$$\frac{\partial}{\partial t}\int \psi^*(t-\Delta t/2)\,\psi(t+\Delta t/2)\,d\mathbf{r} = \frac{\partial}{\partial t}\int \psi(t+\Delta t/2)\,dF(t-\Delta t/2), \tag{2.4.4}$$

where

$$dF(t-\Delta t/2) = \psi^*(t-\Delta t/2)\,d\mathbf{r}. \tag{2.4.5}$$

Thus, Eq. (2.4.4) may be regarded as the rate of $\psi(t+\Delta t/2)$ running out of a functional region (a part of the Hilbert space) that is covered by $\psi(t-\Delta t/2)$, and $\vec{J}(t,\Delta t)$ is a complex vector that indicates the direction of the loss of such an overlap between two wavefunctions of time interval Δt. Therefore, by tracking $\vec{J}(t,\Delta t)$ with an appropriate choice of Δt, one can comprehend the time dependent flow represented by $\psi(t)$.

2.4.2 Induced flux and adiabatic flux

To study a little more precise feature of the time-shift flux, let us consider the time reversal of $\vec{J}(t,\Delta t)$, that is $\vec{J}(t,-\Delta t)$, which is

$$\begin{aligned}\vec{J}(t,-\Delta t) &= \frac{\hbar}{2im}\left[\psi^*(t+\Delta t/2)\,\nabla\psi(t-\Delta t/2) - \psi(t-\Delta t/2)\,\nabla\psi^*(t+\Delta t/2)\right]\\&= \vec{J}(t,\Delta t)^*.\end{aligned} \tag{2.4.6}$$

Therefore we have the following relations

$$\mathrm{Re}\,\vec{J}(t,-\Delta t) = \mathrm{Re}\,\vec{J}(t,\Delta t), \tag{2.4.7}$$

and

$$\mathrm{Im}\,\vec{J}(t,-\Delta t) = -\,\mathrm{Im}\,\vec{J}(t,\Delta t). \tag{2.4.8}$$

If our treated wavefunction remains real valued as in the *ab initio* dynamics, $\vec{J}(t, \Delta t)$ is kept pure imaginary, that is $\vec{J}(t, \Delta t) = \mathrm{Im}\, \vec{J}(t, \Delta t)$, and the entire flux behaves subject to the classical-like time reversal symmetry due to Eq. (2.4.8). In the limit of $\Delta t = 0$, it follows that

$$\mathrm{Im}\, \vec{J}(t, \Delta t) \to 0 \tag{2.4.9}$$

and

$$\vec{J}(t, \Delta t) \to \vec{j}(t), \tag{2.4.10}$$

with $\vec{j}(t)$ being the Schiff flux. For these reasons, we call the imaginary and real parts of $\vec{J}(t, \Delta t)$ the adiabatic flux and the induced flux, respectively, in what follows.

2.4.3 Approximate calculation of the time-shift flux

It is not necessarily easy to calculate $\vec{J}(t, \Delta t)$ rigorously. We therefore should introduce a practical approximation as follows. For a short time Δt *up to* 100 attosecond (or may be one femtosecond), the nuclear positions do not change significantly. So, in the estimate of $\langle \phi_i(t - \Delta t/2) |\nabla| \phi_i(t + \Delta t/2) \rangle$, where $\phi_i(t)$ are the molecular orbitals, the positions of the *atomic* orbitals are assumed to be common for both $\phi_i(t - \Delta t/2)$ and $\phi_i(t + \Delta t/2)$. But the coefficients of the molecular orbitals and those of the CSF can be mutually different. Likewise, we assume (within a sufficiently short time Δt)

$$\langle \phi_i(t - \Delta t/2) | \phi_j(t + \Delta t/2) \rangle \simeq \delta_{ij}. \tag{2.4.11}$$

This approximation prevents the estimate of $\int d\mathbf{r} \psi^*(t + \Delta t) \nabla \psi(t)$ from being too complicated.

2.4.4 Time-shift flux for the semiclassical Ehrenfest wavefunction.

We first study the basic feature of the time-shift flux by comparison with the Schiff flux based on the semiclassical Ehrenfest wavefunctions.

2.4.4.1 H_2

Figure 2.1 panels ((b1), (c1)) and panels ((b2), (c2)) display the real part (induced flux) and imaginary part (adiabatic flux) of the time-shift flux, which have been calculated with the semiclassical Ehrenfest wavefunctions used in Fig. 2.1 (a1) and (a2). The shift-time chosen is $\Delta t = 20$ as. If Δt is too short, the adiabatic flux simply approach zero and less economical, while for Δt of too long magnitude the overlap in Eq. (2.4.4) loses its clear sense of continuity. Also as Δt become longer, the approximation in Eq. (2.4.11) is deteriorated more significantly. Our numerical experience so far shows that

$\Delta t = 20 - 50$ as is an efficient choice. Again, panel (b1) and (c1) represent the case of approaching nuclei, while (b2) and (c2) does the case of separating nuclei. The induced flux is very similar to the Schiff flux, as it should be. On the other hand, the adiabatic flux is somewhat different from them, but the basic feature or topology is more or less similar. We have currently no idea about the physical meaning of this difference.

2.4.4.2 NaCl

We next examine NaCl, a nonadiabatic electron transfer system. In Fig. 2.4, the first, second, and third rows, represent the cases of $R = 8.31$ Å, $R = 7.39$ Å, and $R = 6.02$ Å, respectively. The panels in the left column (a1), (b1), and (c1) display the induced flux ($\Delta t = 50$ as), which can be directly compared with the Schiff fluxes of Fig. 2.2. The right column panels exhibit the adiabatic flux. Again the topological similarity between the adiabatic and induced fluxes is apparent.

2.4.4.3 FAD

Similar calculations have been performed for FAD. Since we think that the similarity between the induced flux and Schiff flux is already well confirmed, we here consider only the adiabatic flux. Fig. 2.5, panel (a1) displays the adiabatic flux for the σ-flux at the same geometry of Fig. 2.3, while panel (a2) shows for the π-flux. Once again, the similarity of the adiabatic flux to the Schiff flux has been confirmed.

Through the above series of numerical studies, we may conclude that the adiabatic flux can be used as an indicator of the topology of flux, although the details among all these fluxes, namely, the Schiff flux, the induced flux, and the adiabatic flux, are slightly different from each other.

2.4.5 Time-shift flux extracted from *ab initio* molecular dynamics (AIMD)

We have so far utilized the electronic wavefunction propagated in the semiclassical Ehrenfest dynamics, in which the time variable is naturally involved through the nonadiabatic coupling with nuclear motions. We further examine how the adiabatic flux (the imaginary part of the time-shift flux) works for the time-independent eigenfunctions (adiabatic electronic wavefunctions) generated as a snapshot at each moment in *ab initio* molecular dynamics (AIMD).

2.4.5.1 H_2

Our first example is again taken from the hydrogen molecule; the basic behavior of its flux has been well studied as above. Figure 2.1 panels (d1) and (d2) show the adiabatic

flux taken from AIMD in the same situation as those for the other panels of the same figure. The time shift is again set to $\Delta t = 20$ as. It turns out that the adiabatic flux of AIMD is similar to the Schiff flux, which is quite promising.

2.4.5.2 FAD

The final numerical example of this paper is taken from FAD with the recognition that this molecular complex is large enough to test the adiabatic flux. In Fig. 2.5 panels (b1) and (b2), we show the adiabatic flux extracted from the AIMD, by comparison with the adiabatic flux of the semiclassical Ehrenfest electronic wavefunction, panels (a1) and (a2). We can also compare them with the Schiff flux of FAD at the same geometry shown in Fig. 2.3. As observed in the figures, the flux of this system is rather complicated. Moreover, it is quite often that the electron flux quickly fluctuates in a large molecular system, which can make some difference between the Schiff and time-shift flux. Nevertheless, we may conclude that the topological and overall qualitative behaviors of the vector fields are close enough to one another and the adiabatic flux of AIMD can be used as one of the tools for analysis of chemical reactivity in electron dynamics.

2.5 Concluding Remarks

As a useful tool to study the electron dynamics in the course of chemical reactions, or as an indicator of attosecond wavepacket dynamics, we have studied the electron flux within a molecule or between molecules in terms of the electronic wavefunctions given by the semiclassical Ehrenfest theory. Our preliminary calculations suggest that the electron flux provides with very rich information about electron dynamics to facilitate visualization and conceptualization of chemical processes.

We have also proposed a straightforward extension of the Schiff flux by considering the time dependence of the regional overlap between a wavefunction and its counterpart at some shifted time. One of the remarkable characteristics of this time-shift flux is that its imaginary part of extracts a good approximation of the flux from a real-valued wavefunction such as adiabatic electronic wavefunctions generated in *ab initio* molecular dynamics.

References

[1] M. Born, R. Oppenheimer, Ann. Phys. **84**, 457 (1927).

[2] H. Ushiyama, K. Takatsuka, J. Chem. Phys. **115**, 5903 (2001).

[3] H. Ushiyama, K. Takatsuka, Angew. Chem. Int. Ed. **46**, 587 (2007).

[4] M. Hentschel, R. Kienberger, C. Spielmann, G.A. Reider, N. Milosevi, T. Brabec, C. Corkum, U. Heinzmann, M. Drescher, F. Krausz,. Nature **414**, 509 (2001).

[5] H. Niikura, F. Légaré, R. Hasban, A.D. Bandrauk, M.Y. Ivanov, D.M. Villeneuve, P.B. Corkum, Nature **417**, 917 (2002).

[6] A. Baltuška, Th. Udem, M. Uiberacker, M. Hentschel, E. Goulielmakis, Ch. Gohle, R. Holzwarth, V.S. Yakovlev, A. Scrinzi, A. Hänsch, F. Krausz, Nature **421**, 611 (2003).

[7] Y. Mairesse, A.de. Bohan, L.J. Frasinski, H. Merdji, L.C. Dinu, P. Monchicourt, P. Breger, M. Kovacev, T. Auguste, B. Carrè et al., Phys. Rev. Lett. **93**, 163901 (2004).

[8] Y. Nabekawa, T. Shimizu, T. Okino, K. Furusawa, K. Hasegawa, K. Yamanouchi, K. Midorikawa, Phys. Rev. Lett. **96**, 083901 (2006).

[9] J.J. Carrera, X.M. Tong, S.-I. Chu, Phys. Rev. A **74**, 023404 (2006).

[10] Y.I. Salamin, S. Hu, K.Z. Hatsagortsyan, C.H. Keitel, Phys. Rep. **427**, 41 (2006).

[11] K. Harumiya, I. Kawata, H. Kono, Y. Fujimura, J. Chem. Phys. **113**, 8953 (2000).

[12] N.A. Nguyen, A.D. Bandrauk, Phys. Rev. A **73**, 032708 (2006), and references cited therein.

[13] I. Kawata, H. Kono, Y. Fujimura, J. Chem. Phys. **110**, 11152 (1999).

[14] T. Yonehara, K. Takatsuka, J. Chem. Phys. **128**, 154104 (2008).

[15] K. Takatsuka, T. Yonehara, Adv. Chem. Phys. vol. **144**, to be published.

[16] L.I. Schiff, Quantum Mechanics, McGraw-Hill, New York, 1968.

[17] E.A. McCullough Jr., R.E. Wyatt, J. Chem. Phys. **54**, 3578 (1971).

[18] S.L. Latham, J.F. McNutt, R.E. Wyatt, M. Redmon, J. Chem. Phys. **69**, 3746 (1978).

[19] J.O. Hirschfelder, C.J. Goebel, L.W. Bruch, J. Chem. Phys. **61**, 5456 (1974).

[20] E. Steiner, P.W. Fowler, J. Phys. Chem. A, **105**, 9553 (2001).

[21] P.W. Fowler, R.W.A. Havenith, E. Steiner, Chem. Phys. Lett. **359**, 530 (2002).

[22] M. Tsukada, K. Tagami, K. Hirose, N. Kobayashi, J. Phys. Soc. Jpn **74**, 1079 (2005).

[23] I. Barth, J. Manz, Y. Shigeta, K. Yagi, J. Am. Chem. Soc. **128**, 7043 (2006).

[24] I. Barth, H.-C. Hege, H. Ikeda, A. Kenfack, M. Koppitz, J. Manz, F. Marquardt, G.K. Paramonov, to be published.

[25] A. Jasper, B.K. Kendrick, C.A. Mead, D.G. Truhlar, in: X. Yang, K. Liu (Eds), Modern Trends in Chemical Reaction Dynamics, World Scientific, Singapore, 2004, Part I, Chapter 8.

[26] M. Amano, K. Takatsuka, J. Chem. Phys. **122**, 084113 (2005).

[27] W. Domcke, D.R. Yarkony, H. Köppel, Conical Intersections: Electronic Structure, Dynamics & Spectroscopy World Scientific, 2004.

[28] M. Baer, Beyond Born-Oppenheimer, Wiley, Hoboken, NewJersey, 2006.

[29] K. Bolton, W.L. Hase, G.H. Peslherbe, in: D.L. Thompson (Ed.), Modern Methods for Multidimensional Dynamics Computations in Chemistry, Singapore, 1998, p.143.

[30] P. Pulay, Adv. Chem. Phys. **68**, 241 (1987).

[31] M.C. Zerner, in : A. Szabo, N.S. Ostlund, Modern Quantum Chemistry, Dover, 1996, p.437.

[32] P.-O. Löwdin, Phys. Rev. **97**, 1474 (1955); R. McWeeny, Proc. Roy. Soc. (London) Ser. A **232**, 114 (1954).

[33] K. Takatsuka, J. Phys. Chem. A **111**, 10196 (2007).

[34] T. Yonehara, K. Takatsuka, J. Chem. Phys. **129**, 134109 (2008).

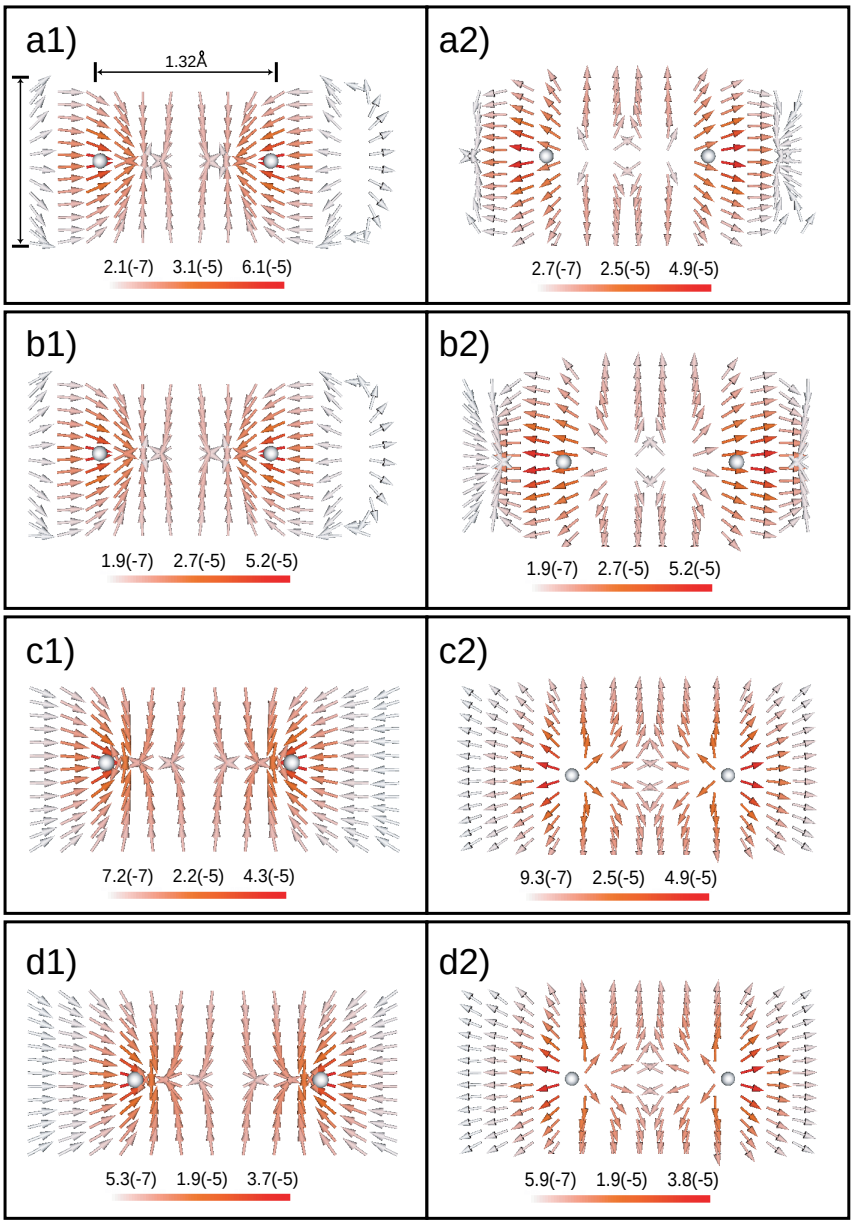

Figure 2.1: (Color online) Electron flux within the hydrogen molecule at the bond distance of 1.32 Å. Flux vectors are drawn at square lattice points. The vertical line-segment in panel (a1) indicates 1.27 Å. In panels of the left column, the atoms are mutualy approaching, while they are separating in the right column. (a1,a2) Schiff flux with SET. (b1,b2) Time shift flux with $\Delta t = 20$ as, the real part (induced flux) with SET. (c1,c2) Time shift flux, the imaginary part (adiabatic flux) with SET. (d1,d2) Time-shift flux (adiabatic flux) estimated with the AIMD (using the adiabatic electronic wavefunctions.) The gray-scale bar represents the intensity of flux measured in units of $\text{Å}^{-2}\times$ as^{-1}.

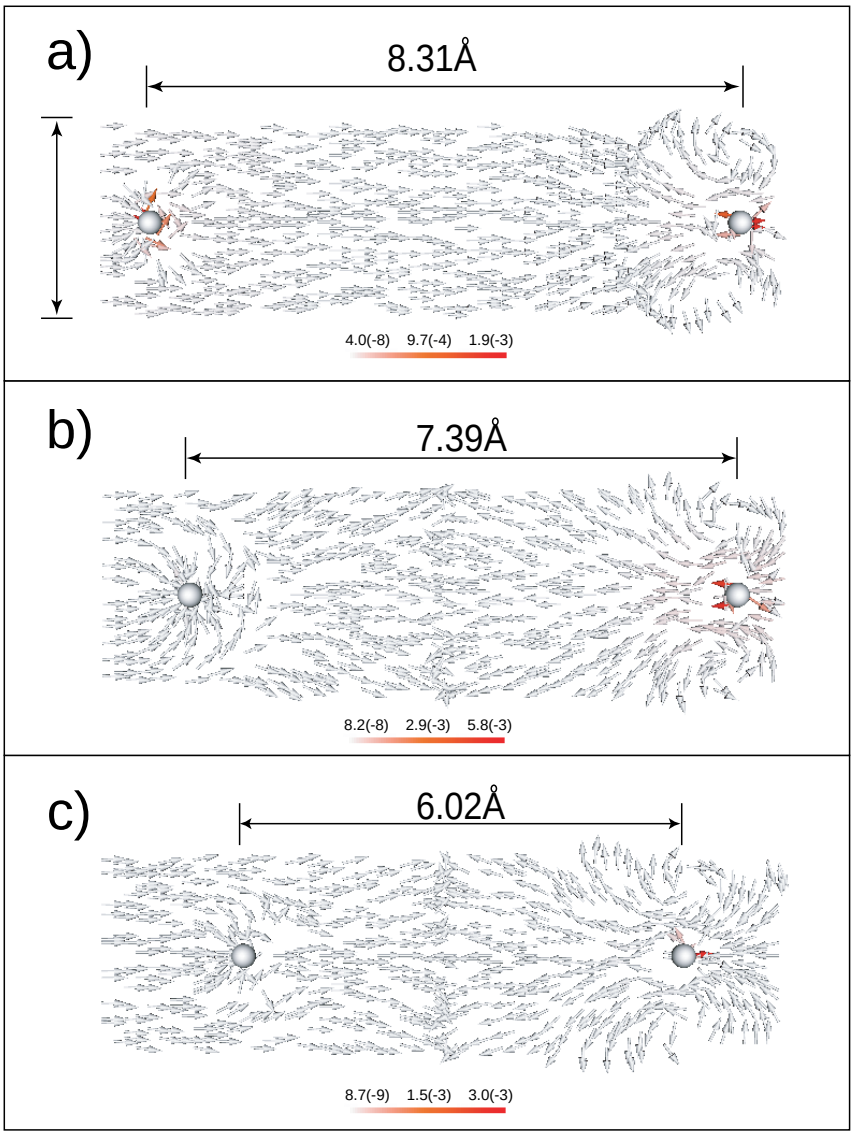

Figure 2.2: (Color online) Schiff flux estimated with SET in NaCl molecule. Left and right spheres graphyically represent Na and Cl nuclei, respectively. Flux vectors are drawn at randomly chosen points.): Snapshots taken at geometries (a) before crossing, (b) at the crossing point, and (c) after crossing. The vertical line-segment in panel (a) indicates 2.65 Å

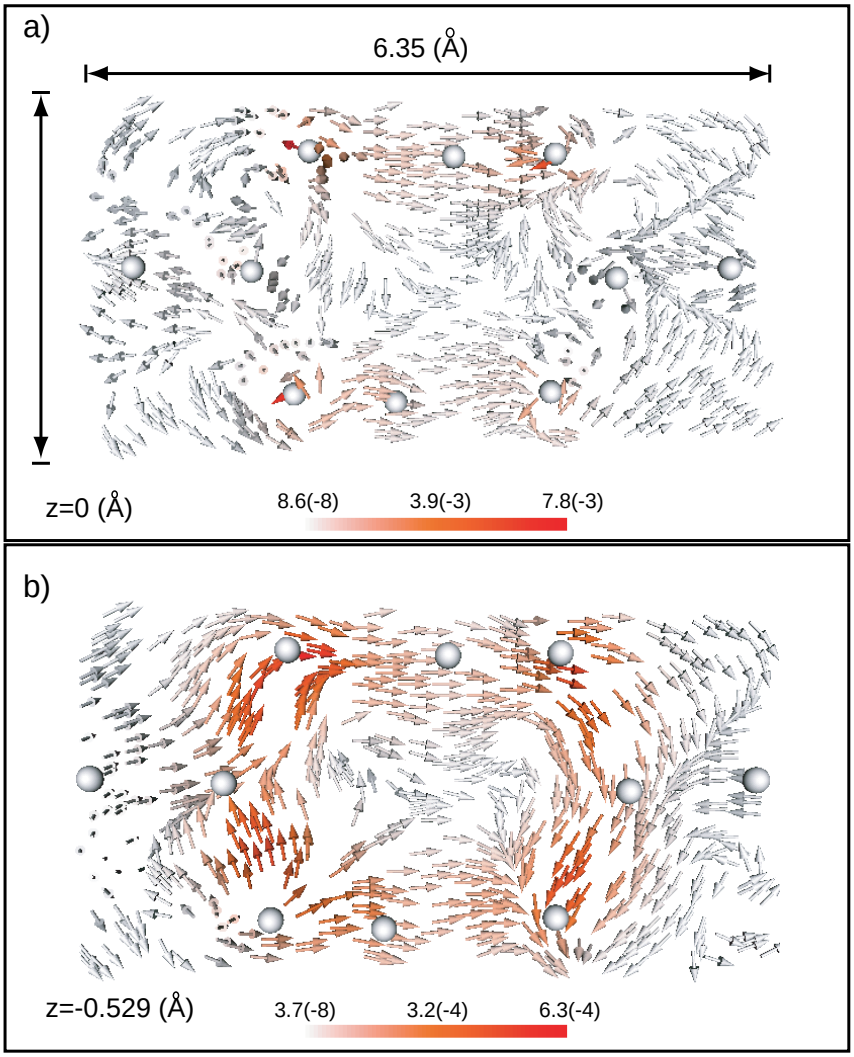

Figure 2.3: (Color online) Schiff flux at a moment of proton transfers in formic acid dimer. Flux vectors are drawn at randomly chosen points. Flux vectors are taken at (a) the mlecular plane (σ-flow) and (b) on a plane blow the plane of (a) by 0.529 Å(π-flow). The vertical line in panel (a) indicates 3.18 Å.

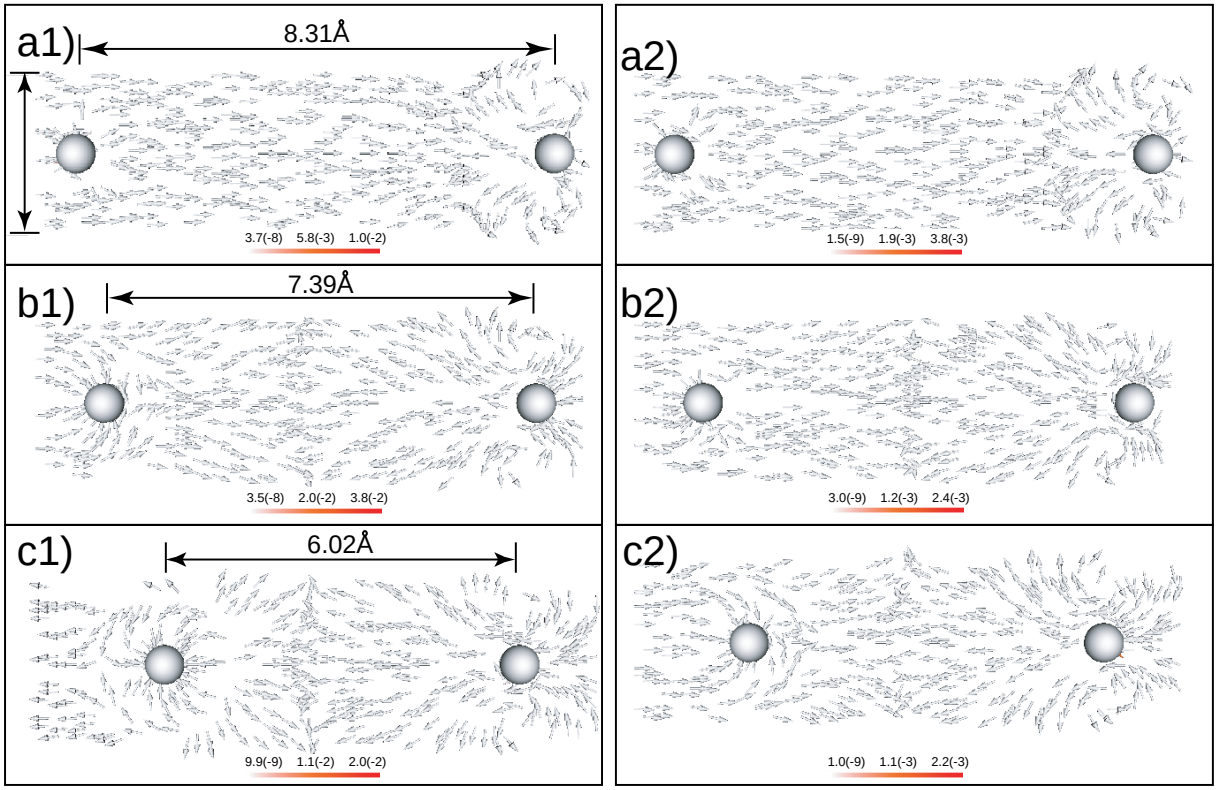

Figure 2.4: (Color online) Time shift flux with SET in NaCl molecule with $\Delta t = 50$ as, the real part (induced flux, left column) and the imaginary part (adiabatic flux, right column). Flux vectors are drawn at randomly chosen points. The nuclei of Na and Cl are located on the left and right, respectively. Snapshots taken at geometries (a1,a2) before crossing, (b1,b2) at the crossing point, and (c1,c2) after crossing. The vertical line-segment in panel (a) indicates 2.65 Å.

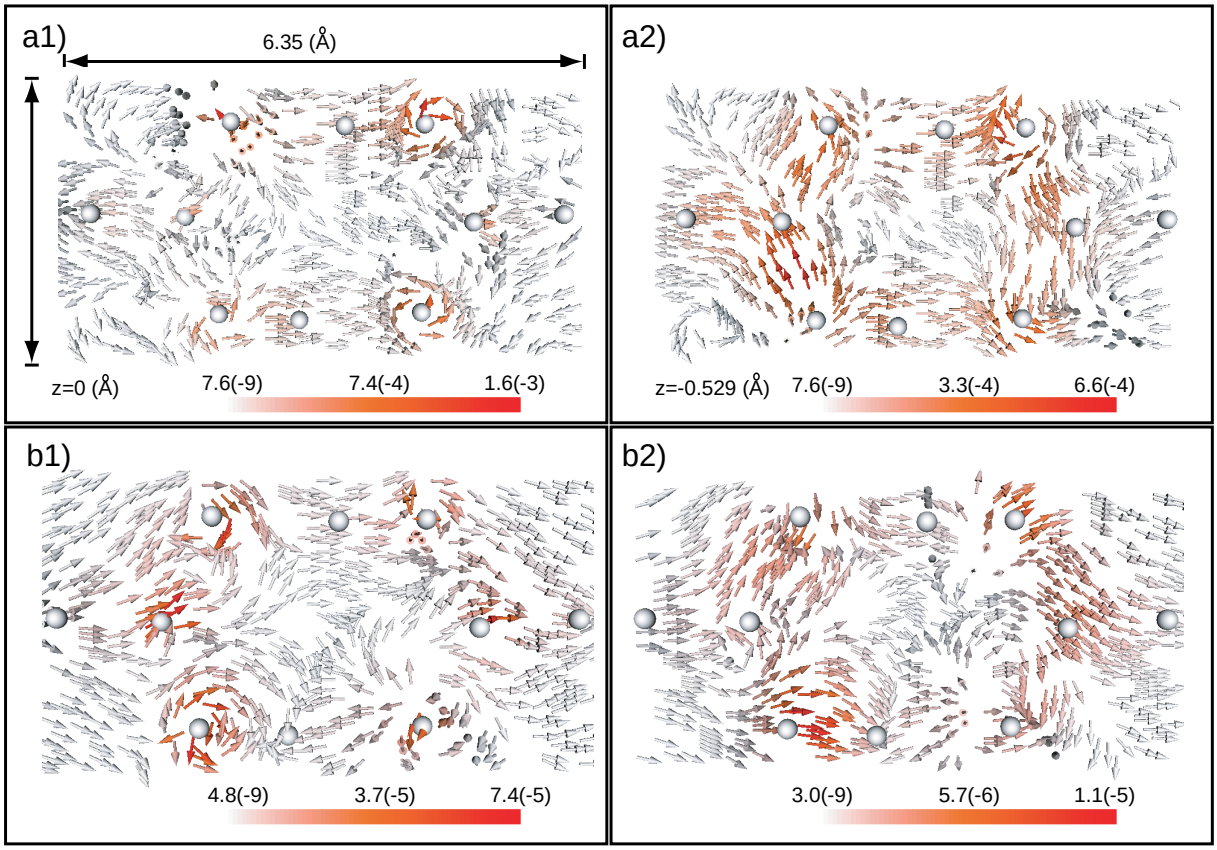

Figure 2.5: (Color online) Time-shift flux in formic acid dimer at the moment of Fig. 2.3 with $\Delta t = 50$ as. Flux vectors are drawn at randomly chosen points. (a1) Adiabatic time-shift fluxes of (a) on the molecular plane estimated with SET, (a2) Adiabatic time-shift flux taken on a plane blow the plane of (a1) by 0.529 Å, estimated with SET. Adiabatic time-shift flux estimated with AIMD taken (b1) on the molecular plane, (b2) on a plane blow the plane of (b1) by 0.529 Å. The vertical line in panel (a1) indicates 3.18 Å.

Chapter 3

Electron wavepacket dynamics of double proton transfer for FAD: Semiclassical Ehrenfest study

Abstract

Double proton transfer is one of the most basic and interesting phenomena not only in chemistry but in biological molecular science. Indeed, a DNA of the double helix structure resorting to double and triple hydrogen bondings may undergo mutation through proton transfers. We study the dynamical electronic mechanism in double proton transfer (DPT) for formic acid dimer (FAD) as an illustrative example by using the semiclassical Ehrenfest theory (SET).

Our main concern is how the molecular complex compensates the possible charge localization due to "proton" transfer, which will induce an electron flow within the molecule complex. This is so to say electronic current induced by proton transfer. Then general questions are what is the geometrical pathway of electron current and how much is the gross current. These analyses can be achieved only with a quantum chemical method that directly treats the electron wavepacket motion within molecules as SET. In doing so, we first investigate the electronic reorganization in dimerization process from two formic acid monomers (FAM) to FAD before proton transfer. We find that the electronic structure of the dimer is already significantly deformed from the relevant monomers in such a manner that the reorganization facilitates the double proton transfer very smoothly. We then proceed to the electron wavepacket study of proton transfer dynamics in terms of SET. After identifying the basic properties, such as the fact that this reaction is not hydrogen-atom migrations but indeed "proton" transfer reaction in concerted mechanism, we investigate the electronic mechanism of this double transfer in great details. In particular, we apply the so-called adiabatic flux studied abouve in this thesis to this study, which reveals the direction of gross current in the dimer. It turns out that electrons flow collectively in the

direction of the transferring protons, but the net amount of electrons that actually flow is not large.

3.1 Introduction

Proton transfer is an important elementary chemical reaction in chemistry, biology, and material physics. For instance, it has been shown that proton transfer plays a vital role in ATP synthesis [1]. Other studies of proton transfer in hydrogen-bonding systems are [2, 3] (theoretical) and [4, 5] (experimental). Raymond et al. [2] have performed *ab initio* molecular dynamics simulation for protonated linear water chain consisting of single proton and six water molecules. Ushiyama and Takatsuka [6] have achieved for the first time electron wavepacket dynamics for $H_5O_2^+$ starting from electronic ground and the first excited states, respectively by using Semiclassical Ehrenfest theory [7, 8].

In nature, there are many molecules which undergo multiple hydrogen bonding like DNA in a double helix structure. In those systems, multiple proton transfer may also take place. In particular, double proton transfer in formic acid dimer (FAD) has been studied extensively as a typical example of multiple proton transfer. In the early studies on this dimer, optimized geometry, transition states, barrier heights were main objects in quantum chemistry [9, 10, 11]. The tunneling splitting has also been calculated with experimental [12] and theoretical approaches [13]. Ushiyama and Takatsuka have studied the timing of double proton transfer and associated electronic structures with use of the so-called *ab initio* molecular dynamics simulation [14], finding that double proton transfer in FAD takes place rather successively.

Here in this paper, we study the electronic mechanism of the double proton transfer in FAD with electron wavepacket method, actually the semiclassical Ehrenfest theory (SET) described in Sec. 2.2.2. In spite of the fact that this dynamics looks simple, arise the following serious questions on its detailed mechanism. First of all, we have shown through a number of examples that transferring proton is never a bare proton nucleus but is always covered with much amount of electrons (0.5 - 0.8 electrons). Based on this numerical finding, the sequential questions follow:

1. What is the dynamical mechanism: proton transfer (Fig. 3.1), hydrogen-atom migration (Fig. 3.2), hydride transfer (Fig. 3.3)? We call the event "proton" transfer tentatively before we can determine the mechanism.

2. In the limit of proton transfer and hydride transfer, a large amount of electrons should flow inside the system to compensate the charges carried by the proton nuclei. How and how much does electron-current occur in the event of "proton" transfer. What is the geometrical path-way of such electrons currents?

3. If the hydrogen-atom migration is the basic mechanism, we do not have to expect such a large net flow of electrons. (See Fig. 3.2) However, it is quite unlikely that hydrogen-atom migration actually happens since very high-energy is expected to generate non-bonded hydrogen atoms. How, though, can we verify this intuitive

statement on the theoretical basis? In other words, how can we determine the distinction between the hydrogen migration and proton transfer.

4. If indeed proton transfer occurs, a kind of coordination of the lone pair of the oxygen atom to the bare proton nucleus is expected. Then, how electrons flow in direction opposite to that of shifting of the double bond within a monomer? In fact, this further electron transfer cannot happen since the valence orbitals of the protonated oxygen is already full. Or else, does an electron jump with the transferring proton from one FAM to the other? If so, isn't it a hydrogen-atom transfer? Besides, a large amount of electron flux is expected from the newly protonated oxygen to the other oxygen that releases proton and electron.

5. The hydride transfer makes the above electron flow even larger and should be precluded as a possible mechanism. And, none of the three mechanisms is good. What is wrong with these classic mechanisms?

The aim of this paper is to resolve these questions in a general manner. The difficulty arises from a simple minded idea that the transfer "protons" are pushed out from each monomeric state. This is actually not the case and it turns out that this simple looking reaction is composed of two states: (1) A significant electronic state reorganization from monomers to dimer precedes the "proton" transfer, in which each of the transferring protons is in a kind of electron deficient chemical bond in the site of OHO. This bonding state makes it easier for the proton nucleus to shift from one side to the other without large electron flow. Also, the double bond nature in C=O is delocalized to the other side and keeps to dynamically fluctuate. The electronic state of the stable geometry of FAD is therefore already close to that of the transition state. (2) We then track the electron wavepacket dynamics associated with "proton" transfer with SET. It turns out that this "proton" transfer proceeds in a concerted mechanism and no hydrogen radical is generated on the reaction path way.

The semiclassical Ehrenfest theory (SET) we apply in the present analysis is a method of mixed quantum-classical treatment; an electron quantum wavepacket evolved on a "classical" nuclear path, which is driven by an mean-field potential given by the electronic wavepacket. With such time-dependent electronic wavepacket we calculate the electronic flux and its related quantities. These methods have been developed in the preceding chapter in this thesis. Since the direction and amount of electron current induced in the double proton transfer is a critical key to understand its mechanism, as described above, the visualization of the dynamical current of electrons is important. In the analysis of FAD, therefore, we develop some theoretical methods to analyze the electron dynamics in reactions and define various quantities, which would serve as useful tools also for analyses of general molecules.

3.2 Electronic reorganization from monomers to dimer: Molecular orbitals and electron densities of FAD at the stable and transition states

As stated in Introduction, we study the double proton transfer in FAD in two stage. Here in this section, we examine what happens when two formic acid monomers (FAM) makes a dimer. A chemically significant reorganization of the electronic structure is observed. We presents both canonical and localized molecular orbitals at the stable (energetically optimized) geometry and at the transition state for double "proton" transfer.

3.2.1 Computational methods

To obtain the geometric structures and electronic states at the stable and transition states for FAD, we carried out electronic state calculation for FAD and FAM with the standard version of GAMESS [15]. In the dynamical calculations with SET, which is implemented into GAMESS, we use the electronic configurations of singles and doubles excitations (CISD) to construct configuration state function (CSF), for which the method by graphical unitary group approach (GUGA) has been applied [16, 17, 18, 19, 20]. The basis set we used are basically STO-6G. In CISD calculation with STO-6G, the number of the canonical molecular orbital (CMO) is 34 with 10 occupied orbitals. We selected 20 frozen core orbitals out of 34 CMOs, resulting in 864 CSFs for SET. Obviously, this basis set is very small, but the number of CSF to expand the electron wavepackets is already large enough.

3.2.2 Geometric structures at stable and transition states for FAD and FAM

In Figure 3.4, we show the schematic pictures of the molecular structures of FAD at the most stable state (consistently abbreviated as SS) and transition state (TS), respectively. For later convenience, we label each atom of FAD as in Fig. 3.4. In Table 3.1, we show the internuclear distance, $R_{\mathrm{A_I B_J}}$, the angle, $\angle \mathrm{A_I B_J C_K}$ and the relative coordinates, $X_i (i = 1, 2)$, where $R_{\mathrm{A_I B_J}}$ is the internuclear distance between the I-th A and J-th B atoms, $\angle \mathrm{A_I B_J C_K}$ denotes the angle between lines $\mathrm{A_I B_J}$ and $\mathrm{B_J C_K}$. $X_i (i = 1, 2)$ will be defined later in Eqs. (3.3.1) and (3.3.2). The units of internuclear distance, angle and relative coordinate are Bohr and degree, respectively, throughout the present paper.

Both FAD at the SS and ST lie on a single plane, and have molecular symmetry of C_{2h} and D_{2h}, respectively. It is found in this computation that the geometries of SS and TS are quite similar to each other in the present basis set, except for the asymmetric positions ofH5 and H10 in SS. Also, the internuclear distance, R_{O3C2} and R_{H5O3} are shortened and

elongated, respectively, from the relevant values of the monomer. This suggests that the double bonds on C=O should be weakened and instead the single bond of C-O be stronger by dimerization. This is not surprising but still provides a theoretical window from which to see the inside of mechanism.

3.2.3 Molecular orbitals study for FAD at stable and transition states

3.2.3.1 Some characteristics of the canonical molecular orbitals

We next try to capture the very basic characteristics of electronic structure of FAD using the RHF molecular orbitals with STO-6G basis set. Figure 3.5, 3.6, 3.7 and 3.8 represent the canonical molecular orbitals (CMO) for SS, while those for TS are drawn in Figs. 3.9, 3.10, 3.11 and 3.12. In both figures the 1s orbitals of C and O atoms are excluded, and only 28 out of 34 MOs are displayed. CMO #24 is the highest occupied molecular orbital (HOMO). The number in each box represents the relevant orbital energy in Hartree. The red and blue distributions in the panel represent positive and negative values, respectively.

We first look at the CMOs of the transition state, which is simpler due to the higher symmetry. As seen graphically all of them show interesting geometrical feature. In particular, CMO #13 along with #11 and #19 strongly suggests a similarity of bonding at the bridging sites C-H-C to the electron deficient bonds of B-H-B in diborane, three center two electron bonding. Another interesting feature is found in CMOs #16 and #17, which are responsible of double bonds between C and O atoms. Due to the obvious symmetry, though, they are not localized in contrast to the monomer. Therefore, these two π-bonds represents a bond order of one and half.

Then, we examine the CMOs at the stable structure. It turns out in this basis set that geometrical distributions as well as their phases at SS are quite similar to those of TS. Indeed, only the order of CMO #17 and #18 is different from each other. CMO #13, along with #11, still retain the feature of the electron deficient bonding. As a natural consequence of the lower symmetry of SS, the CO double bonds are now significantly localized, but still the delocalization over O-C-O site is observed.

3.2.3.2 Electron deficient chemical bonds: Comparison with diborane

As noted above, some of the molecular orbitals suggest that the bonding in the site of O-H-O looks like three-center-two-electron bond, the so-called electron deficient bond, the typical one of which is found in diborane. A large difference between FAD and diborane, though, is that the potential energy for the central proton nuclei in diborane has only a single valley without a potential barrier in contrast to FAD. The molecular orbitals of diborane can be seen in the recent study on its electron wavepacket dynamics in laser

field [21]. The distance between H5 and H10 in FAD (4.288 Bohrs) is much longer than the distance between the central two protons in diborane, and the indirect interaction between them via the bonds H-O-C-O-H in FAD should be much weaker than that of H-B-H of diborane. Therefore the attractive interaction between the central H atoms is not strong enough to overcome the their individual local interactions that tend to shift the position of them from the D_{2h} structure.

3.2.4 Localized molecular orbitals (LMO) at stable and transition states for FAD

It is quite often for the canonical molecular orbitals not to give the valence picture of chemical bonds. The localized molecular orbitals (LMO) facilitates such understanding and sometime provide additional insight. We thus localize the CMOs of FAD. Although we have done it with both Boy's criterion [22] and Ruedenberg one [23], we here show the Boy's LMO $\{\phi'_i\}$, which can be obtained by maximizing the total distance between the molecular orbitals, that is,

$$A\left(\{\phi'_i\}\right) = \prod_{i>j} \left[(R_{ix} - R_{jx})^2 + (R_{iy} - R_{jy})^2 + (R_{iz} - R_{jz})^2\right], \tag{3.2.1}$$

where $\{R_{ia}\}$ are dipole integrals defined by

$$R_{ia} = \langle \phi'_i \left| a \right| \phi'_i \rangle \qquad (a = x, y, z), \tag{3.2.2}$$

where $\{\phi'_i\}$ are usually real functions at standard electronic state calculation. The LMOs $\{\phi'_i\}$ are correlated through an orthogonal transformation with the CMO $\{\phi_\alpha\}$ such that

$$\phi'_i = \sum_{\alpha}^{\mathrm{CMO}} d_{i\alpha}\phi_\alpha \tag{3.2.3}$$

with

$$\left\langle \phi'_i | \phi'_j \right\rangle = \delta_{ij}. \tag{3.2.4}$$

Thus, the above coefficients, $\{d_{i\alpha}\}$ are determined so as to maximize evaluation function, $A\left(\{\phi'_i\}\right)$.

Figure 3.13, 3.14 and 3.15 are LMOs of the stable state (SS), while those at the transition state are displayed in Figs. 3.16, 3.17 and 3.18. To save the space only occupied LMOs, except for the 1s cores of C and O atoms, are exhibited in those figures. Again, the red and blue distributions in the panel represent the positive and negative parts of LMO, respectively.

We first take a closer look at the LMOs at TS. The first four LMOs, panel (a1)-(a4), are obviously four lone pairs lying on the molecular plane and emanating from four oxygen atoms. The next four, panel (b1)-(b4), represent OH bonds in the bridging regions. The

characteristic of the electron deficient bonding at O-H-O site is not clearly reflected in the present LMOs. The next eight LMOs, panel (c1)-(c8), create the so-called τ-bond (or the banana bond) arching between the C and O atoms. It should be noted however, they are a little biased so as to have a heavier weight at O atoms. The last two bonds, panel (d1)-(d2), give rise to CH bonds of the edging CH bonds.

Here again, the LMO at SS are quite similar in shape to those of TS. It is quite interesting to see that even at the stable structure, eight almost equivalent τ-bonds are also generated. Therefore, the difference between the single bond C-O and double bond C=O has become very small in the dimer, that is, FAD.

Another interesting feature in LMO representation is that the nature of electron deficient bonding as in diborane, which was rather clearly observed in CMO representation, is not as clear even at the transition state. This aspect is rather subtle and we will come back later to this point.

3.2.5 Similarity of electronic structure between the stable and transitions: energetics

As shown above, the similarity of both in CMO and LMO at the stable geometry and transition state is quite clear. We here detour the energetics of this characteristic feature by calculating the binding energy and for two monomers to form a FAD, and energy barrier at the transition state energy for the double proton transfer in FAD. These are calculated with CISD method with basis sets, STO-6G, STO-6G(p), STO-6G(p(H5H10)) and 3-21G. STO-6G(p(H5H10)) is the basis set which includes p type polarization function on H5 and H10 atoms. The dimerization energy is defined as

$$\Delta E_d = 2.0 \times E_{\rm s}^{\rm FAM} - E_{\rm s}^{\rm FAD}, \tag{3.2.5}$$

while the potential barrier at the transition state is given by

$$\Delta E_b = E_{\rm t}^{\rm FAD} - E_{\rm s}^{\rm FAD}, \tag{3.2.6}$$

with $E_{\rm s}^{\rm FAM}$, $E_{\rm s}^{\rm FAD}$ and $E_{\rm t}^{\rm FAD}$ being, respectively, the total energy of formic acid monomer, that of FAD at SS, and that of FAD at TS.

Table 3.2 lists these values, but experimental value for ΔE_b was not found in the literature. In this table, dimerization energy with 3-21G is closest to the experimental value. On the other hand, the barrier height with the basis STO-6G(p) and STO-6G(p(H5H10)) are almost equal to that given by 3-21G, although the dimerization energies ΔE_d with them are pretty far from that with 3-21G. Also, the dimerization energy by CISD with STO-6G is much larger than that of the experimental value, whereas the barrier height is much lower than that given by 3-21G. Thus, it seems to be important to use double zeta basis set for the accurate calculation of dimerization energy, and the p type polarization

function may be necessary for the calculation of the barrier height. Nevertheless, we use STO-6G basis for the sake of computational cost in performing a electronic wavepacket propagation with the semiclassical Ehrenfest theory with use of CISD configuration state functions.

3.2.6 Electronic reorganization from monomers to dimer: Difference electronic density

3.2.6.1 Deformation of the electronic density

To clarify more vividly what happens to the electronic states in the process of dimerization of formic acid monomers (FAM) to FAD. To investigate the difference in spatial distribution of one electron density between FAD and two FAMs, we calculate the following difference density [24]. Suppose FAD is given at a geometry. Then one can assume the presence of two FAM at this geometry without any mutual interaction. Then $\Delta\gamma(\boldsymbol{r})$ between FAD and FAM is simply defined as follows

$$\Delta\gamma(\boldsymbol{r}) = \gamma_{\mathrm{FAD}}(\boldsymbol{r}) - \gamma_{\mathrm{FAM}}(\boldsymbol{r}), \tag{3.2.7}$$

where $\boldsymbol{r}$ is the Cartesian coordinate of one electron, and $\gamma_{\mathrm{FAD}}(\boldsymbol{r})$ and $\gamma_{\mathrm{FAM}}(\boldsymbol{r})$ are the diagonal spin-free first order density matrix for FAD and for the two noninteracting FAM, respectively, at this geometry. The density matrix, $\gamma(\boldsymbol{r})$ is defined by

$$\gamma(\boldsymbol{r}) = \sum_{ij} \phi_i^*(\boldsymbol{r})\,\gamma_{ij}\phi_j(\boldsymbol{r}), \tag{3.2.8}$$

where $\{\phi_i(\boldsymbol{r})\}$ and $\{\phi_i^*(\boldsymbol{r})\}$ are one-electron orbital functions and its complex conjugate, respectively, which may be molecular orbitals or atomic orbitals, and $\{\gamma_{ij}\}$ are the relevant coefficients. $\{\gamma_{ij}\}$ in our calculations are given through the CISD and is further decomposed as

$$\gamma_{ij} = \sum_{IJ}^{\mathrm{CSF}} C_I^* \gamma_{ij}^{IJ} C_J, \tag{3.2.9}$$

where $\{C_I\}$ are the coefficients of the CSF, $\left\{\gamma_{ij}^{IJ}\right\}$ are one electron coupling constants [25, 26].

Figure 3.19 shows the difference density, where two FAMs are specified to be the left fragment consisting of O6C7O8H9H10 and the right fragment of O1C2O3H4H5 (the upper proton H5 is transferring from right to left, and H10 from left to right.) These FAM are regarded as two noninteracting FAMs that have been brought in to the give positions and geometries. Here again the CISD method with STO-6G basis set for both $\gamma_{\mathrm{FAD}}(\boldsymbol{r})$ and $\gamma_{\mathrm{FAM}}(\boldsymbol{r})$ has been used. The spatial distribution of the difference densities at the stable structure, panel (a1) - (a3), and those for the transition state, panel (b1) - (b3) are shown. Panels (a1) [(a3)] and (b1) [(b3)] display the contour plot sliced at $Z = -1.0$

[$Z = 1.0$] Bohr from the molecular plane. These represents the difference density mainly in π-bonding. On the other hand, panels (a2) and (b2) shows those at $Z = 0.0$ Bohr, which detects the difference in the σ-bonding. d values in each panel denotes the contour width. Red and blue closed curves in all panels indicate positive and negative values, respectively. The vertical line segment at panel (a1) indicates 10 Bohrs.

We first investigate the stable state. The electronic reorganization occurred in π-bonding, as observed in panel (a1), is a great shift of the double bond from O3-C2 [O8-C7] to the site of O1=C2 [O6=C7], which was already observed in the presence of the eight equivalent τ-bonds in the site of O3-C2-O1 [O6-C7-O8]. The decrease of π-bonding character at C2 [C7] is due to a trade-off between the decrease in O3-C2 [O8-C7] and increase in O1=C2 [O6=C7].

The difference happened in σ-bonding seems a little more complicated, which is observed in panel (a2). The population of the part of sp^2 hybridization on O6, which directs towards H5 side, decreases. There was a double bond in between O6 and C7 in the isolated formic acid monomer, and this hybridization made one of two lone pairs on the molecular plane. On the other hand, in the similar part of sp^2-like space on O3, the electron density increases despite the weakening of the bond of H5O3. The electron density on H5 is a little lower than that in the corresponding monomer. The same phenomena happens in the lower part of FAD, that is the place around O8, H10, and O1, which is the mirror image of the upper site consisting of O6, H5, and O3.

The above reorganization of σ-electrons may be comprehended as the following view: On the O6, the nature of lone pair is partly eliminated and instead the character of the chemical bonding of O6H5 is penetrating in. On O3, conversely, the nature of chemical bonding between H5 and O3 is weakened and the nature of the lone pair is being brought in. The similar phenomena take place also for the transition state. The reason why the electron density on H5 becomes smaller is that H5 has been treated as though it still belongs to the site of the right formic acid monomer in our calculation of the difference density. It is quite natural to conceive that the density on an oxygen atom is larger for a lone pair than for the bond of OH, which accounts for the balance of the positiveness on O3 and negativeness on O6.

The above difference density may summarized that in forming FAD the electronic structure has been significantly deformed so that the release of H5 from O3 making a lone pair on O3 and the accepting of H5 by O6 making a new bond have already become easy and smooth.

3.2.6.2 Electronic currents

Since the FAD lies on a plane, the separation between σ and π electrons holds rigorously. Therefore the electronic deformation in the π-electron systems (decrease in O3 and O8, and increase of O1 and O6) suggests that current in the direction from O3 to O1, and

from O8 to O6. On the other hand, it should be safe to assume that electron does not flow through the σ-bonds of O3-C2-O1 and O6-C7-O8. Then the increased electron density at O3 [O8] should have been supplied from the decreasing site of O6 [O1]. Therefore it is expected that the over all electron flow has taken place in clockwise manner in the present geometrical configuration. That is the reverse direction of the double proton transfer. Note, however, that the double proton transfer does not yet begin.

3.3 Double proton transfer dynamics in FAD as studied with Semiclassical Ehrenfest theory (SET)

This section is devoted to the study of dynamics of proton transfer in formic acid dimer with the semiclassical Ehrenfesrt theory. We show the results of double proton transfer dynamics for FAD by SET.

3.3.1 Initial condition and computational procedure to solve SET

The initial conditions and the computational procedures to solve numerically the equations of motion, Eq. (2.2.11) and Eq. (2.2.13) for SET are as follows: First we prepare the most stable state, or the optimized geometry of FAD using CISD with STO-6G basis. Therefore the initial condition for the electronic state is the ground state. To this molecule, momenta whose kinetic energy as high as 60.2 kcal/mol are given in various directions to initialize the dynamics. 16 paths have been launched to evolve the electron wavepacket in SET calculations, and 11 paths out of these 16 successively undergo double proton transfer. In what follows we pick one path from these as a typical example and perform detailed analyses.

The electronic Hamiltonian matrix, $H_{IJ}^{(\mathrm{el})}\left(\boldsymbol{R}(t)\right)$ to solve SET is generate with CISD configuration state functions in STO-6G basis. The integrators used to solve Eq. (2.2.11) and Eq. (2.2.13) are the 4th order Runge-Kutta and 5th order Gear methods, respectively. The time-step to integrate these equations are 0.5 as [attosecond] for Eq. (2.2.11) and 30 as for Eq. (2.2.13), respectively. We have integrated SET equations up to 180 fs [femtosecond].

3.3.2 Time series of geometry change

We first trace the geometrical change in the proton transfer. To specify the position of protons, H5 and H10 in Fig. 3.4, the relative coordinate, X_1 and X_2 are defined as follows [14]:

$$X_1 = \frac{R_{\mathrm{O6H5}}}{R_{\mathrm{O3O6}}} \cos\left(\theta_{\mathrm{O3O6H5}}\right), \tag{3.3.1}$$

and

$$X_2 = \frac{R_{\mathrm{O8H10}}}{R_{\mathrm{O1O8}}} \cos\left(\theta_{\mathrm{O1O8H10}}\right), \tag{3.3.2}$$

where $R_{\mathrm{A_IB_J}}$ is the internuclear distance between the I-th atom A and J-th atom B, whereas $\theta_{\mathrm{A_IB_JC_K}}$ is an angle between lines $\mathrm{A_IB_J}$ and $\mathrm{B_JC_K}$. By the definition of relative coordinate, $X_1 > 0.5$ and $X_2 < 0.5$ imply that H5 and H10 stay at the O3 and O8 sides, respectively. For instance, $X_1 = 0.5$ is regarded as a criterion to judge whether H5 exceeds the center lines of O3-O6.

In Fig. 3.20, we show the time series of relative coordinates, $X_1(t)$ in panel (a1) and $X_2(t)$ in panel (a2). The vertical and horizontal line segments in this figures are $X_i(t)\,(i = 1, 2)$ and time, respectively, and horizontal line in each panel indicates the critical value to judge proton transfer. In panels (a1) and (a2) observed is a rapidly change from $X_1 > 0.5$ and $X_2 < 0.5$ to $X_1 < 0.5$ and $X_2 > 0.5$ during a period from 60 fs to 80 fs. This fact means that H5 (H10) move from right (left) formic acid monomer (FAM) to the left (right). After this has happened, X_1 becomes consistently small, while X_2 keeps increasing, which simply suggests that two newly formed FAM recede from each other after exchanging the protons. In what follows, we further study what happens in electron wavepacket dynamics behind this proton movement in terms of the present example.

3.3.3 Proton carries much electron density in its transfer: Mulliken population analysis

We then track the time series of the Mulliken charge [27] in Fig. 3.21, where the Mulliken charge on atom A is defined as

$$\text{Mulliken charge} = Z_A - \sum_{\mu \in A}^{\mathrm{AO}} \sum_{\nu}^{\mathrm{AO}} \gamma_{\mu\nu} S_{\mu\nu}, \tag{3.3.3}$$

where Z_A is a nuclear charge at atom A and $S_{\mu\nu}$ are the overlap integrals among the atomic orbitals (AO), which are to be summed up only over AOs belonging to atom A, as symbolized as $\sum_{\mu \in A}^{\mathrm{AO}}$.

In Fig. 3.21 plotted are the Mulliken charge of H5 and H10. A quite interesting fact is observed both in H5 and H10. They remain almost constant, as low as about 0.3 (not 1.0), throughout the proton transfer reaction. A naive interpretation of this observation is that each proton nucleus is covered with electrons as many as about 0.7. Therefore proton in "proton" transfer is never a naked proton nucleus, but it is rather a positively charged hydrogen atom as far as only the electron population is concerned. Surprisingly, therefore, the electronic state, at least the electronic population, on a transferring proton is not affected by the transition from one side to the other.

The above fact has been widely observed in other "proton" transfer dynamics in electronic ground state. Of course, the actual population of the covering electrons depends on a system under study and the basis set used. However, it is quite likely that the above view should be a phenomena quite common to the proton transfer dynamics. So arises a natural question: Is it proton transfer or hydrogen migration?

3.3.4 Extremely small contribution of hydrogen-atom migration: Very small radical character in the reaction

As shown above, it is not theoretically trivial to distinguish between electron rich proton transfer and electron poor hydrogen migration. We here study this aspect from the view point of electronic structure. The idea is that if hydrogen-atom migration happens, a radical centered on the transferring proton nucleus should be form, as though a hydrogen atom is isolated on the way of transfer. Since this implies that a strong chemical bond OH (say O3-H5) is perfectly broken before forming a new OH bond (say O6-H5), this process is likely to be quite unfavorable in energetics. Nevertheless, let us check this possibility.

To judge quantitatively whether a radical center is actually formed on a transferring proton nucleus, we resort to the unpaired electron density proposed by Takatsuka many years ago [28, 29, 30]. It is defined as

$$\hat{D} = \hat{\gamma} - \hat{\gamma}^2, \tag{3.3.4}$$

where $\hat{\gamma}$ is the one electron density operator. In closed shell system, the diagonal elements of Eq. (3.3.4) in coordinate representation become

$$D\left(\boldsymbol{r}\right) = 2\gamma\left(\boldsymbol{r}\right) - \int d\boldsymbol{r}'\gamma\left(\boldsymbol{r},\boldsymbol{r}'\right)\gamma\left(\boldsymbol{r}',\boldsymbol{r}\right), \tag{3.3.5}$$

which represents the spatial distribution of unpaired electrons. To obtain the gross unpaired electron population on an atom A, the matrix elements, we write $\gamma(\boldsymbol{r},\boldsymbol{r}')$ as

$$\gamma(\boldsymbol{r},\boldsymbol{r}') = \sum_{\mu\nu}^{\mathrm{AO}} \chi_\mu\left(\boldsymbol{r}\right)\gamma_{\mu\nu}\chi_\nu\left(\boldsymbol{r}'\right). \tag{3.3.6}$$

and insert it Eq. (3.3.6) to Eq. (3.3.5). Then $D\left(\boldsymbol{r}\right)$ is written as

$$D\left(\boldsymbol{r}\right) = 2\sum_{\mu\nu}^{\mathrm{AO}} \chi_\mu\left(\boldsymbol{r}\right)\gamma_{\mu\nu}\chi_\nu\left(\boldsymbol{r}\right) - \sum_{\mu\nu\lambda\delta}^{\mathrm{AO}} \chi_\mu\left(\boldsymbol{r}\right)\gamma_{\mu\lambda}S_{\lambda\delta}\gamma_{\delta\nu}\chi_\nu\left(\boldsymbol{r}\right). \tag{3.3.7}$$

The gross population for unpaired electron on atom A, N_A, then becomes

$$N_A = \sum_{\mu\in A}^{\mathrm{AO}} \left(2\sum_{\nu}^{\mathrm{AO}} \gamma_{\mu\nu}S_{\nu\mu} - \sum_{\nu\lambda\delta}^{\mathrm{AO}} \gamma_{\mu\lambda}S_{\lambda\delta}\gamma_{\delta\nu}.S_{\nu\mu} \right), \tag{3.3.8}$$

which we call unpaired electron population.

In Fig. 3.22, we show the time series of unpaired electron population on O1, C2, O3, H4, H5, O6, C7, O8, H9 and H10, which is given by Eq. (3.3.8. The population on O1, C2, O3, H4, H5, O6, C7, O8, H9, and H10 are presented in panel (a1), (a2), (a3), (a4), (a5), (a6), (a7), (a8), (a9), and (a10), respectively. Again this time series corresponds to the dynamics of Fig. 3.20.

From this figure, the unpaired electron populations on O1, C2, O3, O6, C7 and O8 are seen to remain as small as about 0.1, and those on H4, H5, H9 and H10 are even smaller down to about 0.01. This fact means that the radical character of FAD remains very small in this reaction. Or, this reaction is essentially of a concerted mechanism. Thus it can be judged that any significant radical center does not appear on the transferring protons in the course of their transfer dynamics, and we preclude the possibility of hydrogen-atom migration in this reaction.

3.3.5 Large fluctuation of double bonds: Bond order dynamics representing the fluctuation of double bonds

We next study the dynamics of the double bonds in C-O sites. To investigate the spatiotemporal distribution of π-bonding as well as its anti-bonding character, we define a bond-order density [21], which is a natural extension of the standard bond order. It is defined as

$$\gamma_{bond}\left(\boldsymbol{r}\right)=\sum_{\mu\nu}^{\mathrm{AO}}\chi_{\mu}\left(\boldsymbol{r}\right)\gamma'_{\mu\nu}\chi_{\nu}\left(\boldsymbol{r}\right), \tag{3.3.9}$$

where $\chi_{\mu}\left(\boldsymbol{r}\right)$ denotes atomic orbital (AO) on μth atom. The matrix elements $\left\{\gamma'_{\mu\nu}\right\}$ are determined as follows

$$\gamma'_{\mu\nu}=\begin{cases}\gamma_{\mu\nu} & \text{(If AO pair span over different atoms)}\\ \\ 0 & \text{(Otherwise)}\end{cases} \tag{3.3.10}$$

and the matrix elements, $\{\gamma_{\mu\nu}\}$ are the spin-free first order density matrix in the AO representation. Recall that these density matrices have been calculated with the electron wavepackets in SET.

In Fig. 3.23, we show the snapshots of the spatial distribution of bond order density. Panel (a1)-(d1), (a2)-(d2), and (a3)-(d3) are given at 40.0fs, 73.9fs, 99.0fs, and 144.9fs on $x-y$ plane (almost the molecular plane) at $z=-1.0$, $z=0.0$, and $z=1.0$ Bohr, respectively. The density at $z=0.0$ Bohr show the bond order for σ-electrons, while those at $z=-1.0$ and $z=1.0$ Bohr are supposed to represent mainly the π-electron dynamics. The width of the contour lines in panels (a1)-(d1), (a2)-(d2) and (a3)-(d3) are 0.005, 0.01 and 0.005, respectively, and the red and blue lines in all the panels represent positive and

negative values, respectively. The vertical line segment in panel (a1) indicates 10.0 Bohr and white, black and red spheres at all panels represent hydrogen, carbon and oxygen atoms, respectively. During the period of 40.0 (fs) to 73.8 (fs) in Fig. 3.23, H5 (H10) move from right (left) to left (right) fragment.

We focus on the spatial distributions at 40.0 fs, 73.8 fs and 99.0 fs. Panels, (a1)-(a3) at 40.0 (fs) are the spatial distributions of bond order density of FAD, which is fluctuating around the stable state. As observed in the spatial distribution of the localized molecular orbitals at the optimized geometry, the double bond character localizing in C2=O1 and C7=O6 is obviously weak, and they fluctuate in space and time.

At 73.8 (fs), two protons, H5 and H10 are shifting from one site to the other, and by 99.0 (fs) the transfer is finished. One can see the shift of the double bonds being associated with the transfer, but again, the bond alternation proceeds in a mild manner. No dramatic change has been observed. On the other hand, it is almost a trivial task to confirm that bond order density for σ-electrons in the site of O-C-O keeps almost constant throughout.

Incidentally, in panels (b2) and (c2), we observe a smooth change of bond orders in O-H-O sites. In particular, they support the view of concerted reaction mechanism without generating radical centers. The spatial distribution in O-H-O looks like a three-center-two-electron bonding.

Thus we may say that FAD has already been prepared well so that it can exchange protons with no further need to drastically reorganize the electronic distribution and bonding status.

3.3.6 Bending motion of CH with respect to OCO plane assisting the π-bond fluctuation through sigma-bond to pi-conjugation

In Fig. 3.23, panel (a1) for $Z = -1.0$, a pretty high bond order density in H5-O3 and H10-O8 is noticed as though there are π-bonding in these sites. Of course this is not the case. However such a high density may arise due to out-of-plane motion of these OH bonds. Likewise we observe in panel (b1) in Fig. 3.23 that there is a similar effect of in between C2 and H4. The out-of-plane bending motion of C2-H4 seems to assist the delocalization or fluctuation of π-bond from C2=O3 to C2-O1. This effect reminds us of the hyperconjugation between a methyl functional group and benzene π-bonds.

We try to quantify this effect, that is the effect of the bending motion of CH on π-bond shift. To do so, we define the dihedral angles, θ_1 and θ_2 as follows:

$$\cos\theta = \frac{a_\alpha a_\beta + b_\alpha b_\beta + c_\alpha c_\beta}{\sqrt{a_\alpha^2 + b_\alpha^2 + c_\alpha^2}\sqrt{a_\beta^2 + b_\beta^2 + c_\beta^2}} \tag{3.3.11}$$

with

$$a_i x + b_i y + c_i z + d_i = 0, \qquad (i = \alpha, \beta) \tag{3.3.12}$$

where Eq. (3.3.12) is the equation of plane, α and β and the schematic picture of the angles is shown in panel (a) of Fig. 3.24. Next, we calculate the bond order density at the middle point between C7 and H9 and between C2 and H4 at $Z = \pm 1.0$ Bohr, that is, $(x, y, z) = (R_{\mathrm{H9}x} + |R_{\mathrm{H9}x} - R_{\mathrm{C7}x}|/2, R_{\mathrm{H9}y} + |R_{\mathrm{H9}y} - R_{\mathrm{C7}y}|/2, \pm 1.0)$, where $R_{\alpha i}$ is the i-th coordinate of atom α. Figure 3.24 shows the time-propagation of the angles, θ_1 and θ_2 in panel (b1) and (b2), respectively. The bond order density at the middle point of CH at $Z = \pm 1.0$ Bohr are shown in panel (c1) and (c2), which corresponds to the dynamics of θ_1 and θ_2.

In panel (c1) and (c2), we see the bond order densities at C7-H9 at $Z = 1.0$ Bohr and at H4-C2 at $Z = -1.0$ Bohr increase at 73fs, when two protons, H5 and H10 are just transferring at X_1 and $X_2 \simeq 0.5$. On the other hand, in panels (b1) we see a large out-of-bending motion for θ_1, which reaches up to about 20 degree from the molecular plane, while θ_2 doesn't almost change as in panel (b2). The bond-order density at $Z = \pm 1.0$ for C7-H9 is seen to well correlate with the bending motion in θ_1. In particular, at time 73 fs, we observe a high peak in the bond-order density for C7-H9 as seen in panel (c1), which is in accordance with the counter plot of the bond-order density of panel (b1) in Fig. 3.23.

In Fig. 3.25, we draw the bond-order density at time 73.11 fs at the planes of $Z = -1.0$ Bohr (panel (a1)) and 1.0 Bohr (panel (a2)). In between C4 and O2, we observe a high bond-order density in the plane of $Z = -1.0$ Bohr. Panel (a3) shows a side view of the bond-order density on the $x - z$ plane, which extends almost parallel to the axis of C2 and H4. A closer look at the density nearby H4 in panel (a3) strongly suggests that the σ bond of C2-H4 is noticeably mixed with the π bond character, which should be borrowed from the $2p_z$ orbital of C2. Note that in the present basis set, STO-6G, no p-type orbital is used for H4 atom. Conversely, it may be said that C2-H4 bond should commit the π-bonding systems through C2 atom. So far, however, we have not yet found a numerically clear evidence that such bending motion actually assists the delocalization of π-bonding in the site of O-C-O.

3.3.7 Global feature of electronic state remains almost constant: Snapshot of difference density

We here revisit the difference density, which we studied in Sec. 3.2.6 to confirm that a dramatic change in the electronic structure does not happen in the course of double proton transfer. It is defined in Eq. (3.2.7). The snapshot of the difference density at the planes of $z = -1.0$ (left column), $z = 0.0$ (central column), and $z = 1.0$ (right column) at time 40.0, 73.8, 99.0, and 144.9 fs are shown in Fig. 3.26. Again, the red and blue curves

represent the contour lines of positive and negative values, respectively. The vertical line segment in panel (a1) indicates 10.0 Bohrs. Red, black, and white spheres represent carbon, oxygen and hydrogen atoms, respectively.

A comparison of Fig. 3.26 with Fig. 3.19 shows that the topological features of them, the places of increasing and decreasing electrons, are essentially the same, whose physical interpretation was discussed in Sec. 3.2.6. The most outstanding feature in these figures therefore that (i) the spatial distribution of electrons has changed significantly on the occasion of dimerization of monomers, and moreover (ii) there is no qualitative difference after dimerization even when double proton transfer occurs. This characterizes a very important and essential aspect of double proton transfer in FAD.

3.3.8 Gross electron flux associated with proton transfer: Adiabatic electron flux

After all the endeavor in analyzing the essential feature of double proton transfer in terms of the static quantities, we are now getting into the final stage to summarize the mechanism of it. We here study the electron current induced in the molecular system in accordance with the proton transfers. As a quantity to capture such electron dynamics, we can consider Schiff's flux. This flux means probability current density (PCD), and we can track the motion of probability density. The Schiff's flux gives non-zero value for a complex-valued function, the complexity usually arise from the external time-dependent perturbation. The electronic wavepacket in SET is also usually a complex-valued function, which is driven by the nonadiabatic coupling with time-dependent nuclear motions. To attain the gross electron flow arising even from adiabatic electronic motion, we also apply the adiabatic flux, which has been proposed in Chapter 2.

Snapshots of the adiabatic flux

We here show the snapshots of adiabatic flux in Fig. 3.27. In this figure, blue arrow and contour line are adiabatic flux and the bond order density. In the left, middle, and right columns are the snapshots taken on plane $z = -1.0$, $z = 0.0$ and $z = 1.0$ (Bohr), respectively. Also, the first, second, third, and forth rows show the snapshots taken at time 69.0, 73.1, 76.0, and 81.0 (fs), respectively. Red, black and white spheres represent oxygen, carbon and hydrogen atoms. The bond order density with red and blue contours indicate positive and negative values, respectively. During the present period occurs the double proton transfer.

In panels (b1)-(b3) at time 73.1 fs, the adiabatic fluxes take the largest values, when the relative coordinates X_1 and X_2 takes almost 0.5, implying that the protons are just in the middle on the way of their shifting. Adiabatic flux in panel (b1) is directed from O6 to O8 and from O1 to O3, respectively. In panel (b2) generated is a vortex around each

atom, and that of panel (b2) is directed from O6 to O8 and from O1 to O3, respectively. This is an interesting dynamics that needs deeper study.

Although quite interesting, these raw data of the pointwise local flux have not revealed the gross electron flow that is synchronized with proton transfer. We therefore proceed to the following analyses, seeking for more qualitative behavior of the electron dynamics.

Definition of surface and time integrals: some practice for the flux calculations

The adiabatic flux is able to track the behavior for overlap distribution of electronic wavefunctions at time, t and $t + \Delta t$. We first define the surface integral of the adiabatic flux at x and y directions, $S_x^{(\mathrm{ad})}$ and $S_y^{(\mathrm{ad})}$ First, Adiabatic flux, $\boldsymbol{j}^{(\mathrm{ad})}(\boldsymbol{r}, t; \Delta t)$ is given by

$$\boldsymbol{j}^{(\mathrm{ad})}(\boldsymbol{r}, t; \Delta t) = \mathrm{Im}\left[\boldsymbol{J}\left(\boldsymbol{r}, t; \Delta t\right)\right], \tag{3.3.13}$$

where $\boldsymbol{J} \equiv \vec{J}$ and $\boldsymbol{J}$ is defined in Eq. (2.4.3). By using Eq. (2.4.3), we define the following form

$$\left.\begin{aligned} S_x^{(\mathrm{ad})}\left(x_0, t\right) &= \int_{S_2} dydz J_x^{(\mathrm{ad})}\left(x_0, y, z, t; \Delta t\right) \\ S_y^{(\mathrm{ad})}\left(y_0, t\right) &= \int_{S_1} dxdz J_y^{(\mathrm{ad})}\left(x, y_0, z, t; \Delta t\right), \end{aligned}\right\} \tag{3.3.14}$$

where x_0 and y_0 are points at x and y coordinates in the Cartesian coordinates, respectively, and the integrals of Eq. (3.3.14) mean the integral quantities of time-shift overlap distribution, which passes through the surface, S_1 and S_2 at $x = x_0$ and $y = y_0$, respectively. In our numerical calculations, points x_0 and y_0, and surfaces S_1 and S_2 are selected such that

$$S_1 = \left\{\begin{array}{c} -2.0 + \dfrac{|R_{\alpha x} - R_{\beta x}|}{2} \leq x \leq 2.0 + \dfrac{|R_{\alpha x} - R_{\beta x}|}{2}, \\ \\ y_0 = \dfrac{|R_{\alpha y} - R_{\beta y}|}{2}, \\ \\ -2.0 + \dfrac{|R_{\alpha z} - R_{\beta z}|}{2} \leq z \leq 2.0 + \dfrac{|R_{\alpha z} - R_{\beta z}|}{2}, \\ \\ (\alpha, \beta) = (\mathrm{O1},\ \mathrm{O8}) \ \text{and} \ (\mathrm{O3},\ \mathrm{O6}) \end{array}\right. \tag{3.3.15}$$

and

$$S_2 = \begin{cases} x_0 = \dfrac{|R_{\alpha x} - R_{\beta x}|}{2}, \\ -2.0 + \dfrac{|R_{\alpha y} - R_{\beta y}|}{2} \leq y \leq 2.0 + \dfrac{|R_{\alpha y} - R_{\beta y}|}{2}, \\ -2.0 + \dfrac{|R_{\alpha z} - R_{\beta z}|}{2} \leq z \leq 2.0 + \dfrac{|R_{\alpha z} - R_{\beta z}|}{2}, \\ (\alpha, \beta) = (\mathrm{O1}, \mathrm{C2}),\ (\mathrm{O3}, \mathrm{C2}),\ (\mathrm{O6}, \mathrm{C7}) \text{ and } (\mathrm{O8}, \mathrm{C7}) \end{cases} \tag{3.3.16}$$

where $R_{\alpha i}$ is the i-th component at classical nuclear position of α atom. Next, we define the time integral of Eq. (3.3.14) by

$$\left.\begin{aligned} Q_x^{(\mathrm{ad})}(y_0, t) &= \int_{t_0}^{t} d\tau S_x^{(\mathrm{ad})}(y_0, \tau) \\ Q_y^{(\mathrm{ad})}(x_0, t) &= \int_{t_0}^{t} d\tau S_y^{(\mathrm{ad})}(x_0, \tau), \end{aligned}\right\} \tag{3.3.17}$$

where t_0 means initial time and τ is time variable later than t_0. The numerical integral of Eq. (3.3.14) is approximated by the sum

$$\int_a^b dx f(x) \cong \sum_{i=1}^{n} \Delta x_i f(x_i), \tag{3.3.18}$$

where x_i is coordinate, $f(x_i)$ is integrand at x_i and $\Delta x_i = x_{i+1} - x_i$. In the present calculations of Eq. (3.3.14), we select Δx_i, Δy_i and Δz_i of Eq. (3.3.18) with 0.0667 Bohrs and select the integral region in x, y and z axes to be 4.0 Bohrs. The time-shift Δt of time is set to 30 as.

Net electron flow

In Fig. 3.28, we show the time dependence of the surface integral at time t, panels (a1) - (a6); the results of Eq. (3.3.14), where panels (a1), (a2), (a3), and (a4) are for $S_y^{(\mathrm{ad})}(y_0, t)$ taken at O6-C7, O8-C7, O3-C2 and O1-C2, respectively, whereas panels (a5) and (a6) are for $S_x^{(\mathrm{ad})}(x_0, t)$ taken at O3-O6 and O1-O8, respectively. They are plotted against time in units of fs. At these panels, the behavior of Eq. (3.28) fluctuates rapidly around zero and also, the amplitude of $S_y^{(\mathrm{ad})}(y_0, t)$ is higher than the one of $S_x^{(\mathrm{ad})}(y_0, t)$. This fact means that the behavior of electronic state between O1 and O3, and between O6 and O8 are larger than the one between lines O1-O8 and O3-O6.

Panel (b1) - (b3) represent the resultant value of Eq. (3.3.17), which is the total amount of current that is accumulated up to time t. Red and green curves in panel (b1)

are for $S_y^{(\mathrm{ad})}(y_0,t)$ of surfaces, O6-C7 and O3-C2, respectively, those at panel (b2) are for $S_y^{(\mathrm{ad})}(y_0,t)$ of surface, and finally O8-C7 and O1-C2 in panel (b3) are for $S_x^{(\mathrm{ad})}(x_0,t)$ of surface, O3-O6 and O1-O8. In the calculation of Eq. (3.3.17), the numerical integration was performed with Eq. (3.3.18) choosing Δt to be 0.18 fs.

The surface integrals in panels (a1) - (a4) represent the flux passing through the cross section in between C and O atoms (four places), which monitors the electron flow associated mainly with the π-bond fluctuation. They actually oscillate around the value of zero with a period of about 20 fs. (The very fine oscillation comes from attosecond level fluctuation of the quantum phase and is not very interesting in the present context.)

On the other hand, the surface integral in panels (a5) and (a6) detects the flow passing through a cross section in between O-H-O sites (hydrogen bonding sites). These quantities also show an oscillation, which is more rapid (period is about 8 fs) with smaller amplitudes.

To quantify the gross flow of these flowing electrons with fluctuation, we show accumulated quantities of the surface integral as in panels (b1) - (b3). In panels (b1) and (b2), a clear change in the behavior of $Q_y^{(\mathrm{ad})}$ is found at about 70 fs, which is the time of proton transfer. That is, those for O6-C7 and O8-C7 are reduced and keep negative after then. Conversely, the accumulated flux in O3-C2 and O1-C2 increase and remain positive afterwards. These results indicate a net flow of electrons in the direction of O1→C2→O3 and O6→C7→O8.

Likewise, panel (b3) of this figure indicates a net electron flow in the transferring proton area in such directions as O3→H5→O6 and O8→H10→O1. Therefore, we have a global and cooperative flow in the counterclockwise direction. See Fig. 3.30. [Recall the discussion of Sec. 3.2.6.2, which suggests a clockwise electron flow in the dimerization process from two FAM to FAD.]

3.3.9 Schiff's flux of electrons induced by nonadiabatic interaction

Finally we apply the same analysis in terms of the Schiff flux, which is induced by nonadiabatic transition. In Fig. 3.29, we show the results of surface and time integrals that the integrand of Eq. (3.3.14) for Schiff's flux are defined as Eq. (2.2.7). In the present calculation, Eq. (2.2.11) for the ground electronic state has been solved. We have applied the same analyses as above to the Schiff flux.

Panel (a1)-(a4) in Fig. 3.29 are $S_y(y_0,t)$ for the surfaces set in O6-C7, O8-C7, O3-C2 and O1-C2, respectively. Panel (a5) and (a6) are for $S_x(x_0,t)$ of the surfaces in O1-O8 and O3-O6, respectively. Here again the positive values of $S_x(x_0,t)$ and $S_y(y_0,t)$ means that the probability density goes through the defined surface to the positive direction in x and y axes, respectively.

Panel (b1)-(b3) in Fig. 3.29 show the time series of $Q_x(x_0,t)$ and $Q_y(y_0,t)$ on surfaces

O6-C7, O3-C2, O8-C7, O1-C2, O3-O6, and O1-O8, where red and green lines of panel (b1) are $Q_y(y_0, t)$ of surfaces O6-C7 and O3-C2, respectively. Likewise those of panel (b2) are for the surfaces in O8-C7 and O1-C2, respectively, and those of panel (b3) are for $Q_x(x_0, t)$ of the surfaces O3-O6 and O1-O8, respectively.

It is interesting to compare the panels (a1)-(a6) of 3.29 with those in Fig. 3.28. An inspection reveals that the Schiff flux oscillates far quickly, and there is no fluctuation of longer scale in contrast to the adiabatic flux. Then we integrate them to accumulate the net current in the Schiff flux. In panel (b1)-(b3), we observe a qualitative change in the behaviors of $Q_x(x_0, t)$ and $Q_y(y_0, t)$ around 70 fs. However, $Q_y(y_0, t)$ on surfaces, O6-C7 and O8-C7 become positive values, and that of surfaces O8-C7 and O1-C2 become negative. This means the fluxes are directed in O8→C7→O6 and O3→C2→O1.

On the other hand, $Q_x(x_0, t)$ on surfaces O3-O6 and O1-O8 become negative and positive values, respectively, although they undergo fluctuation till 100 fs. Thus it turns out that the induced electron flux is directed in O3→H5→O6 and O8→H10→O1, which are the directions of proton transfers nearby them. (See Fig. 3.31.)

In the present system, the mixing of the excited state configurations in the SET wavepacket dynamics happens to be small, which implies that the effect of the nonadiabatic coupling must be small. Therefore the nonadiabatically induced electron flow as detected by the Schiff flus is expected to be small. On the other hand, the adiabatic flux is regarded as a total flux that arise from all the net movement of an electron wavepacket including the nonadiabatically induced motion. Therefore the gross flux discussed in the above subsection should represent the global feature of entire electron flux.

3.4 Summary of the dynamics: monomers to dimer, and double proton transfer: Concluding remarks

The reaction mechanism of double proton transfer in formic acid dimer (FAD) consists of two stages; (i) dimerization of monomers (FAM) to FAD, and (ii) proton transfer in the dimer. It turns out that each is composed of the following substeps, which are not necessarily sequential.

i) Dimerization process:

1. A large electronic reorganization takes place in the dimerization process: (1) The double bond C=O in FAM is weakened and π-electrons are massively delocalized to the single bond region of C-O. Although the distinction between stronger double bond (the former C=O) and weaker one (the former C-O) can be made, they are found to fluctuate. (This fluctuation seems to be assisted by the out-of-plane bending motion of the adjacent CH σ-bond.

2. A large reorganization on the four oxygen atoms: The lone pair on O atoms lying on the molecular plane and directed towards a coming-in proton is reduced in the electronic population. Instead a character of σ-bonding to create the new OH bond grows there. This is essentially a transformation from sp^2 to sp^3 hybridization. Due to this reorganization, the population on these O atoms is reduced. On the other hand, the population on the other set of O atoms is found to increase. This is due to the opposite reorganization, that is, decrease of the character of OH σ-bonding and increase of the character of lone pair, transformation of sp^3 to sp^2 hybridization.

3. Due to the π-delocalization and reorganization in σ-bonding by re-hybridization, electrons should flow in the opposed direction to the forthcoming proton transfers. [Clockwise direction in our molecular setting.]

4. The electronic reorganization thus far to make a dimer let FAD prepare for protons to transfer easily. In case that the above processes are well achieved within FAD, the dimerization energy is deeper and the barrier height for proton transfer (the energy of the transition state) should be lower.

5. It seems that our used basis set STO-6G is particularly favorable in this aspect. Indeed, the molecular orbitals at the optimized geometry is very close to those of the transition states. Particularly interesting feature of some of MOs is that there seems to exist a three-center-two-electron bonding in the site of O-H-O, which looks like a single tube extending over the region. It is readily expected that proton can shift from one O atom to the other through these electron-deficient-like bonding.

ii) Proton transfer process from above formed FAD:

1. First of all, we have precluded the possibility of the mechanism of hydrogen-atom migration in terms of the unpaired electron density. So, the electrons are essentially paired irrespective of their partial population on the atomic sites.

2. In the above electronic status prepared in FAD, the proton nuclei shift their positions as though passing through the three-center-two-electron MO tube. In this passage, the individual nucleus protons carry a pretty much amount of electrons (ca. 0.7 in the present case) as indicated in the Mulliken population analysis. Recall that the inverse electron flow has already taken place in the dimerization process as above.

3. Only a small amount of electrons is carried over from the old CH bonding site to the new CH bonding site.

4. Concomitantly, the double bonds of C=O, which are already delocalized to somewhat a large extent, are also shifted to the old C-O bonding sites.

5. These electron flow is collectively directed in the same direction of proton movement. [Anticlockwise in our setting.]

6. The souble proton transfer is completed.

In the present calculations with use of STO-6G, the above two processes have been clearly recognized, which happen to be nice for analysis. However, for other basis sets, the above two processes may take place almost simultaneously, where the shallower dimerization energy and higher potential barrier for proton transfer. In such a case, the electron flux might be a superposition of those of clockwise and anticlockwise directions.

Finally, let us consider the receding process of FAD after double proton transfer. This is exactly the reverse process of the dimerization summarized above. Therefore, the substeps there take place in time reversal way. For instance, the electron current should be observed in the anticlockwise direction, which would push most of the clockwise flow backwards. In this series of events (dimerization, double proton transfer, dissociation), therefore, net flow of electrons come from the event of proton transfer, which is anticlockwise flow, as described above.

Thus we have attained a clear insight about the dynamical mechanism of double proton transfer through the study with electron wavepacket dynamics.

References

[1] I. Blevich, M. I. Verkhovsky and M. Wikström, Nature **440**, 829 (2001).

[2] R. Raymond and H. Cheng, J. Chem. Phys. **111**, 2086 (1998).

[3] C. Dellago, M. M. Naor and G. Hummer, Phys. Rev. Lett. **90**, 105902 (2003).

[4] A. E.Bragg, J. R. R. Verlet, A. Kammrath, O.Cheshnovsky and D. M. Neumark, Science **306**, 669 (2004).

[5] C. Marcelo, G. de Godoy and S. Cukierman, J. Chem. Phys. **81**, 1430 (2001).

[6] H. Ushiyama, K. Takatsuka, Angew. Chem. Int. Ed. **46**, 587 (2007).

[7] M. Amano and K. Takatsuka, J. Chem. Phys. **122**, 084113 (2005).

[8] H. D. Meyer, W. H. Miller, J. Chem. Phys. **70**, 3214 (1979).

[9] S. Hayashi, J. Umemura, S. Kato and K. Morokuma, J. Phys. Chem. **88**, 1330 (1984).

[10] Y. Cheng, Y. Yamaguchi, W. H. Miller and H. F. Schaefer III, J. Am. Chem. Soc. **109**, 7245 (1987).

[11] P. Svensson, N. Bergman, P. Ahlberg, J. Chem. Soc. Commun. 862 (1990).

[12] Ö. Birer and M. Havenith, Annu. Rev. Phys. Chem. **60**, 263 (2009).

[13] N. Shida, P. F. Barbara and J. Almöf J. Chem. Phys. **94**, 3633 (1990).

[14] H. Ushiyama, K. Takatsuka, J. Chem. Phys. **115**, 5903 (2001).

[15] H. W. Schmidt, K. K. Baldridge, J. A. Boatz, S. T. Elbert, M. S. Gordon, J. H. Jensen, S. Koseki, N. Matsunaga, K. A. Nguyen, S. J. Su, J. Comput. Chem. **14**, 1347 (1993).

[16] J. Paldus, J. Chem. Phys. **61**, 5321 (1974).

[17] J. Paldus, Int. Quant. Chem. Quantum Chem. Symp. **9**, 1650 (1975).

[18] J. Paldus, Phys. Rev. A **14**, 1620 (1976).

[19] I. Shavitt, Int. Quant. Chem. Quantum Chem. Symp. **11**, 131 (1977).

[20] I. Shavitt, Int. Quant. Chem. Quantum Chem. Symp. **12**, 5 (1978).

[21] T. Yonehara and K. Takatsuka, Chem. Phys. In press.

[22] J. M. Foster and S. F. Boys, Rev. Mod. Phys. **32**, 300 (1960).

[23] C. Edmiston and K. Ruedenberg, Rev. Mod. Phys. **35**, 457 (1963).

[24] S. Yamabe, K. Kitaura and N. Nishimoto, Theoret. Chim. Acta (Berl) **47**, 111 (1978).

[25] Y. Yamaguchi, Y. Osamura, J. D. Goddard and H. F. Schaefer III, *A New Dimension to Quantum Chemistry : Analytic Derivative Methods in Ab initio Molecular Electronic Structure Theory*, (Oxford university press, New York, Oxford 1994).

[26] E. R. Davidson, *Reduced Density Matrices in Quantum Chemistry*, (Academic press, New York, San Francisco, London 1976).

[27] A. Szabo and N. Ostlund, *Modern Quantum Chemistry*, (Dover, Mineola, New York 1996).

[28] K. Takatsuka, T. Fueno, K. Yamaguchi, Theoret. Chim. Acta(Berl.). **48**, 175 (1978).

[29] V. N. Staroverov and E. R. Davidson, Chem. Phys. Lett. **330**, 161 (2000).

[30] M. H-Gordon, Chem. Phys. Lett. **372**, 508 (2003).

Table 3.1: Bond lengths and angles of FAD (formic acid dimer) at the stable state (SS) and transition states (TS), along with those of FAM (formic acid monomer). $R_{\mathrm{A_IB_J}}$ is the internuclear distance between I-th A atom and J-th B atom, and angle $\mathrm{A_IB_JC_K}$ denotes the angle between lines $\mathrm{A_IB_J}$ and $\mathrm{B_JC_K}$. The molecules are all on a plane.

	FAD(SS)	FAD(TS)	FAM(SS)
R_{O1C2}	2.382 (Bohr)	2.416 (Bohr)	2.357 (Bohr)
R_{O3C2}	2.456	2.415	2.622
R_{H4C2}	2.079	2.079	2.075
R_{H5O3}	2.007	2.215	1.870
R_{H5H10}	4.288	4.288	
X_1	0.556	0.500	
X_2	0.444	0.500	
∠O3C2O1	127.0°	127.3°	123.4°
∠C2O1H10	118.7	114.9	
∠O3H5O6	177.5	177.1	
∠O3C2H4	116.0	116.4	111.3
∠C2O3H5	111.8	115.0	103.1

Table 3.2: Dimerization energy (FAM to FAD), ΔE_d and barrier height ΔE_b for double proton transfer given by CISD with the basis sets STO-6G, STO-6G(p), STO-6G(p(H5H10)) and 3-21G.

Computational level	ΔE_d (kcal/mol)	ΔE_b (kcal/mol)
CISD/STO-6G	39.1	0.3
CISD/STO-6G(p)	4.2	8.0
CISD/STO-6G(p(H5H10))	4.0	7.1
CISD/3-21G	16.9	8.5
experimental	12.72	

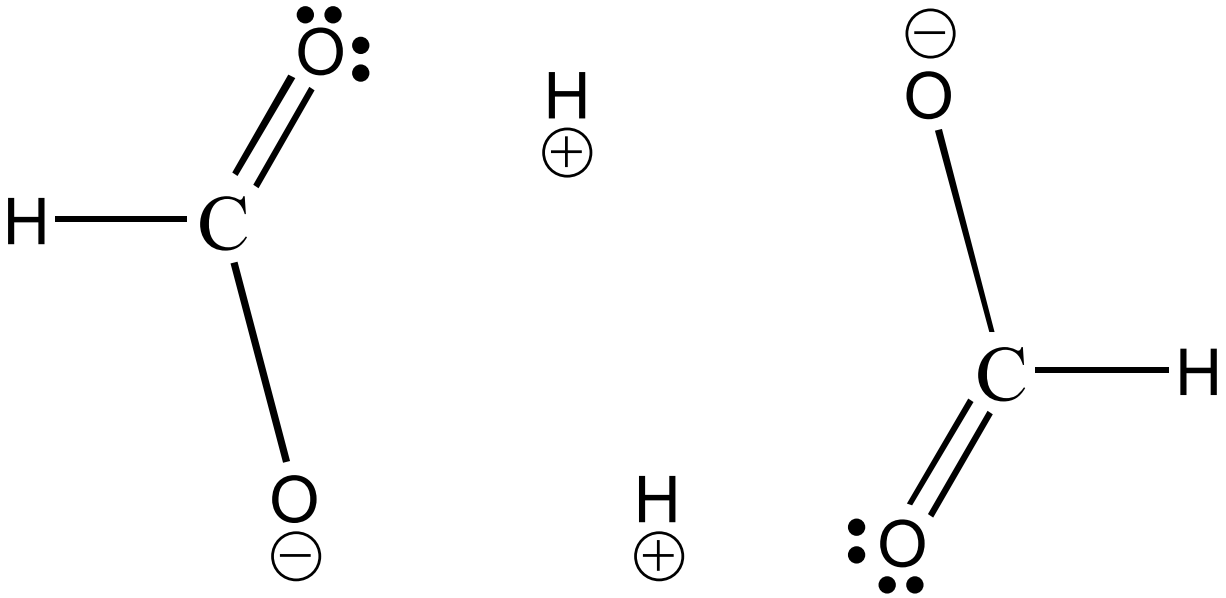

Figure 3.1: Schematic picture for double proton transfers.

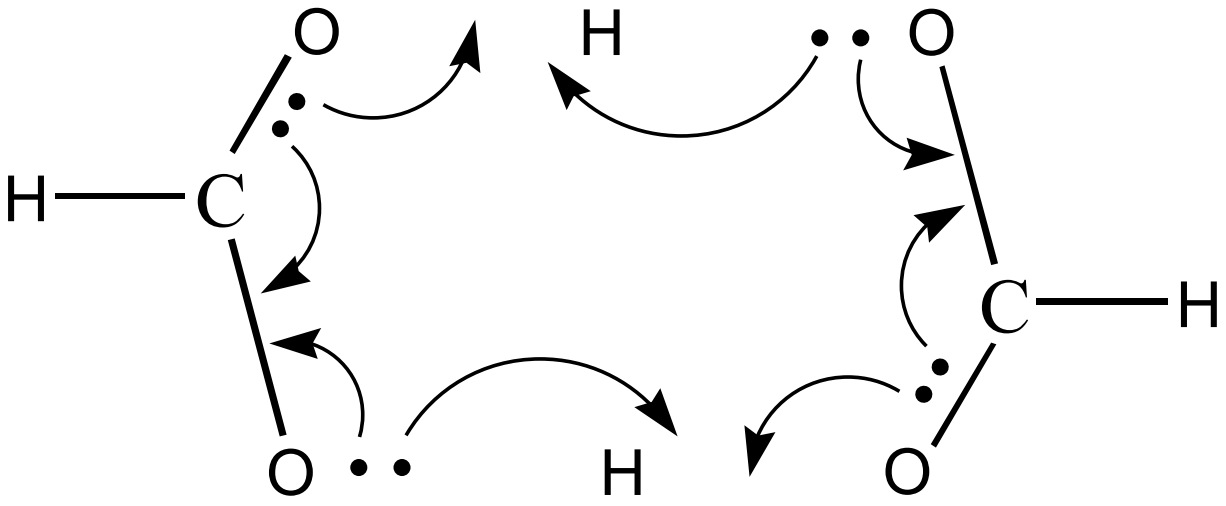

Figure 3.2: Schematic picture for hydrogen-atom migrations.

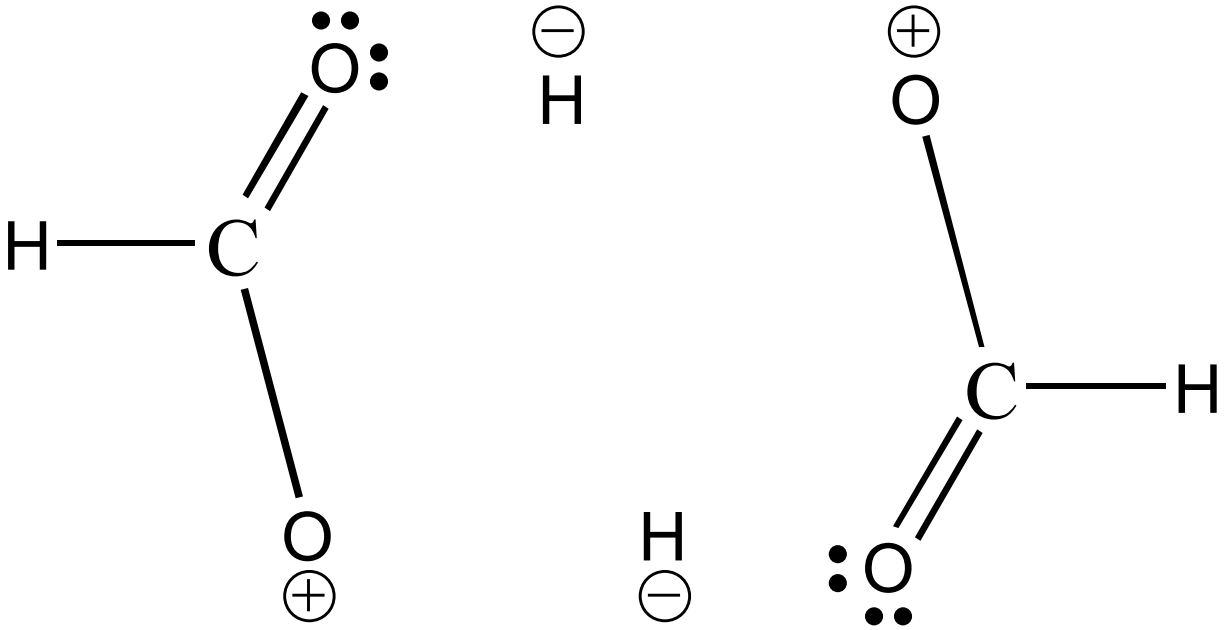

Figure 3.3: Schematic picture for hydrid transfers.

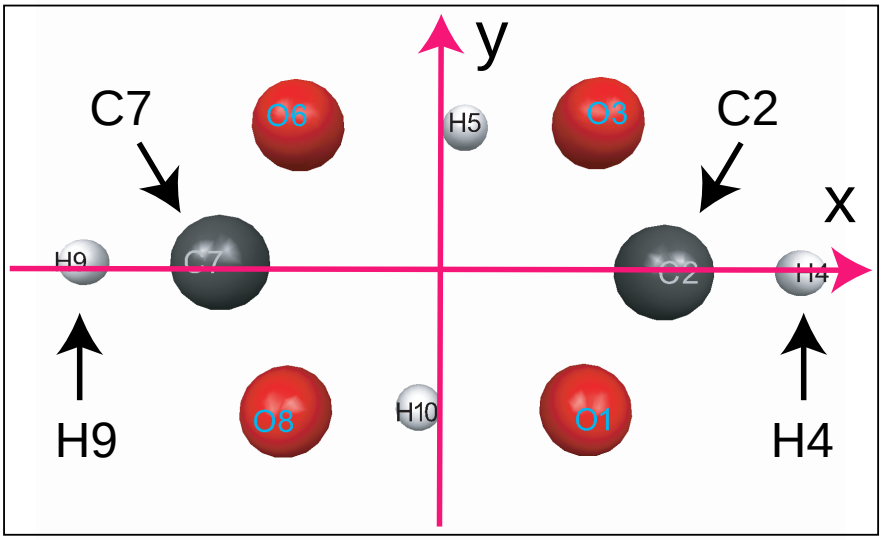

Stable state

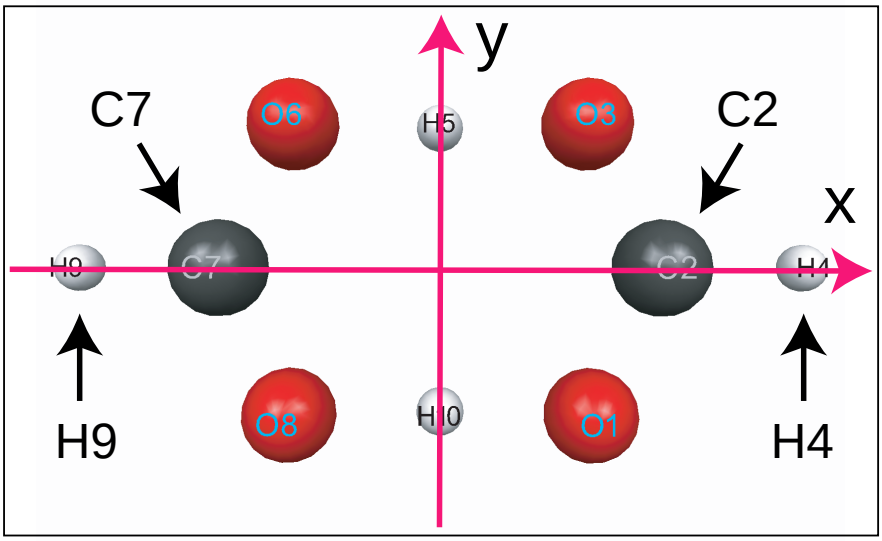

Transition state

Figure 3.4: Schematic pictures of FAD in the stable state (upper panel) and transition states (lower). The atomic configuration in the upper panel serves as an initial geometry before proton transfer. This numbering of the atoms is used throughout.

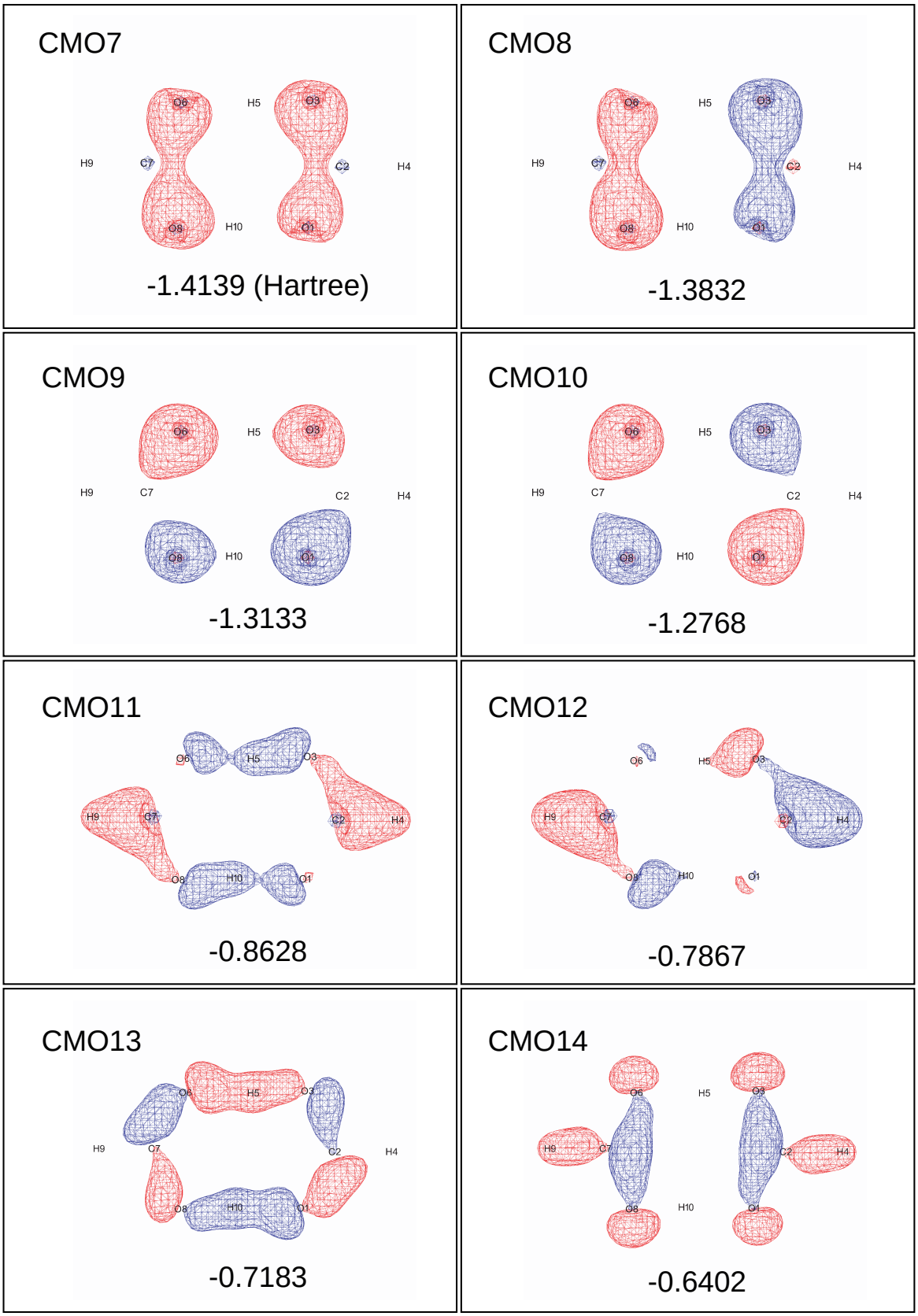

Figure 3.5: Spatial distribution of canonical molecular orbitals (CMO) for FAD in the stable state (SS). The number in each box indicates the corresponding orbital energy (in Hartree). The red and blue curves represent positive and negative values, respectively. CMO24 is HOMO.

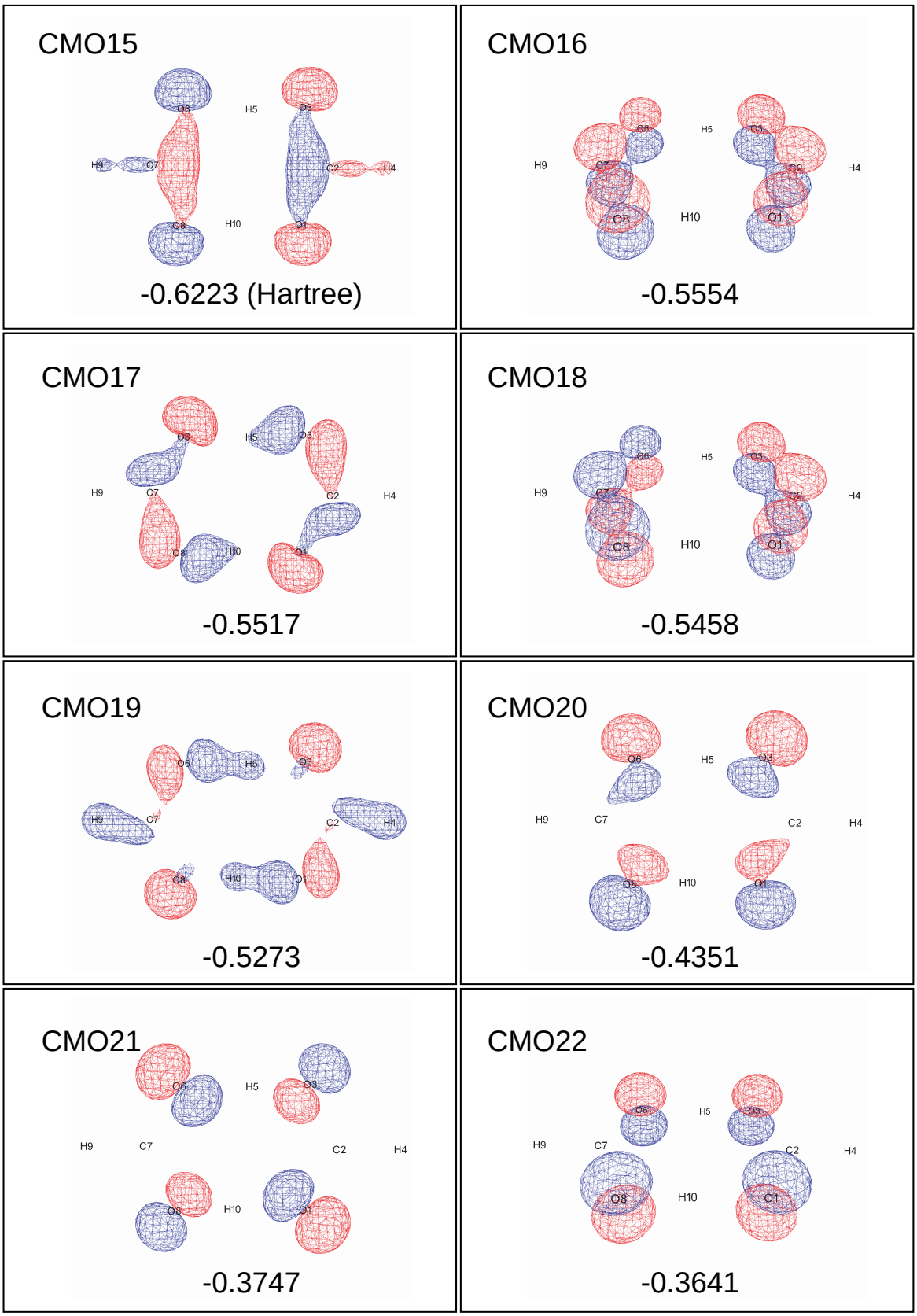

Figure 3.6: Spatial distribution of CMO for FAD in SS. Continued.

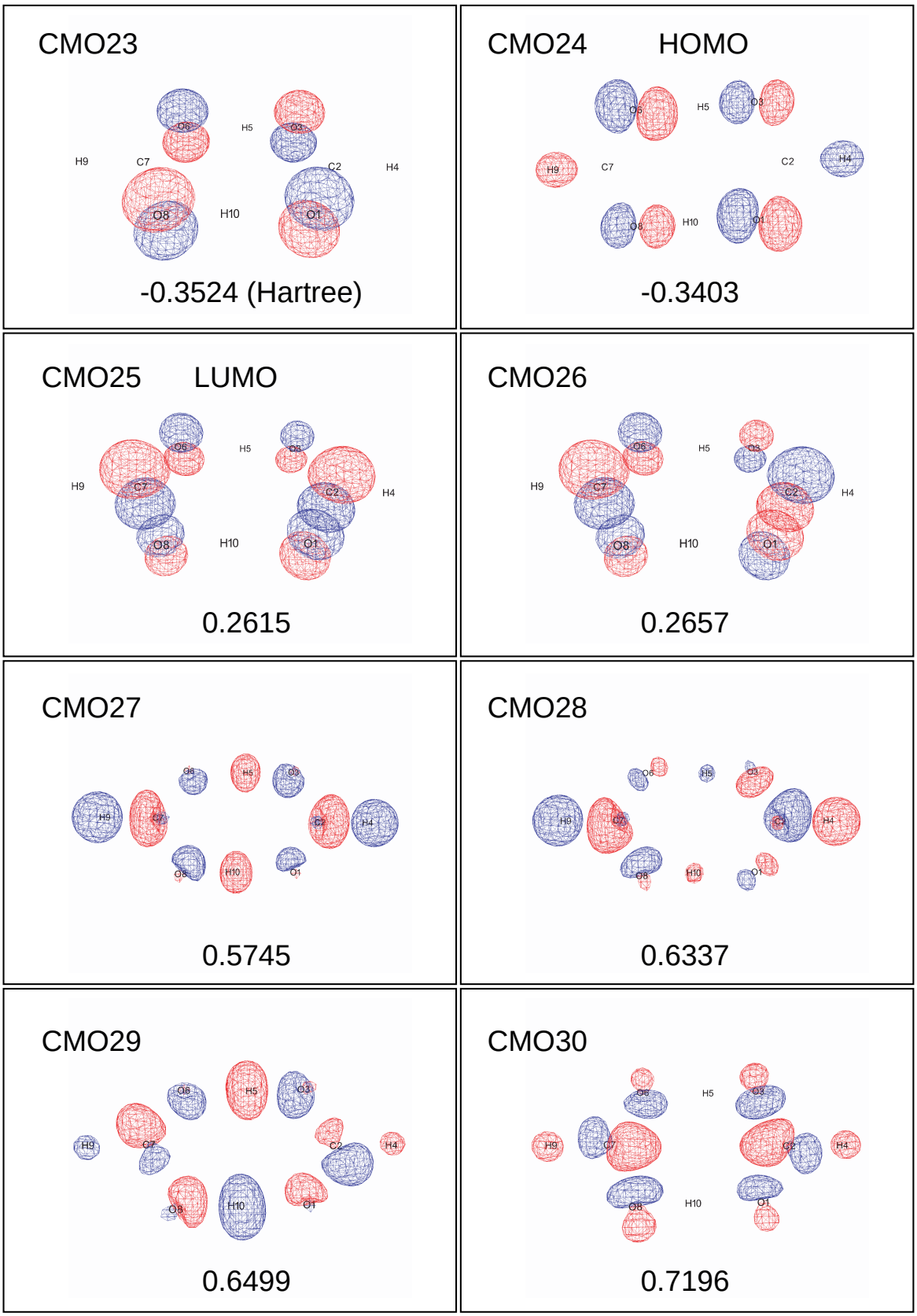

Figure 3.7: Spatial distribution of CMO for FAD in SS. Continued.

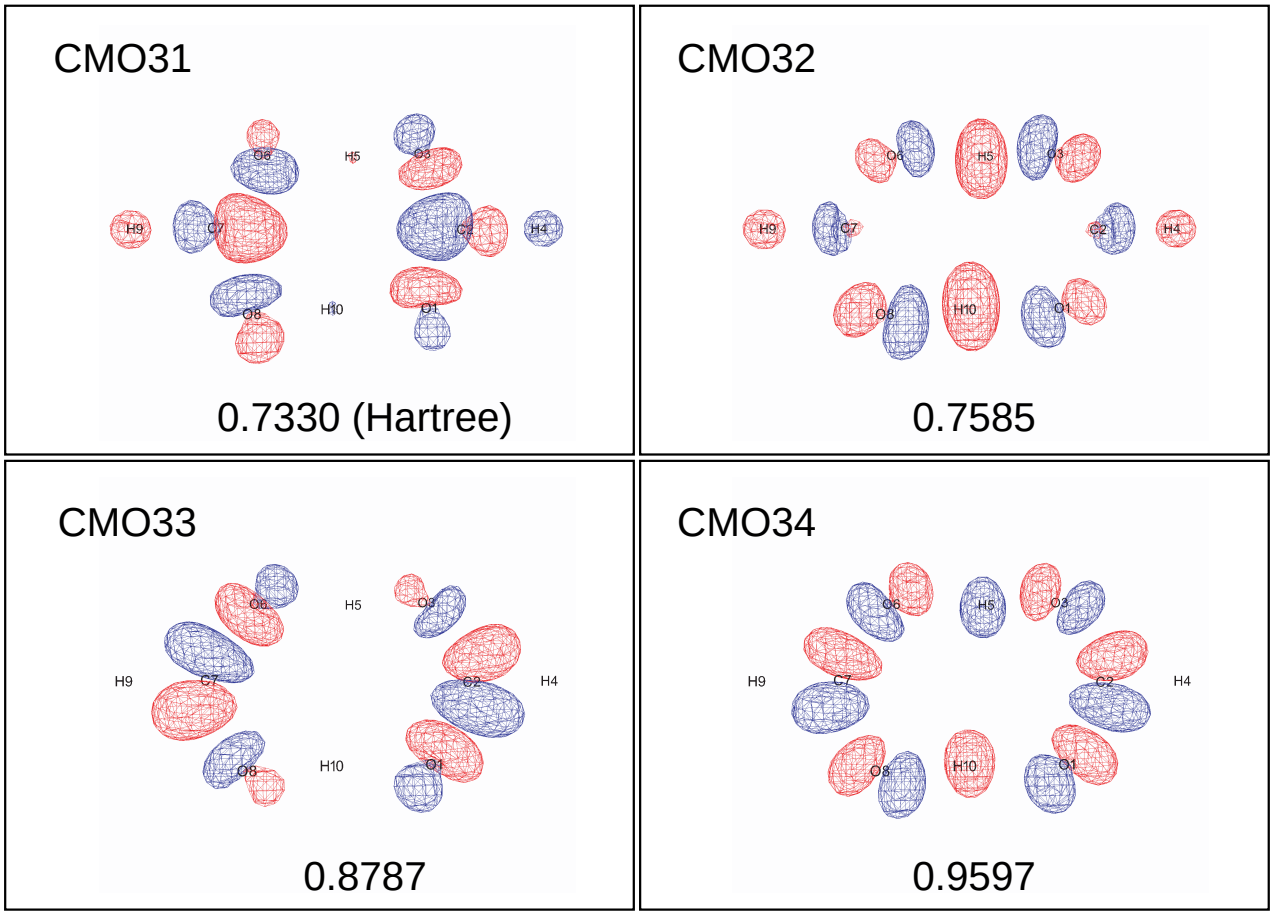

Figure 3.8: Spatial distribution of CMO for FAD in SS. Continued.

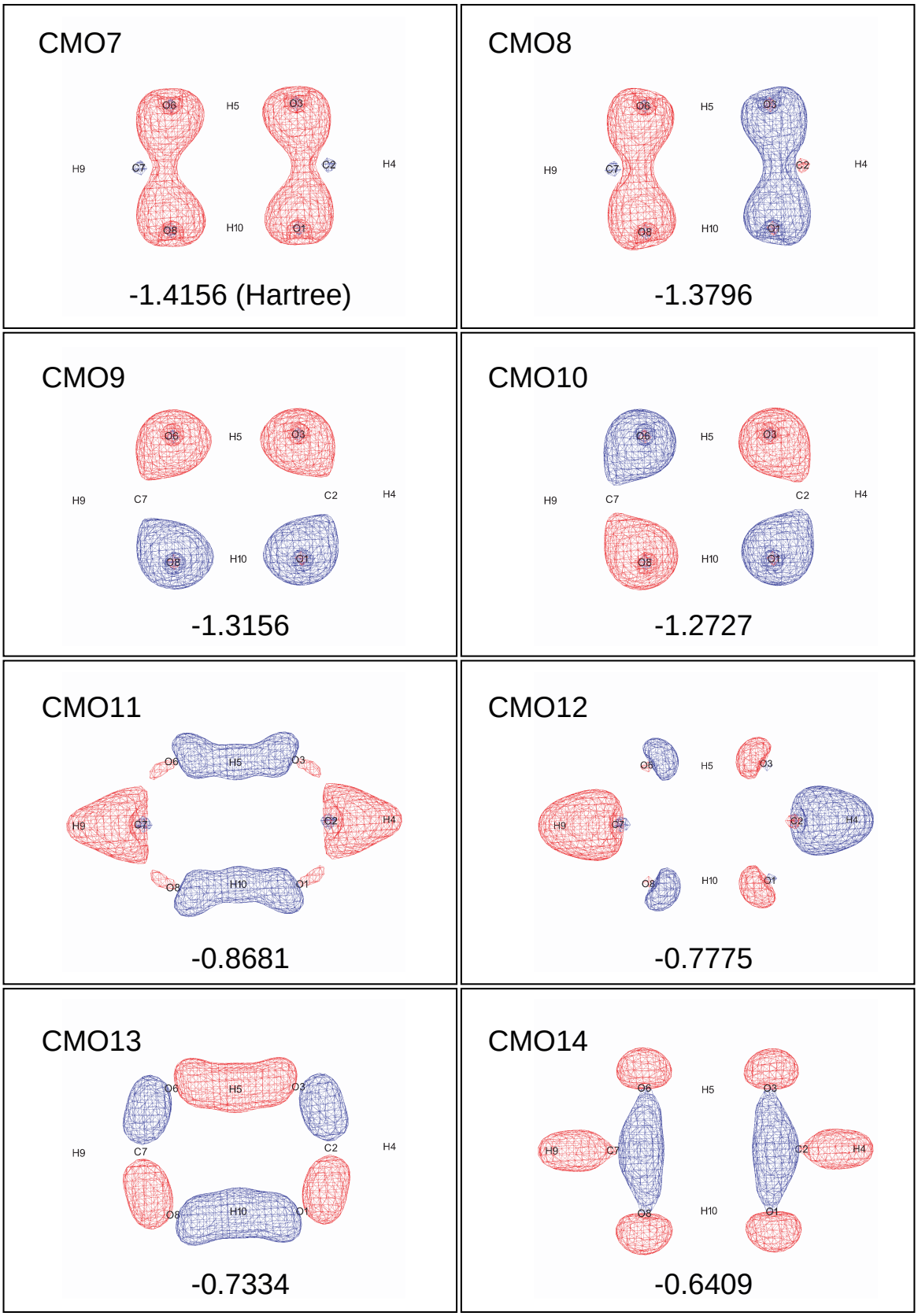

Figure 3.9: Spatial distribution of canonical molecular orbitals (CMO) for FAD in the transition state (TS). The number in each box indicates the corresponding orbital energy (in Hartree). The red and blue curves represent positive and negative values, respectively. CMO24 is HOMO.

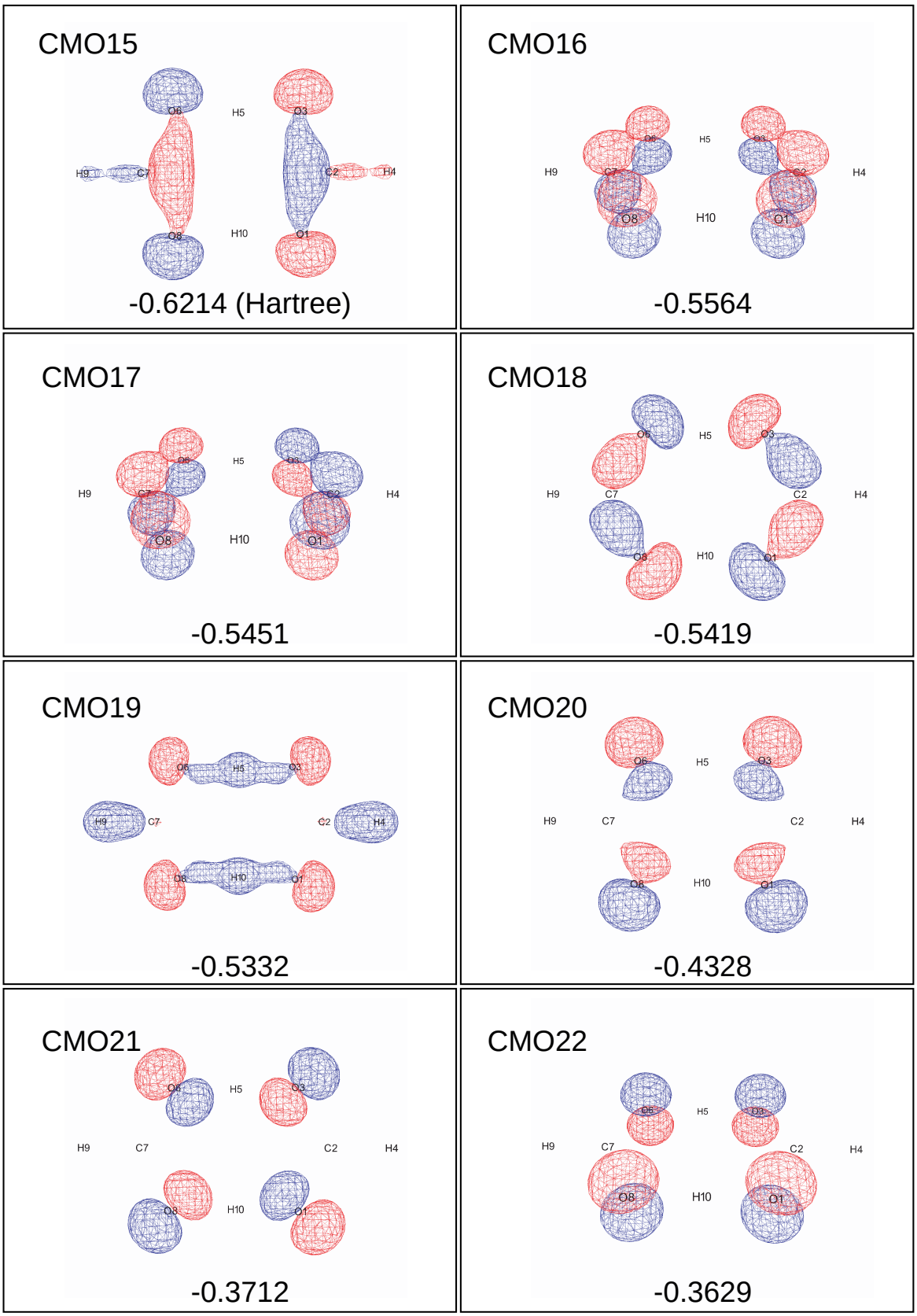

Figure 3.10: Spatial distribution of CMO for FAD in TS. Continued.

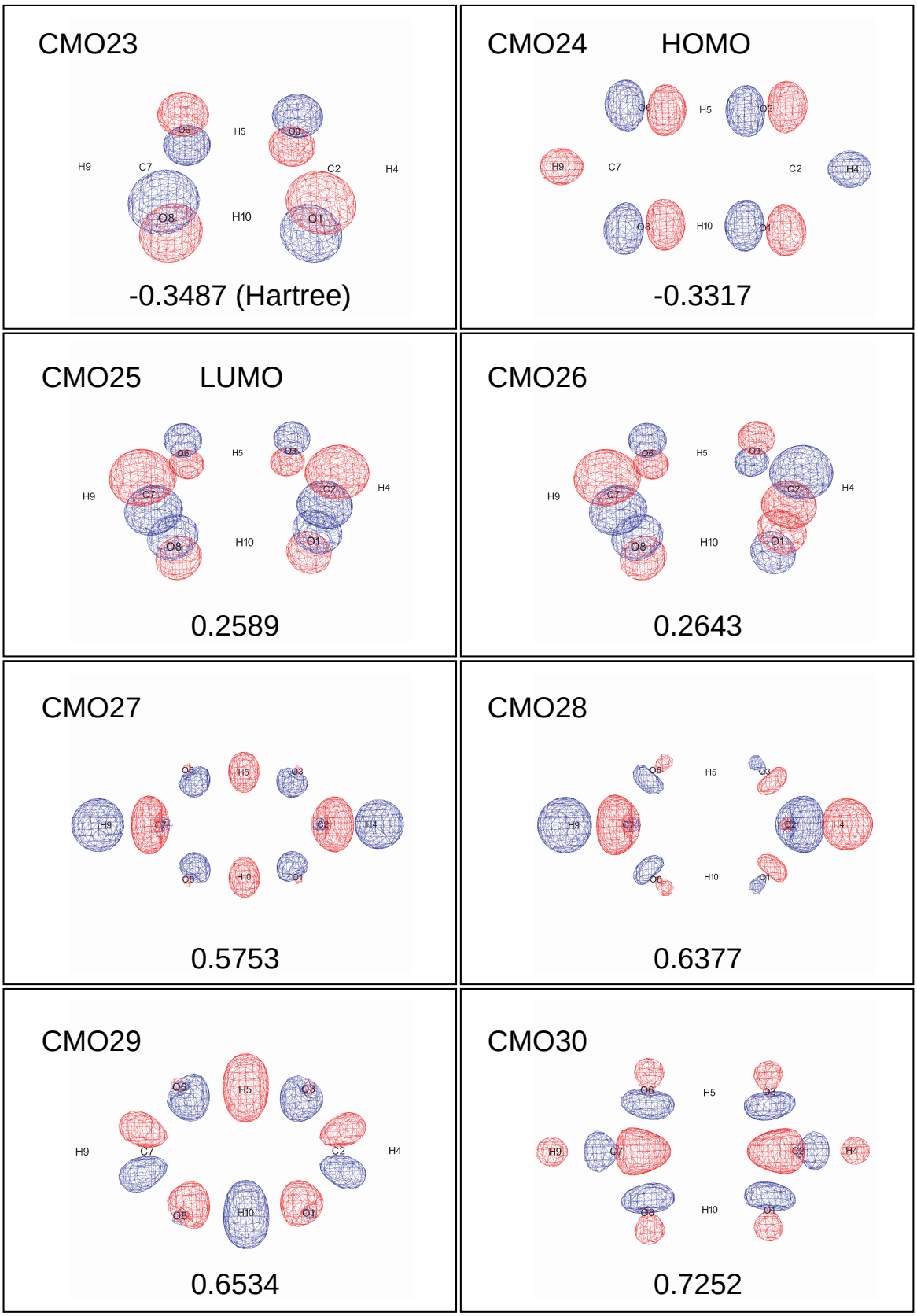

Figure 3.11: Spatial distribution of CMO for FAD in TS. Continued.

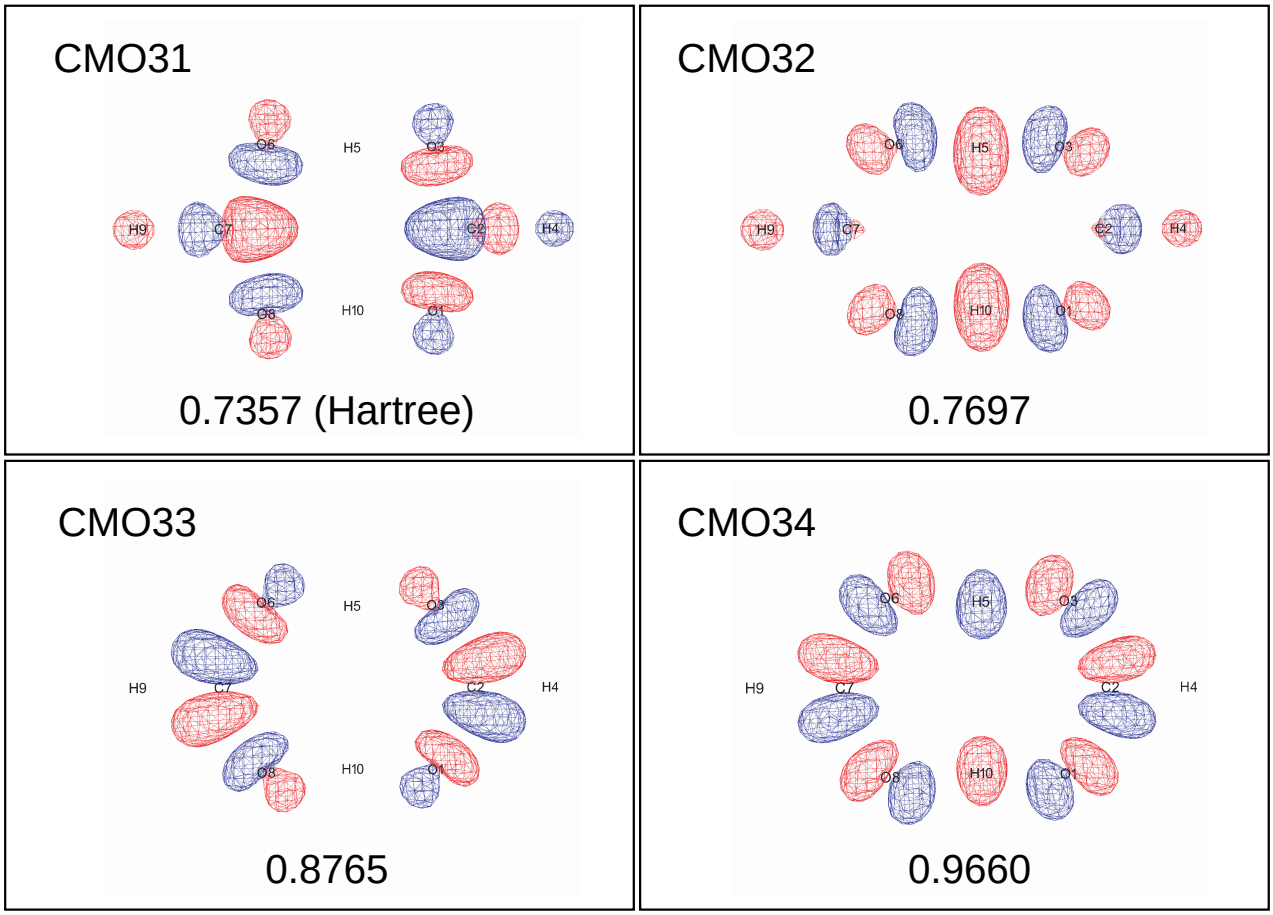

Figure 3.12: Spatial distribution of CMO for FAD in TS. Continued.

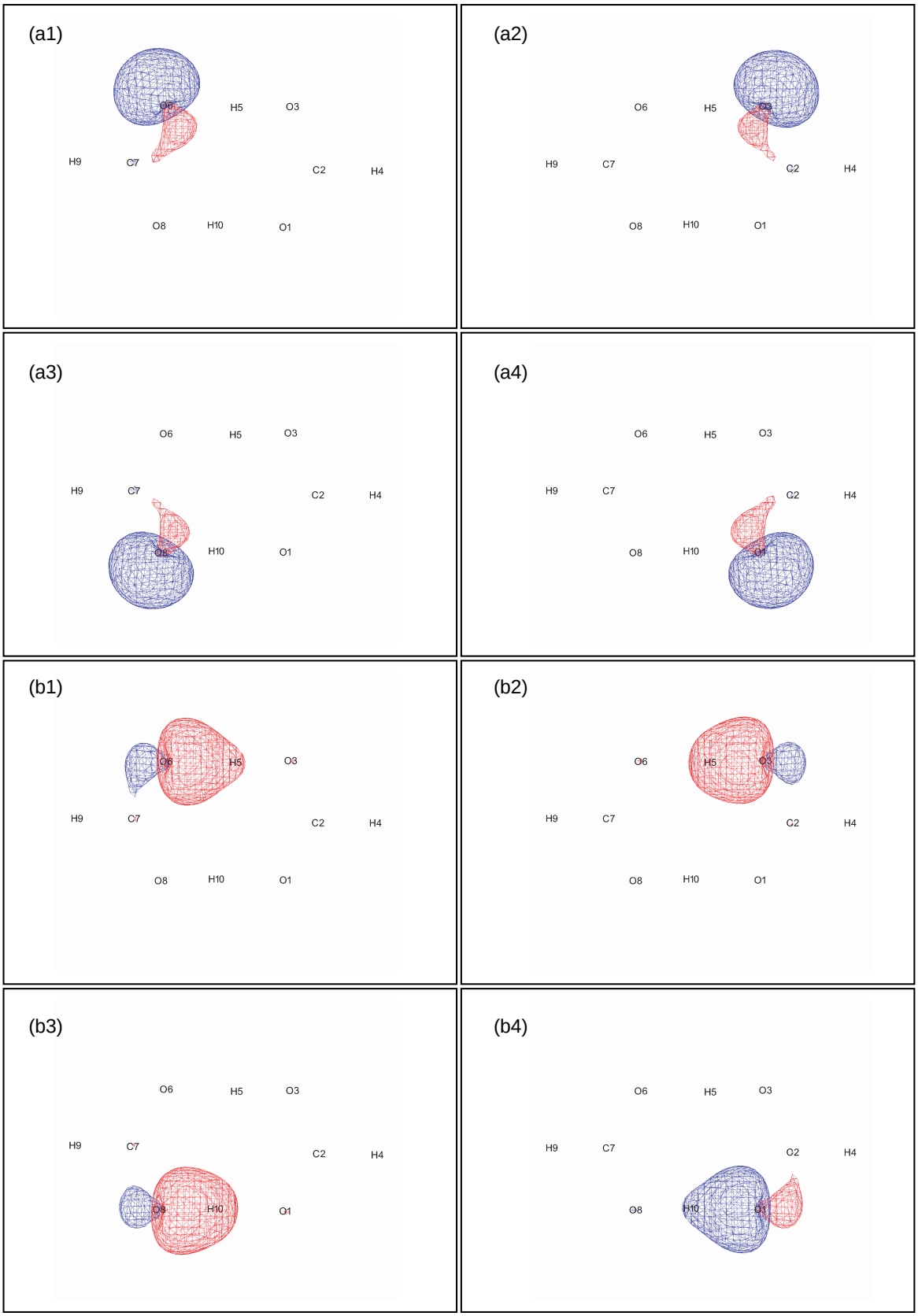

Figure 3.13: Spatial distribution of Boy's LMO for FAD in the stable state (SS). The red and blue curves represent positive and negative values, respectively. Only the occupied orbitals excep for the 1s core of C and O atoms.

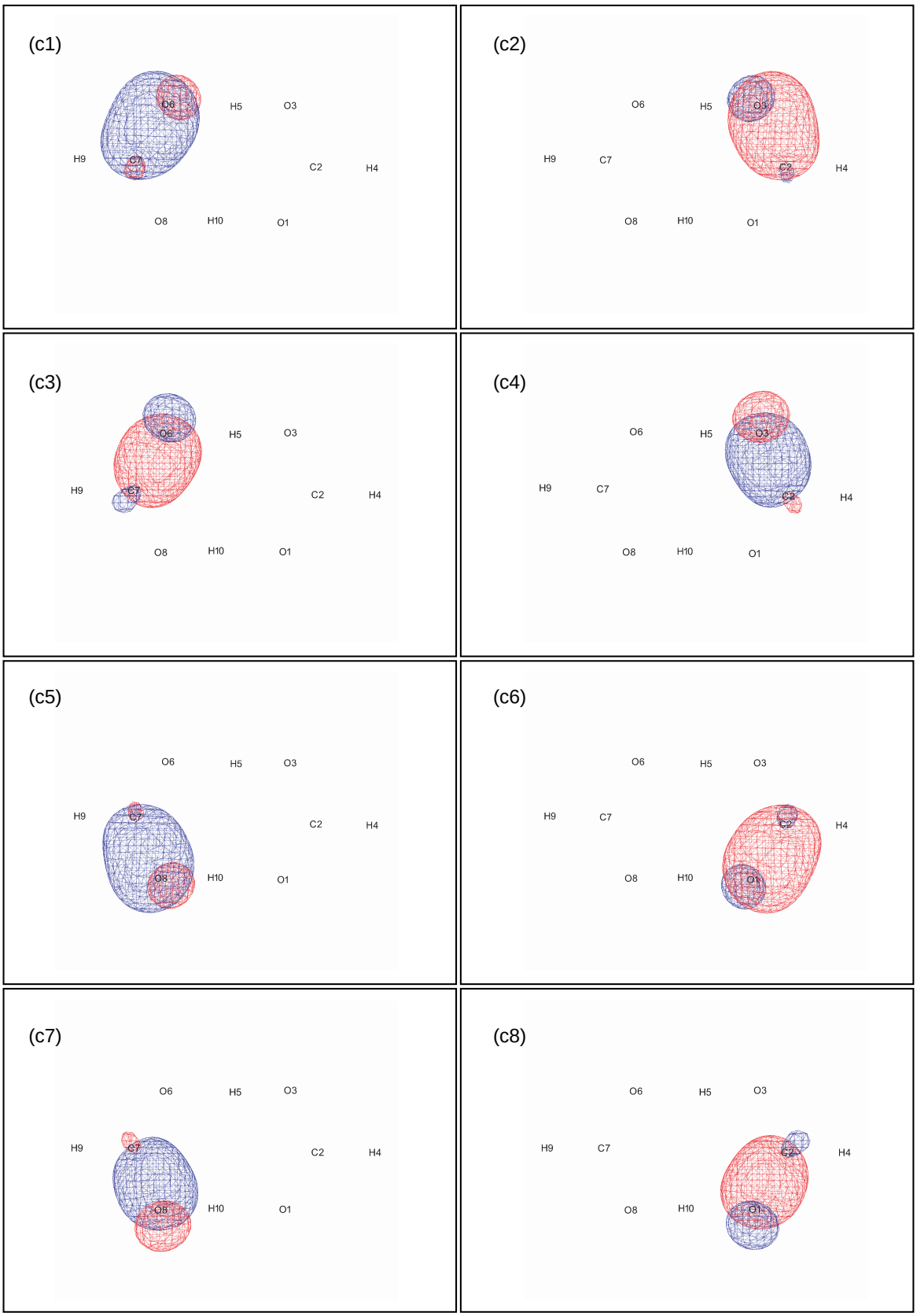

Figure 3.14: Spatial distribution of Boy's LMO for FAD in SS. Continued.

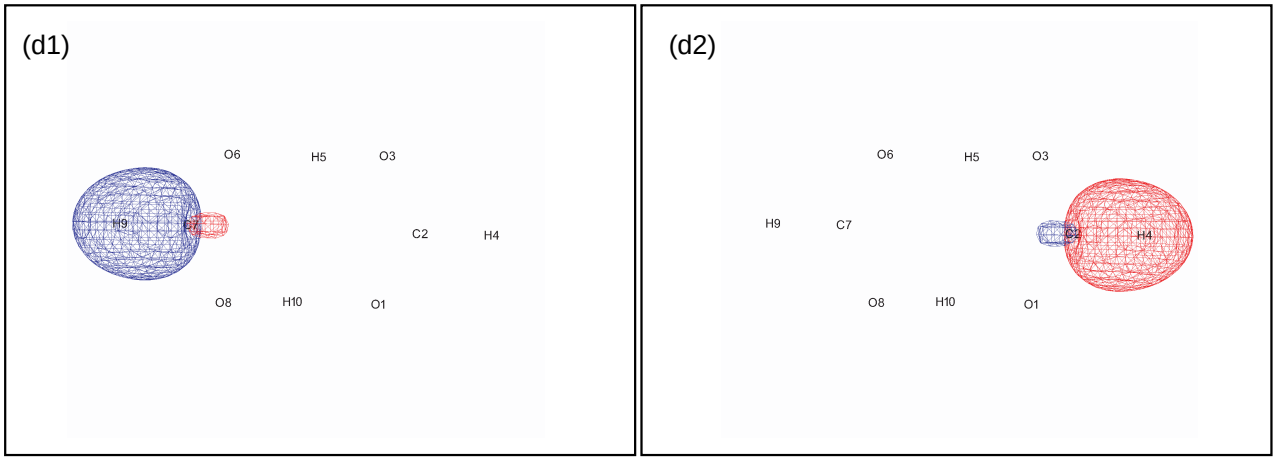

Figure 3.15: Spatial distribution of Boy's LMO for FAD in SS. Continued.

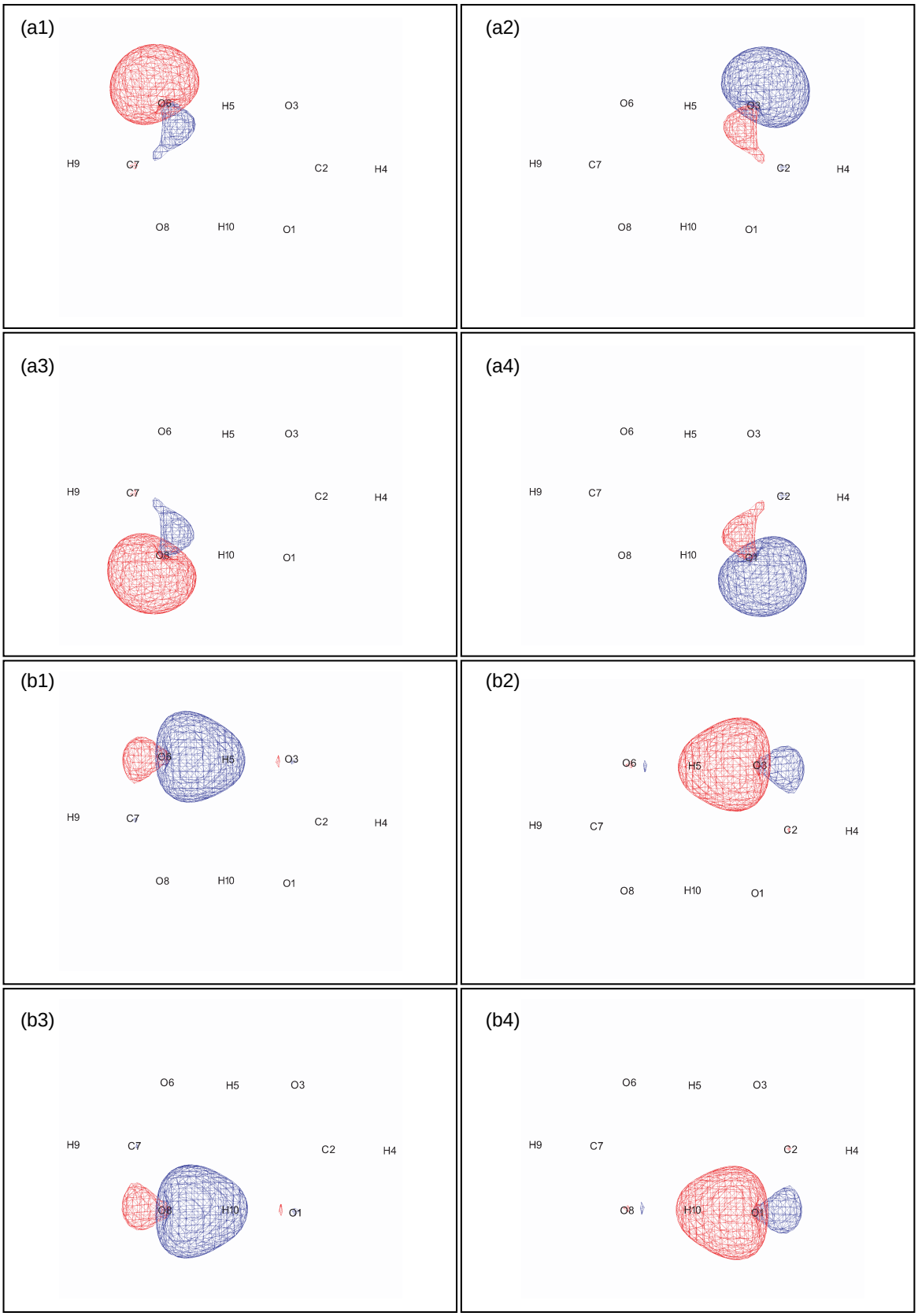

Figure 3.16: Spatial distribution of Boy's LMO for FAD in the transition state (TS). The red and blue curves represent positive and negative values, respectively. Only the occupied orbitals excep for the 1s core of C and O atoms.

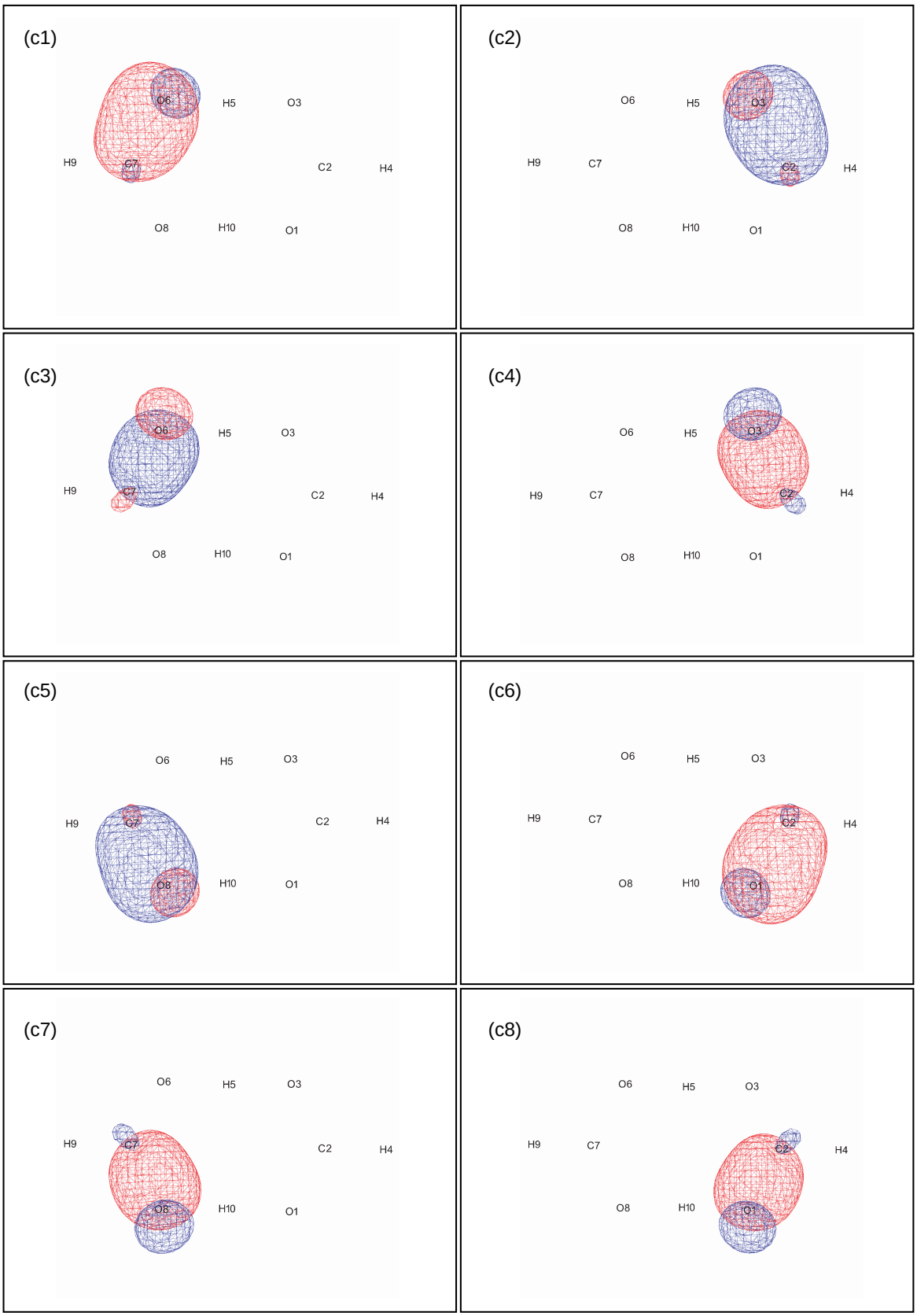

Figure 3.17: Spatial distribution of Boy's LMO for FAD in TS. Continued.

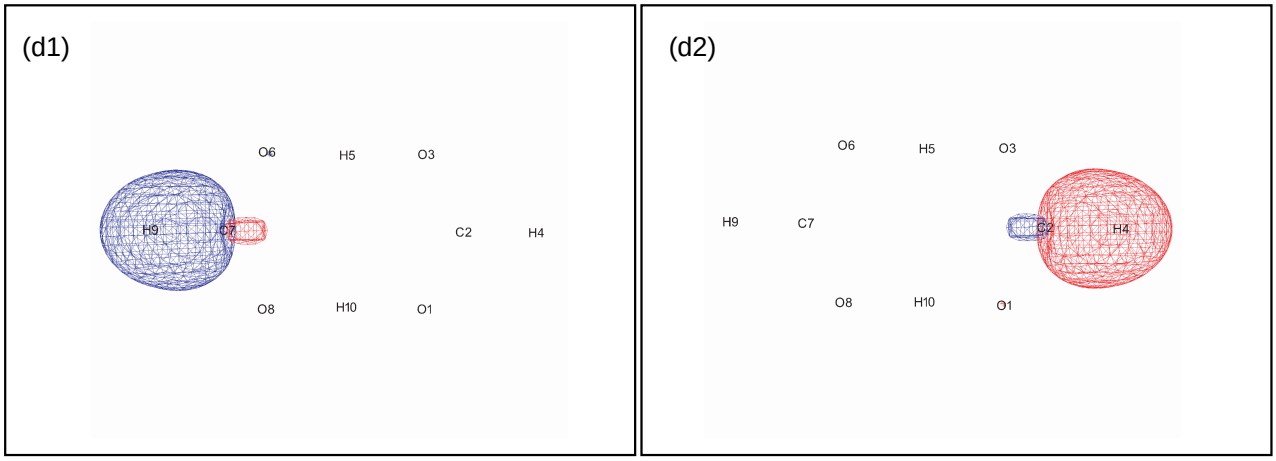

Figure 3.18: Spatial distribution of Boy's LMO for FAD in TS. Continued.

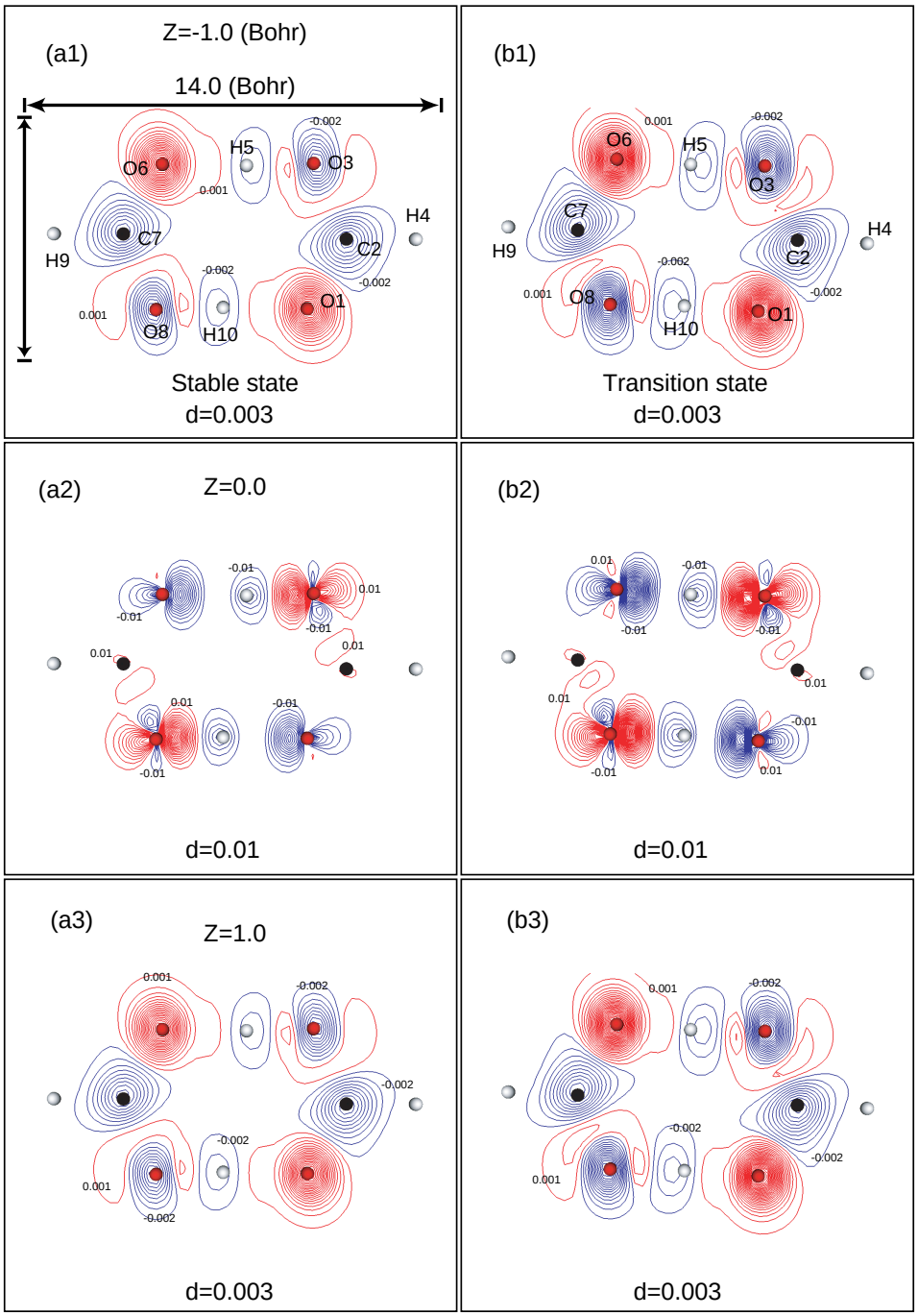

Figure 3.19: Spatial distribution of the difference density based on one electron density of FAD and FAM at the optimized geometry (a1)-(a3), and in the transition states (b1)-(b3). Panels (a1) and (b1) are the plot on $x-y$ plane at $Z=0$ (Bohr), while (a2) and (b2) are taken on $x-y$ plane at $Z=-1.0$ (Bohr). Panel (a3) and (b3) are plot on $x-y$ plane at $Z=1.0$ (Bohr), which is exactly the same as (a1) and (b1), respectively, since the molecules are on a single plane in this case. The red and blue curves represent positve and negative values, respectively, and d is the width of contour plot. The vertical line segment in panel (a1) indicates 10 (Bohr).

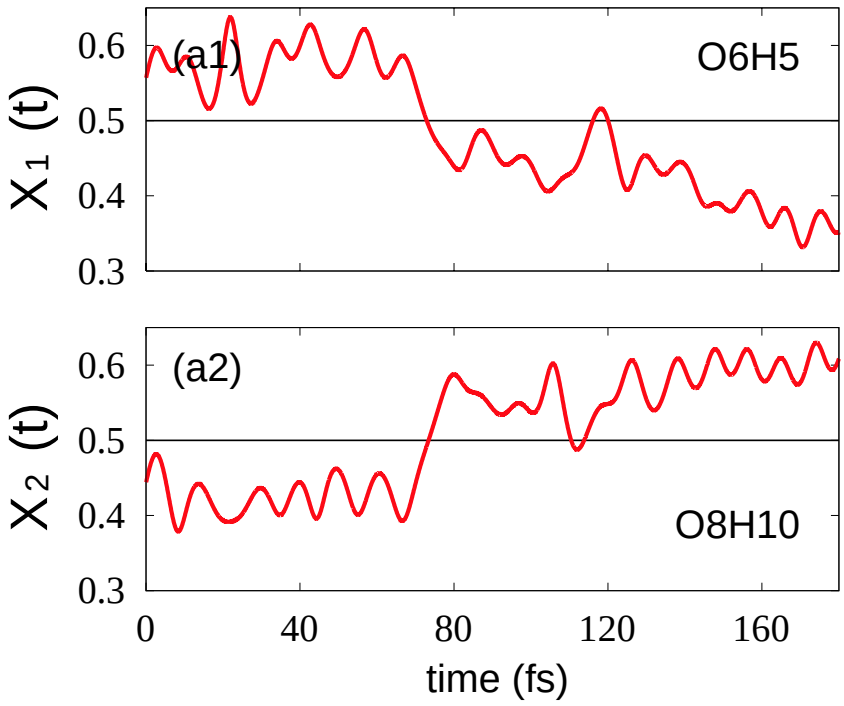

Figure 3.20: Time series of relative coordinates: Panel (a1) $X_1(t)$ and panel (a2) $X_2(t)$. See the text for the definition of the relative coordinates. $X_1 = 0.5$ (the holizontal line), for instance, means that the proton H5 is in the middle on the transferring coordinate.

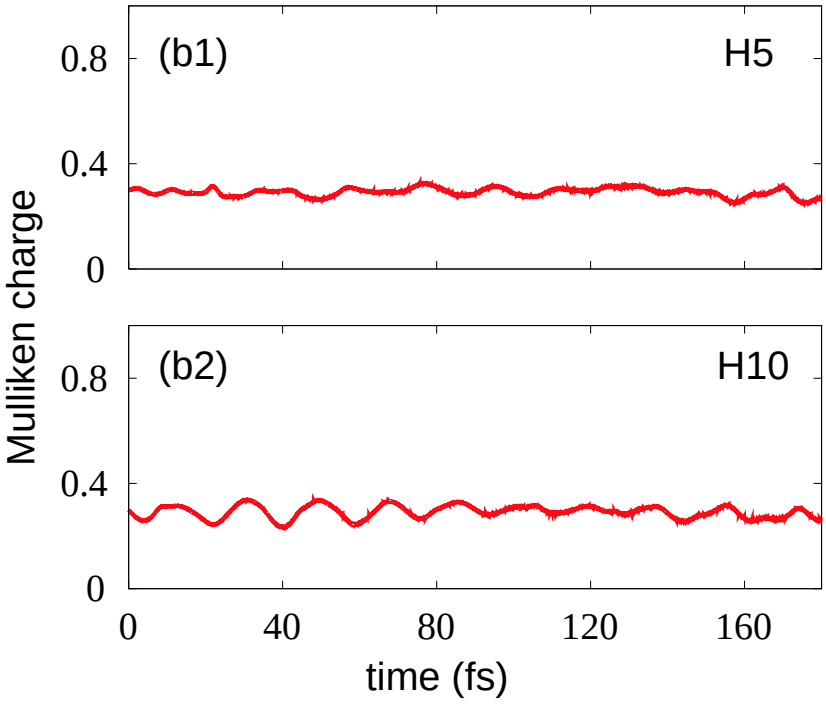

Figure 3.21: Time series of the Mulliken charge on H5 atom (panel (b1) and H10 (panel (b2)).

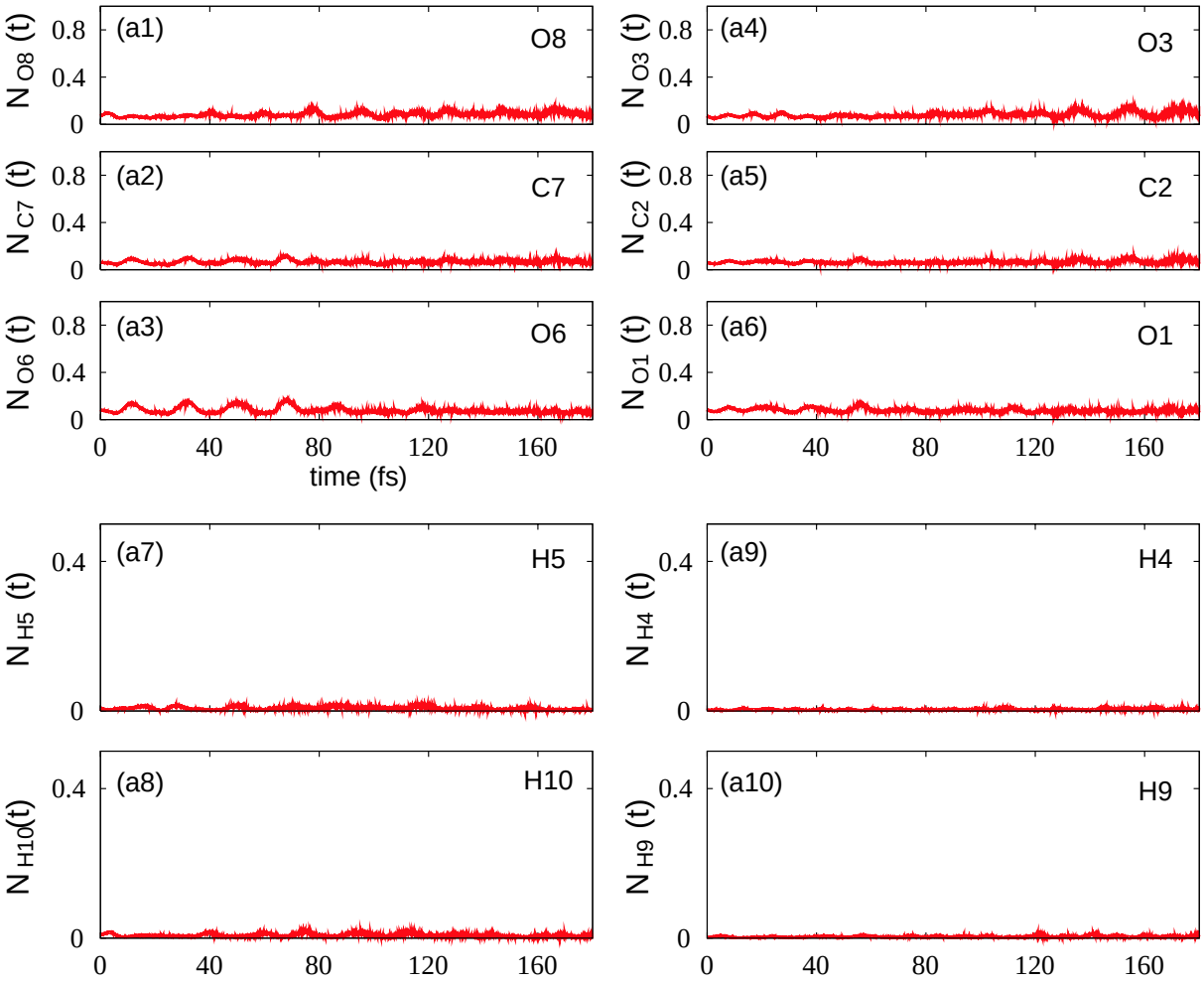

Figure 3.22: Number of the unpaired electrons on each atom: Panel (a1), (a2), (a3), (a4), (a5), (a6), (a7), (a8), (a9) and (a10) are the unpaired electron population on O1, C2, O3, H4, H5, O6, C7, O8, H9, and H10, respectively.

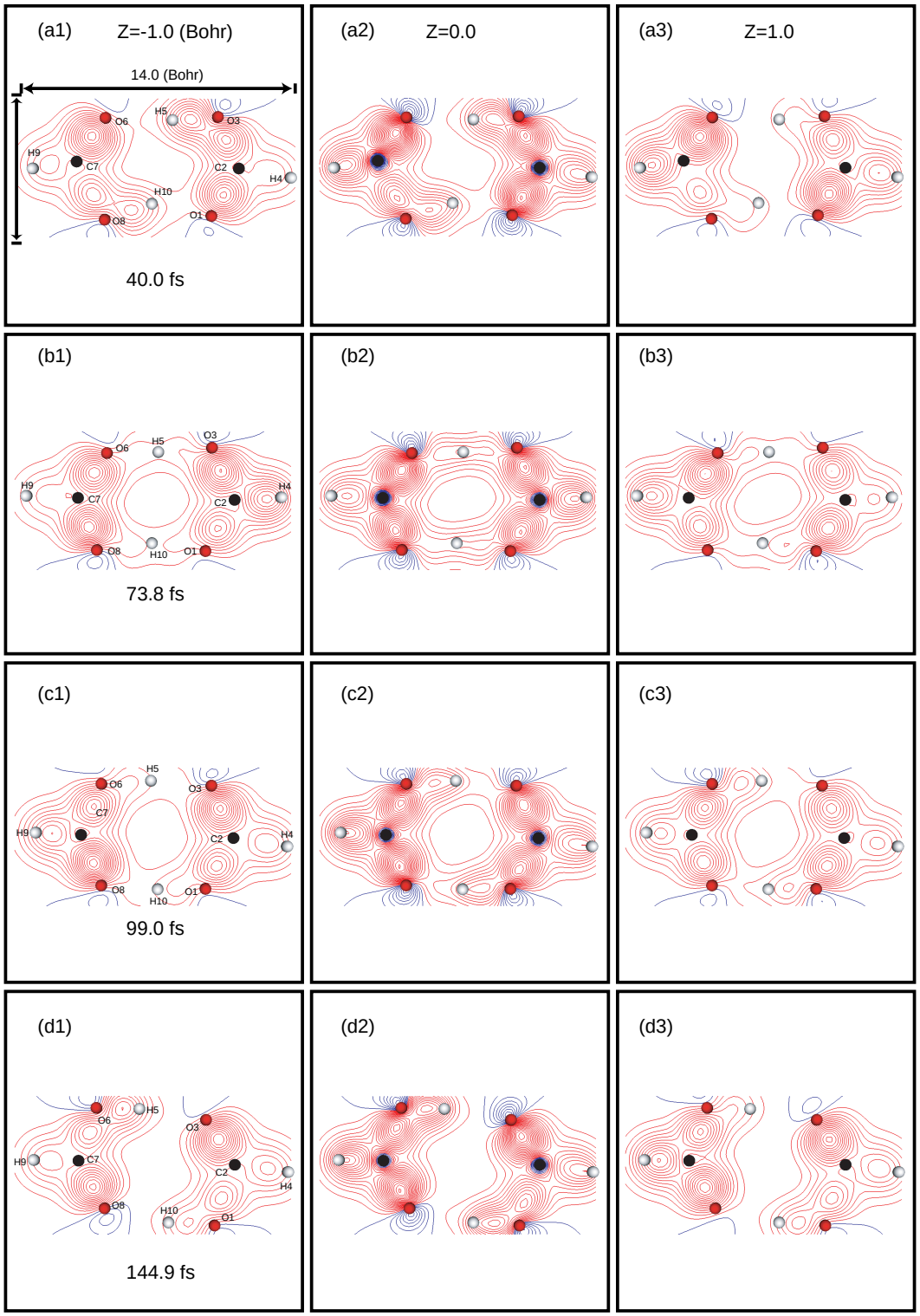

Figure 3.23: Snapshots of the bond order density on $z = -1.0$ Bohr (panels (a1), (b1), (c1) and (d1)), 0.0 Bohr (panels (a2), (b2), (c2) and (d2)) and 1.0 Bohr (panels (a3), (b3), (c3) and (d3)). The vert ical line-segment in panel (a1) indicates 6.0 Bohr. The width among both contour lines is 0.01 and 0.005 for $z = \pm 1.0$ and $z = 0.0$, respectively.

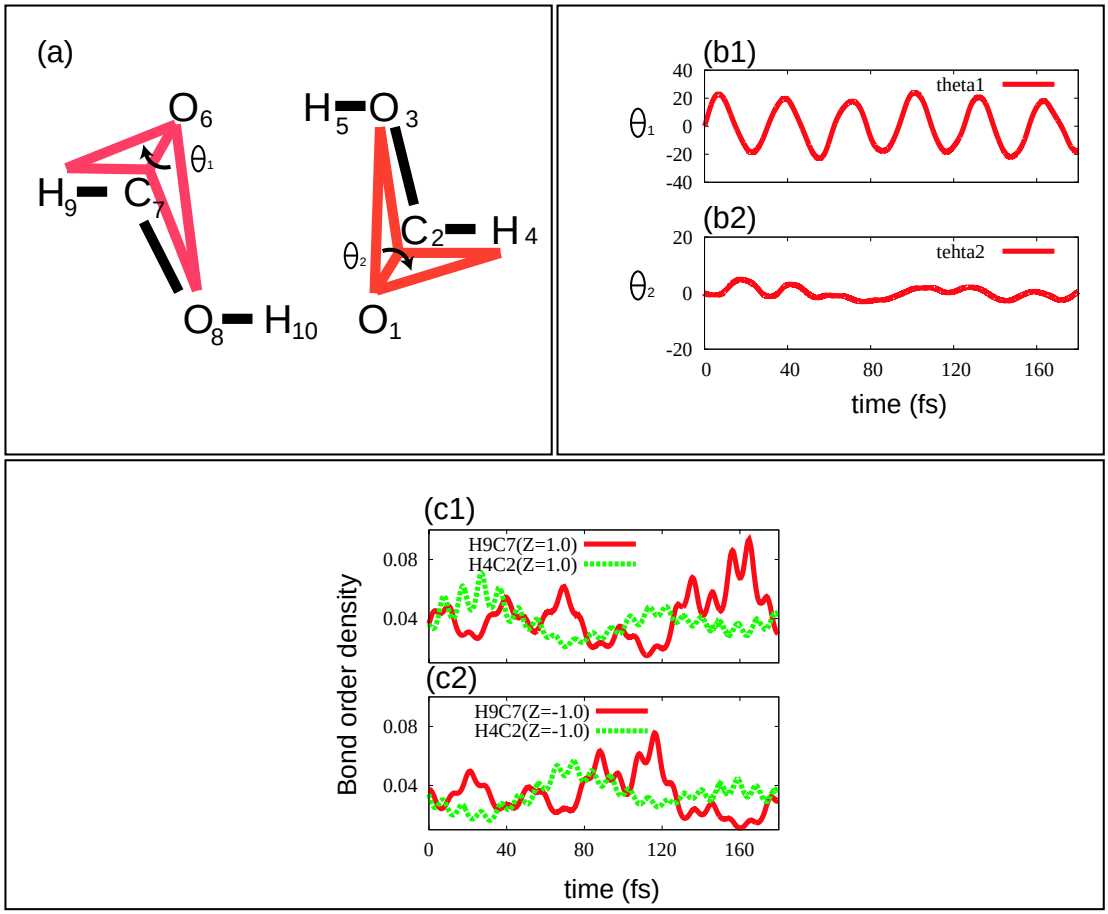

Figure 3.24: Panel (a) Definition of the dihedral angle between plane H9O1O6 and O6C7O3, and that between plane O1C2H4 and O1C2O3. Panel (b1) and (b2) are the dynamics of these dihedral angles, θ_1(b1) and θ_2(b2). Panel (c1) and (c2) exhibit the bond order density at $x = R_{\mathrm{H9}x} + |R_{\mathrm{H9}x} - R_{\mathrm{C7}x}|/2$, $y = R_{\mathrm{H9}y} + |R_{\mathrm{H9}y} - R_{\mathrm{C7}y}|/2$ and $z = \pm 1.0$.

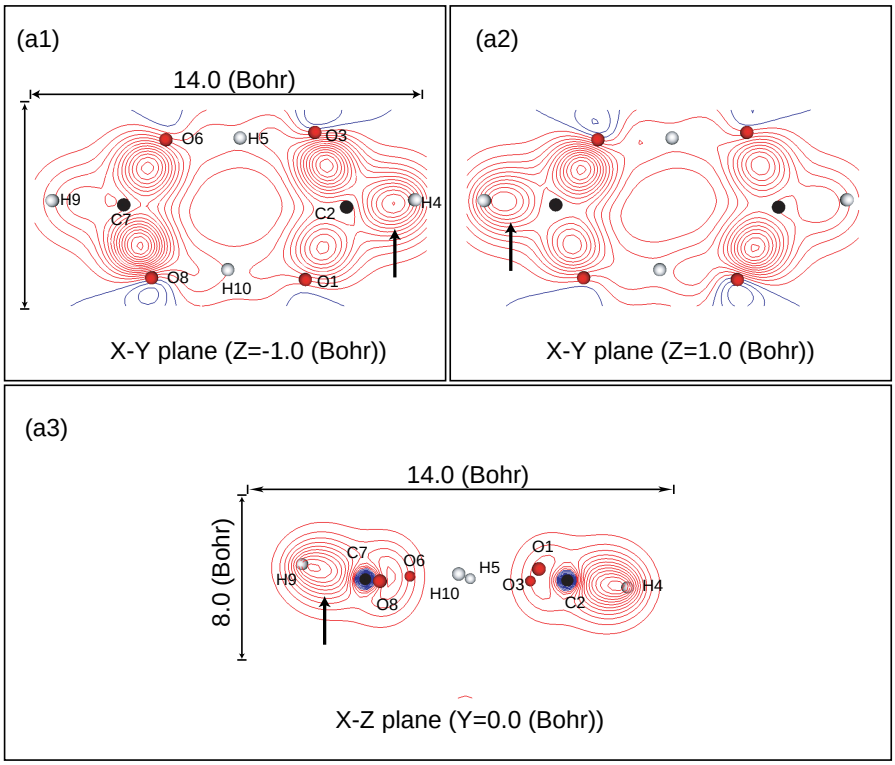

Figure 3.25: Spatial distribution of the bond order density on $x - y$ plane($z = 0$) at-time 73.11 fs. Panel(a1) and (a2) are taken at $Z = -1.0$ (Bohr) and $Z = 1.0$ (Bohr), respectively. Vertical line segment at panel (a1) is 6.0 (Bohr). Panel (a3) is the spatial distribution of bond order density taken at $x - z$ plane ($y = 0$) (side view) at 73.11 fs. Red and blue curves represent positive and negative values, respectively. The width of the contour plot at panel (a1) and (a2) is 0.005, and that of panel (a3) is 0.01.

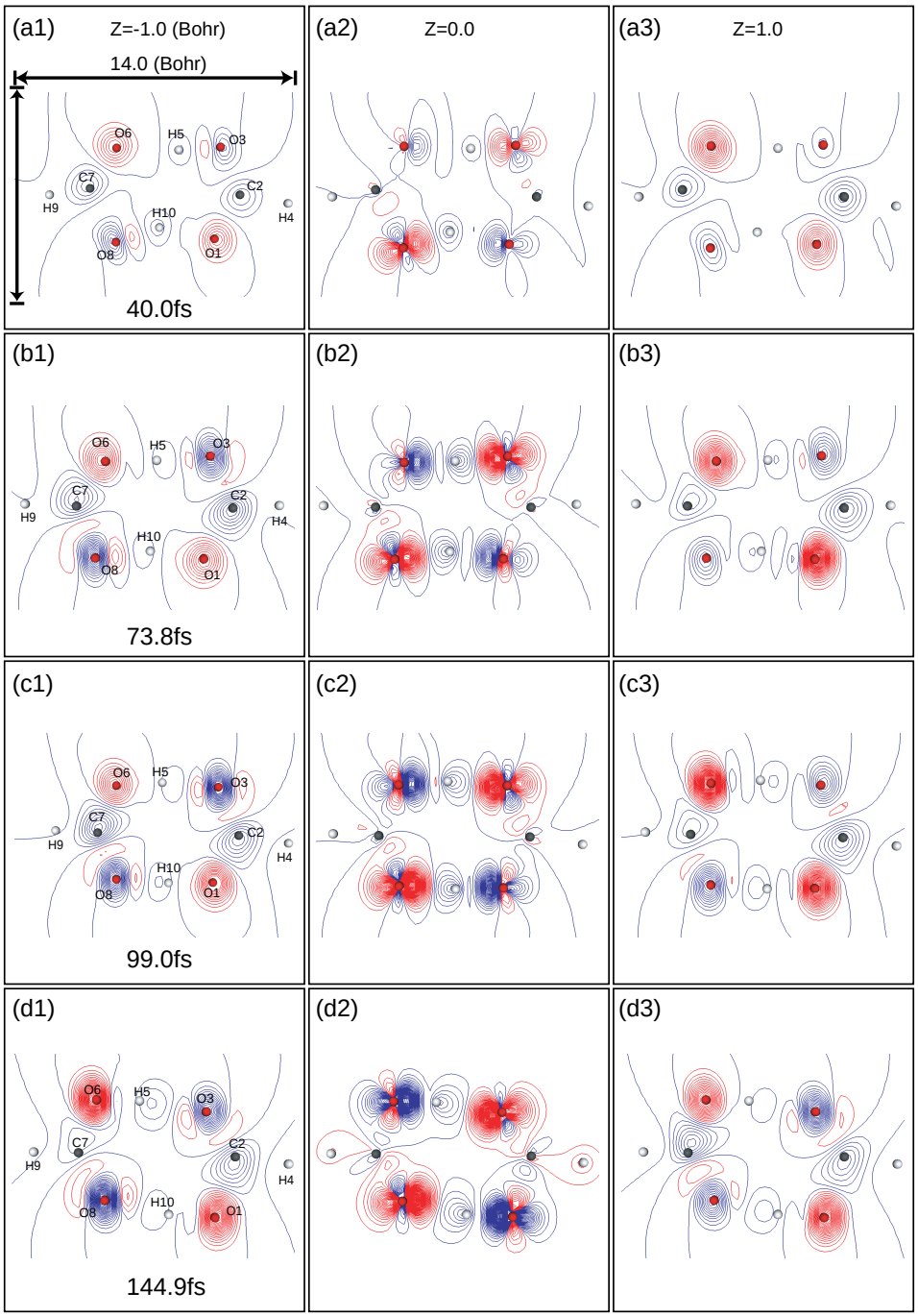

Figure 3.26: Snapshots of the difference density between formic acid dimer and formic acid monomer on $z = -1.0$(left column), 0.0 (central column), and 1.0 (right column). Time to take the snapshot is at time 69.0 fs (first row), 73.1 fs (second row), 76.0 fs (third row), and 81.0 fs (fourth row). The width among both contour lines is 0.01 and 0.005 for $z = \pm 1.0$ and $z = 0.0$, respectively.

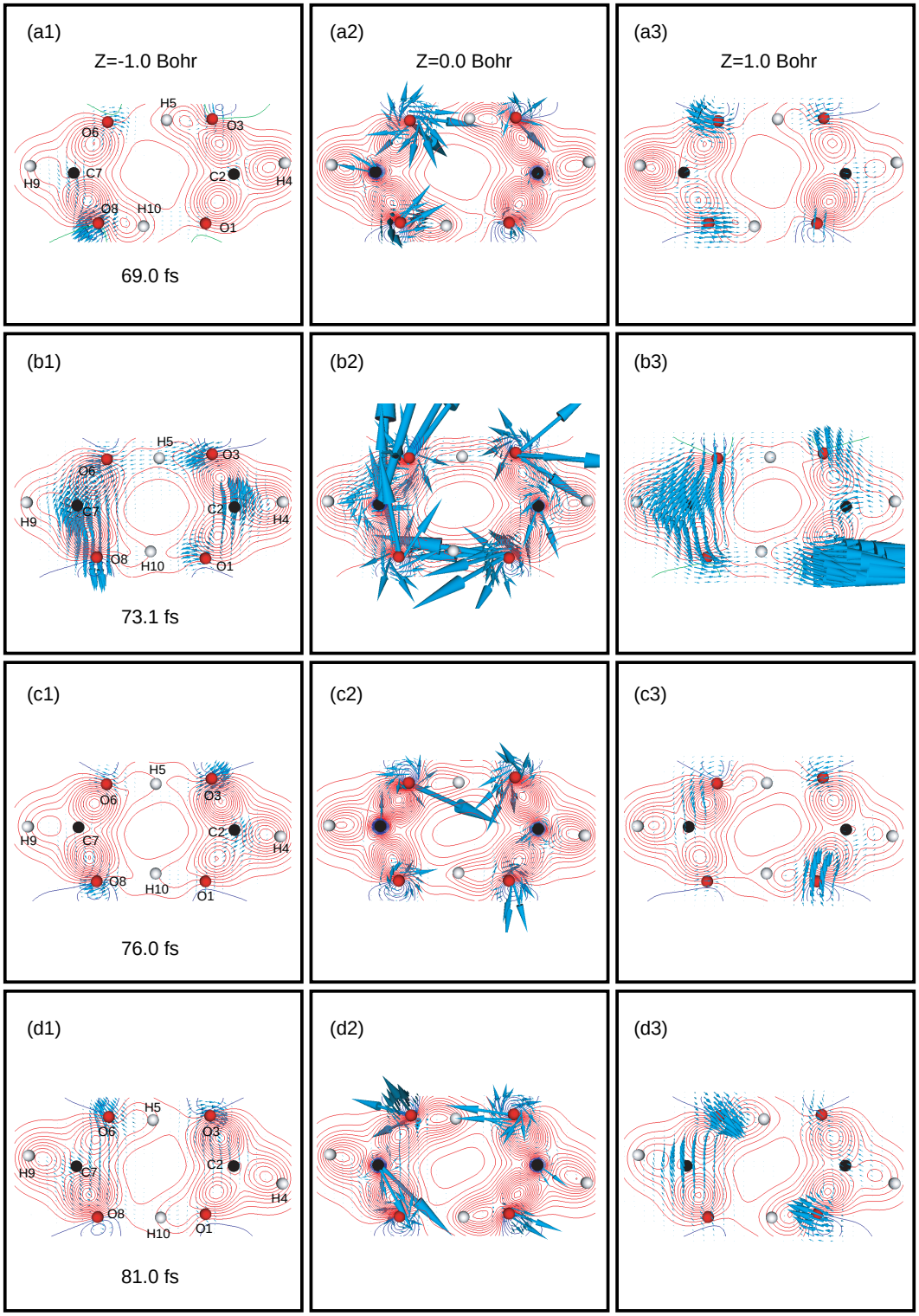

Figure 3.27: Snapshots of the adiabatic flux on on $z = -1.0$ (left column), 0.0 (central column), and 1.0 (right column). Time to take the snapshot is at time 69.0 fs (first row), 73.1 fs (second row), 76.0 fs (third row), and 81.0 fs (fourth row). The arrow and the contour in these panels are the vector and scalar fields of adiabatic flux, respecitvely. The width among both contour lines is 0.01 and 0.005 for $z = \pm 1.0$ and $z = 0.0$, respectively.

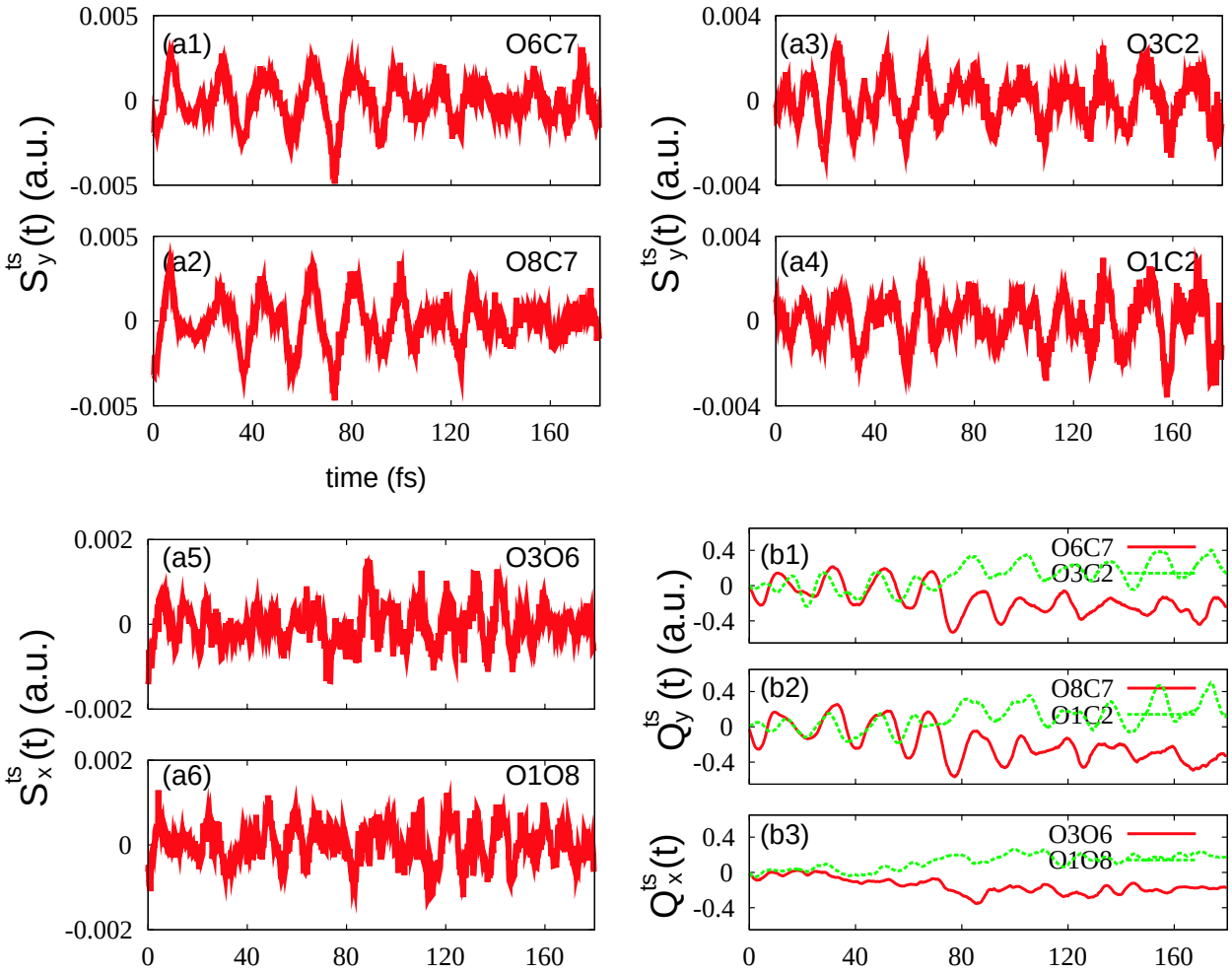

Figure 3.28: Surface integral of the adiabatic flux. Panel (a1), (a2), (a3) and (a4) are $S_y^{(\mathrm{ad})}(y_0, t)$ on O8C7, O6C7, O1C2, and O3C2, respectively. Panel (a5) and (a6) are $S_x^{(\mathrm{ad})}(x_0, t)$ on O3O6 and O1O8, respectively. Panel (b1), (b2) and (b3) are the time integral of Eq.(3.3.14), where red and green curves represent $Q_y^{(\mathrm{ad})}(y_0, t)$ of O6C7 and O3C2, and of O8C7 and O1C2, respectively. Panel (b3) show $Q_x^{(\mathrm{ad})}(x_0, t)$ of O3O6 and O1O8, respectively.

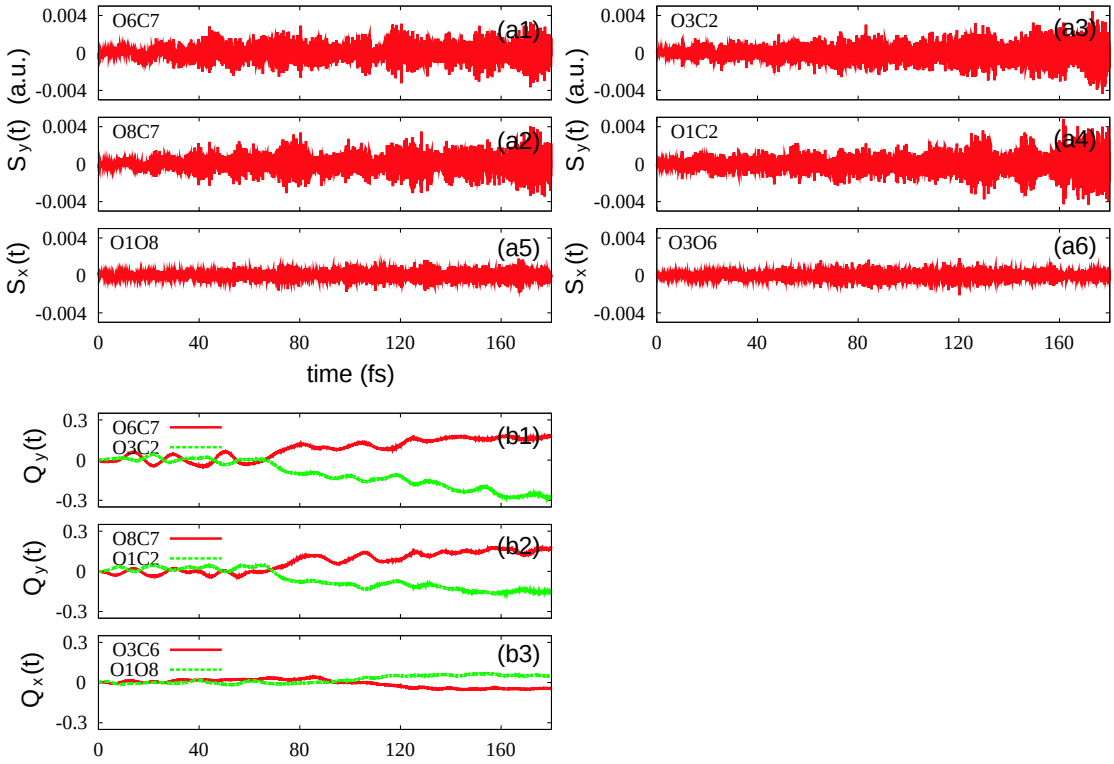

Figure 3.29: Surface integral of Schiff's probability current. Panels (a1), (a2), (a3), (a4), (a5) and (a6) are those taken on O8C7, O6C7, O1C2, O3C2, O3O6 and O1O8, respectively. Panel (b1), (b2) and (b3) are the time integral of Eq.(3.3.14), where red and green curves represent $Q_y^{(\mathrm{ad})}(y_0, t)$ of O6C7 and O3C2, and of O8C7 and O1C2, respectively. Panel (b3) show $Q_x^{(\mathrm{ad})}(x_0, t)$ of O3O6 and O1O8, respectively.

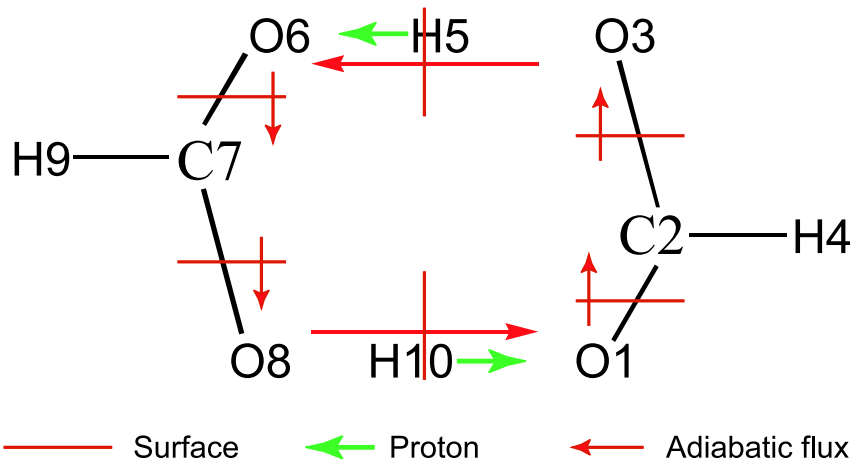

Figure 3.30: Direction of the gross electron flow assocaited with the double proton transfer as estimated with the adiabatic flux.

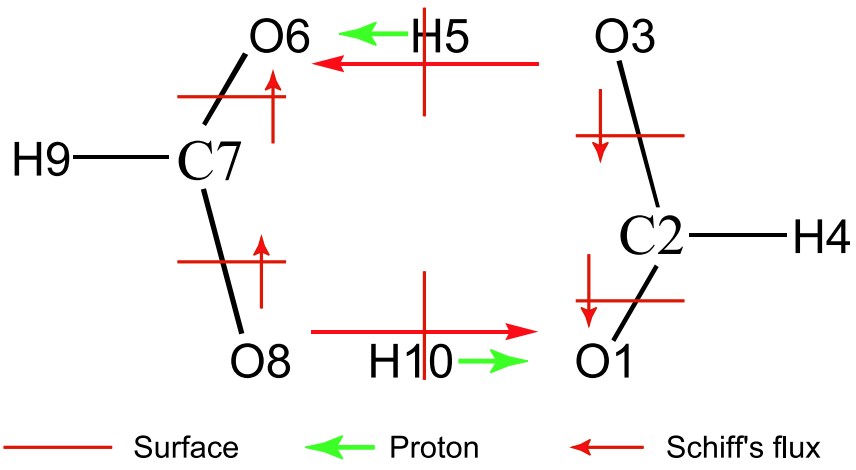

Figure 3.31: Direction of the gross electron flow assocaited with the double proton transfer as estimated with the Schiff's flux.

Chapter 4

General Conclusions

In this thesis, we have constructed a method to analyze electron dynamics causing a chemical reaction within a mixed quantum-classical treatment and the method was applied to double proton transfer for formic acid dimer.

In chapter 1, we first studied an effective way to track a change of electron wavepacket within molecule in terms of probability current density, which is the current of electronic density at time t. However, Schiff's flux gives only a null field for *ab initio* molecular dynamics (AIMD) method, which is one of the frequently used quantum chemical method. In order to resolve the difficulty, we defined adiabatic flux, which is the imaginary part of the time shift flux that we have invented. This flux represents the current density arising from the time shift overlap distribution of electronic wavefunctions at different times. We have shown how it works taking examples from colliding dynamics for H_2 and NaCl with use of the semiclassical Ehrenfest and the AIMD methods. It was shown that the adiabatic flux describes the generating process of covalent bonding for H_2. In NaCl the adiabatic flux well described the generating process of formation of the ionic bond of NaCl. Thus, the adiabatic flux is shown to be capable of describing basic chemical processes.

In chapter 2, we studied double proton transfer for formic acid dimer (FAD) by using the adiabatic and Schiff's fluxes and some physical quantities, which turn out to be useful for chemical analysis. We studied double proton transfer in formic acid dimer as a general example. This dynamics consists of two major processes: The first one is dimerization of two isolated formic acid monomers (FAMs) to FAD, and the second process is the transfer motions of two protons. In the first process, we showed how the electronic probability density moves among O-H-O on the way generating from two FAMs to FAD by using configuration interaction singles and doubles (CISD) method. In this process, by calculating difference density between the FAD and the two FAMs, we showed that π electrons delocalize over the O-C-O sites. Moreover, it was found that oxygen atoms not bonding with hydrogen one undergoes a hybridization from sp^2 to sp^3 hybrid orbitals and oxygen atoms bonding with hydrogen atom causes a hybridization from sp^3 to sp^2 hybrid

orbitals. Thus, in the dimerization process alone, we expect that electronic probability density flows clockwise among two oxygen and hydrogen atoms in a collective manner. Such an electronic rearrangement in dimerization prepares the system into the stage of easy proton transfer. In the second process, therefore, two protons in the FAD move to each other from the old CH bonding sites to new CH bonding sites without much difficulty and without further large electronic rearrangement. Indeed, we have observed a slight current of electrons now in the direction of the proton movement.

List of Publications

[1] Michihiro Okuyama and Kazuo Takatsuka, Chemical Physics Letters **476**, 109 (2009).
Electron flux in molecules induced by nuclear motion

Acknowledgements

The present thesis is the summary of my studies from 2005 to 2009 at the Graduate School of Arts and Sciences, The University of Tokyo, under the guidance of Professor Kazuo Takatsuka.

I cordially thank Professor Kazuo Takatsuka for his powerful guidance, invaluable suggestions and stimulating discussions. I could only accomplish the study through his continuous encouragement since I often happened to be in the situation where I could not obtain results. Furthermore, I could learn many useful things in my life under his guidance. Therefore, I would like to thank him from my heart. I'm thankful to Dr. Hiroshi Ushiyama and Dr. Satoshi Takahashi for their kind support in my laboratory's life. I'm also thankful to Dr. Yasuki Arasaki for various interesting comments: programing language, electronic state calculation package, English writing and some remarkable comments. I express sincere thanks to Dr. Yasuteru Shigeta, Dr. Tomokazu Yasuike, Dr. Kiyoshi Yagi, Dr. Márcio. T. do N. Varella, Dr. Takehiro Yonehara, Dr. Hiroshi Teramoto and Dr. Mikiya Fujii for the discussion of some essential problems about electronic structure calculation and my study. Acknowledgements is made to the members of Takatsuka Laboratory: Dr. Takefumi Yamashita, Dr. Norifumi Yamamoto, Dr. Agung Budiyono, Dr. Hiroshi Fujisaki, Dr. Tomohiro Yanao, Dr. Koji Hotta, Kentaro Yamasaki, Dr. Kenta Odagiri, Dr. Koh Yang Wei Patrick, Dr. Scheit Simona, Dr. Manabu Kanno, Li Zhong-Wei, Atsuhiro Umayahara, Kohei Umetsu, Junko Nakajima, Hajime Ohtsuki, Munehisa Kiriyama, Kengo Nagashima, Nobuki Inoue, Kota Hanasaki, Shin-ichi Koda, Kentaro Yamamoto, Kosuke Miki, Yukiko Kosaka and Chigako Yoshida for their valuable discussions and helpflul comments and is also made to the members to my colleagues in Ibaraki University: Dr. Lu Guo, Takuji Ishikawa, Dr. Yasuaki Ito, Seiichi Yoshida, Masahiko Katsu, Yohei Hashi, Nobuyuki Matsueda and Naoki Minagawa for valuable discussions and very interesting comments. I'm thankful to Professor Jörn Manz, Professor Fumihiko Sakata, Professor Masanori Tachikawa and Associate Professor Seiji Mori for discussion and valuable comments on electron flux and many body theory in molecular systems. I thanks Professor Hiroyasu Kawabe for some valuable comments. Finally, I wish to express my gratitude to my family and my friends for their support.

Tokyo, Japan, December 2009
Michihiro Okuyama